Computational Studies of Turbulent Skin-Friction Drag Reduction with Super-Hydrophobic Surfaces and Riblets

by

Sayed Amirreza Rastegari

A dissertation submitted in partial fulfillment
of the requirements for the degree of
Doctor of Philosophy
(Mechanical Engineering and Scientific Computing)
in The University of Michigan
2017

Doctoral Committee:

Associate Professor Rayhaneh Akhavan, Chair
Professor John P. Boyd
Professor Charles R. Doering
Professor Katsuo Kurabayashi

Sayed Amirreza Rastegari

amirreza@umich.edu

ORCID iD: 0000-0002-2637-2465

To My Parents

ACKNOWLEDGEMENTS

Foremost, I would like to express my sincere gratitude and appreciation to my thesis advisor Prof. Rayhaneh Akhavan for the patient guidance, mentorship and support she provided to me over the years.

I would also like to thank my thesis committee members, Prof. John P. Boyd, Prof. Charles R. Doering, and Prof. Katsuo Kurabayashi, for all that I learned from them in their classes, and their guidance, encouragement and insightful suggestions.

In a similar vein, I would like to thank my friends Dr. Dong-Hyun Lee, Dr. Yifeng Tang, Dr. Ali Ramazani, Dr. Pooya Movahed, Aslan Satari Dizaji, Roman Gayduk, Vahid Rahsidi and Babak Khamsehi for the stimulating discussions we have had in the past years, and for the contributions that each of them made to my intellectual and personal growth during my years of study at the University of Michigan.

Last but not the least, I would like to thank my parents for supporting me throughout my life.

TABLE OF CONTENTS

LIST OF FIGURES

Figure

LIST OF TABLES

Table

LIST OF ABBREVIATIONS

SH Super-Hydrophobic

DR Drag Reduction

BWU Base-flow Wall Unit

DNS Direct Numerical Simulation

LB Lattice Boltzmann

LBM Lattice Boltzmann Method

LGCA Lattice Gas Cellular Automata

DF Distribution Function

EDF Equilibrium Distribution Function

LDA Laser-Doppler Anemometry

CLI Central Linear Interpolation

CFL Courant Friedrichs Lewy

MG Micro-Groove

LMG Longitudinal Micro-Groove

DI Drag Increase

TKE Turbulence Kinetic Energy

rms root-mean-square

FFT Fast Fourier Transform

PR Power Reduction

SFF Shear Free Fraction

μ – **PIV** Micro-Particle Imaging Velocimetry

ABSTRACT

Computational Studies of Turbulent Skin-Friction Drag Reduction with Super-Hydrophobic Surfaces and Riblets

by

Amirreza Rastegari

Chair: Rayhaneh Akhavan

Skin-friction Drag Reduction (DR) with Super-Hydrophobic (SH) surfaces and riblets was investigated using Direct Numerical Simulation (DNS) to study the scaling and mechanism of DR, and the pressure loads on SH surfaces in turbulent flow environments. The computations were performed using Lattice Boltzmann (LB) methods in turbulent channel flow at a bulk Reynolds number of 3600. SH surfaces composed of Longitudinal Micro-Grooves (LMGs) of size 4 to 128 Base-flow Wall Units (BWUs) with Shear Free Fractions (SFFs) of 1/2, 7/8 and 15/16, transverse Micro-Grooves (MGs) of size 8 to 56 BWUs with SFFs of 1/2 and 7/8, and micro-posts of size 8 to 56 BWUs with SFFs of 1/4 and 49/64 were studied by DNS. The liquid/gas interfaces on the SH walls were modeled as 'idealized' flat, shear-free boundaries in these simulations. Additionally, a second set of DNS studies, with SH LMGs and scallop-shaped riblets of size 14 to 56 BWUs with a MG width to MG pitch ratio of 7/8, were performed to investigate the effect of interface deformation on SH LMGs, and compare the results to riblets. The liquid/gas interfaces on the SH LMGs in these simulations were modeled as stationary curved, shear-free regions,

with the meniscus shape obtained from the solution of the Young-Laplace equation. Interface protrusion angles of 0, -30, -60 and -90 degrees were investigated. The same geometries as those formed by the curved SH LMG interfaces were also studied as riblets. DRs of up to 83% and 10% were realized in DNS with the SH surfaces and riblets, respectively.

By analysis of the governing equations, it is shown that in laminar or turbulent channel flow with any SH or riblet wall micro-pattern five elements contribute to DR: (i) the effective slip at the wall, (ii) changes in the normalized structure of turbulence due to the drop in the friction Reynolds number of the flow because of this wall slip, (iii) other changes in the normalized structure of turbulence, (iv) changes in the structure of mean flow, and (v) the minor flow rate through the wall micro-texture. Comparison of DNS results to this expression shows that over 90% of the DR with SH LMGs and all of the DR with riblets arises from effects (i, ii, v). Modifications to the normalized structure of turbulence (iii) were found to be always drag increasing with riblets and SH LMGs of size less than 20 wall units, and only mildly drag reducing with SH LMGs of size greater than 20 wall units. For riblets, this effect leads to diminishing DRs with riblets of size greater than 14 wall units. The presence of interface deformation in SH LMGs led to increases of 2% to 5% in the magnitude of DR at low protrusion angles (-30 degrees), and drops of -0.5% to -10% at high protrusion angles (-90 degrees), compared to flat interfaces. Furthermore, interface deformation led to significant drops in the magnitude of pressure fluctuations with SH LMGs of size ~ 14 BWUs at small protrusion angles (-30 degrees), compared to flat interfaces, offering new opportunities for improving the stability of SH LMGs in turbulent flows. With riblets, the highest DRs were always obtained at the largest MG depths, with the peak DR obtained with MGs of size ~ 14 BWUs.

CHAPTER I

Introduction

Control of wall turbulence, for the purpose of skin friction DR, has been a long-standing goal of turbulence research (*Bushnell and McGinley*, 1989; *Bushnell and Hefner*, 1990). Numerous turbulence control strategies have been proposed over the years (*Bushnell and Hefner*, 1990; *Lumley*, 1969; *Bechert et al.*, 1997; *Lumley and Blossey*, 1998; *Karniadakis and Choi*, 2003). Broadly, these can be classified into active or passive control strategies. In active control strategies, the dynamics of turbulence is manipulated through addition or removal of mass, momentum or energy to/from the boundary layer, to reduce the skin-friction drag (*Bushnell and Hefner*, 1990; *Coustols and Savill*, 1992a,b). Active control strategies can be either open-loop, in which the control strategy is set a priori without monitoring the status of turbulence, or closed-loop, in which the control mechanism is applied in real-time based on signals received from arrays of sensors and activation through actuators. Passive turbulence control strategies are implemented through changing the geometrical or physical characteristics of the bounding walls of the flow (*Bushnell and Hefner*, 1990; *Coustols and Savill*, 1992a,b). Unlike active turbulence control strategies, passive strategies require no external source of energy, making them more likely to achieve net energy savings. Furthermore, no extra arrays of sensors and actuators are used with passive strategies, making their implementation and maintenance costs lower.

Of the passive turbulence control strategies devised to date, micro-textured surfaces provide one of the oldest and most promising methods of skin-friction DR in turbulent wall-bounded flows. Two classes of micro-textured surfaces have been extensively studied in the literature: riblets and SH surfaces.

1.1 Riblets

The earliest designs of micro-textured surfaces were inspired by shark skins, on which the dermal denticles display rib-like protrusions (*Chernyshov and Zayets*, 1970). In man-made implementations, the wall boundaries were carpeted with arrays of LMGs, known as riblets. Numerous experimental (*Bushnell and Hefner*, 1990; *Bechert et al.*, 1997) and computational (*Choi et al.*, 1993; *Goldstein and Tuan*, 1998; *Karniadakis and Choi*, 2003; *García-Mayoral and Jiménez*, 2011) studies in turbulent channel flows or boundary layer flows have shown DRs of up to 10% with riblets. The DR performance has been shown to depend on the MG width in 'wall units', and the cross-sectional shape of the riblets (*Bushnell and Hefner*, 1990; *Choi et al.*, 1993; *Bechert et al.*, 1997; *Goldstein and Tuan*, 1998; *Karniadakis and Choi*, 2003; *García-Mayoral and Jiménez*, 2011). Highest DRs were obtained with V-grooved or scallop shaped riblets of width $g^+ \approx 15$ (*Bushnell and Hefner*, 1990; *Bechert et al.*, 1997), where g denotes the MG width, and the $+$ superscript denotes non-dimensionalization in 'wall units', using the wall-friction velocity, u_τ, and kinematic viscosity, ν, of the flow. Beyond groove widths of $g^+ \gtrsim 15$, the DR performance degrades, eventually leading to a drag increase for groove widths greater than 30 wall units (*Bushnell and Hefner*, 1990; *Choi et al.*, 1993; *Bechert et al.*, 1997; *Goldstein and Tuan*, 1998; *Karniadakis and Choi*, 2003; *García-Mayoral and Jiménez*, 2011). The DR regime observed in riblets of width up to 15 wall units is generally referred to as the 'viscous regime', while that in riblets of width greater than 15 wall units is generally referred to as the 'breakdown regime' (*Bechert and Bartenwerfer*, 1989; *García-Mayoral and*

Jiménez, 2011). DR in the 'viscous regime' has been attributed to the hindering of the spanwise turbulence fluctuations in the near wall regions by riblets (*Choi et al.*, 1993; *Bechert et al.*, 1997; *Karniadakis and Choi*, 2003; *García-Mayoral and Jiménez*, 2011). *Choi et al.* (1993) suggest that riblets reduce momentum transport by impeding the cross-flow motion through reducing the strength of streamwise vortices above the riblets. This, in turn, weakens the downwash and ejection motions and reduces the Reynolds shear stress over the riblets. *Bechert et al.* (1997) suggest that riblets impede the fluctuating turbulent crossflow near the wall, thus reducing momentum transfer and Reynolds shear stresses. *Karniadakis and Choi* (2003) suggest that riblets impede the spanwise movement of longitudinal vortices, thus hampering the stretching of longitudinal vortices which reduces the strength of the downwash motions during the sweep events. The contribution of turbulence to the wall shear stress arises from the downwash of high-momentum fluid by the streamwise vortices (*Choi*, 1989). As such, the reduction in the strength of the downwash motions leads to a reduced wall-friction (*Karniadakis and Choi*, 2003). *García-Mayoral and Jiménez* (2011) suggest that impeding the spanwise flow induced by the overlying streamwise vortices results in moving the streamwise vortices away from the wall, and leads to a reduction in the turbulent mixing of the streamwise momentum. A number of theories also have been proposed to explain the degradation of the DR performance in the 'breakdown regime'. Based on quadrant analysis of turbulent flow *Choi et al.* (1993) proposed that the streamwise vortices lodge inside the riblets. As a result, a larger surface area is exposed to the sweep motions induced by the streamwise vortices, thus decreasing the DR performance. *García-Mayoral and Jiménez* (2011) proposed that the breakdown regime is caused by the appearance of long spanwise rollers in the flow, which results in additional Reynolds stresses.

Research on passive turbulence control by riblets has been mainly focused on turbulent flows. The DR or Drag Increase (DI) effect of riblets in turbulent flow, in

all the studies, has been attributed to the modification of vortical structures due to the presence of riblets on the walls (*Bushnell and Hefner*, 1990; *Choi et al.*, 1993; *Bechert et al.*, 1997; *Goldstein and Tuan*, 1998; *Karniadakis and Choi*, 2003; *García-Mayoral and Jiménez*, 2011). Effect of riblets in laminar flows, however, has been controversial, with some studies reporting DR (*Mohammadi and Floryan*, 2013, 2015) while others report DI (*Choi et al.*, 1991; *Chu and Karniadakis*, 1993). It has been proposed that use of riblets in laminar flow leads to increased surface areas exposed to the viscous friction, and thus increased frictional drag forces (*Choi et al.*, 1991; *Chu and Karniadakis*, 1993). However, recent studies suggest that proper configurations of riblets can sufficiently reduce the shear in the bulk flow to compensate for the DI associated with the increase in the wetted area, thus resulting in a net reduction in the friction drag (*Mohammadi and Floryan*, 2013, 2015).

1.2 Super-Hydrophobic Surfaces

Another class of micro-textured surfaces, which has gained much attention during the recent years, are SH surfaces. These were inspired by the water-repellent structure of lotus leaves, on which a water-repellent 'hydrophobic' wax covers the rough exterior of the leaves and allows rain drops to slide on the leaves (*Ma and Hill*, 2006; *Rothstein*, 2010). Mimicking the structure of natural surfaces, this class of micro-textured surfaces is made of a combination of surface micro-textures and liquid-repelling coatings. Standard micro-manufacturing techniques, such as photolitography, are used to create the surface micro-textures. These micro-textures are then covered by liquid-repelling coatings. The resulting SH surfaces are characterized by a large apparent receding contact angle, typically greater than 150^o (*Schellenberger et al.*, 2016). When such surfaces come into contact with low surface energy liquids, such as water, gas pockets form inside the surface indentations (*Tyrrell and Attard*, 2001; *Tretheway and Meinhart*, 2004). The liquid/gas menisci formed on top of these entrapped gas pockets

prevent the liquids from penetrating into the cavities, leading to the so-called Cassie state (*De Gennes et al.*, 2002). In this Cassie state, liquids slip over the liquid/gas menisci (*Voronov et al.*, 2008; *Rothstein*, 2010), resulting in an apparent slip on the SH surface. This apparent slip is generally characterized by an average slip velocity, U_s, on the wall, and a slip length, L_s, defined as $U_s = L_s \partial U / \partial n_{|\partial\Omega}$, where n denotes the normal to the wall (*Voronov et al.*, 2008).

1.2.1 Experimental Results with SH Surfaces in Laminar Flow

Numerous experiments have reported DR with SH surfaces in laminar flow. With random SH roughness, DRs of 14% have been reported in laminar pipe flow (*Watanabe et al.*, 1999), 18% in laminar Taylor-Couette flow (*Watanabe et al.*, 2003), 20% in laminar boundary layer flow (*Balasubramanian et al.*, 2004) and 13% (*Watanabe et al.*, 2007) to 22% (*Papageorgiou et al.*, 2012) in laminar micro-channel flow. In laminar channel flows with arrays of LMGs on the walls, DRs of 40% have been observed when only one channel wall is covered with LMGs of size $0.01 \lesssim g/h \lesssim 0.63$ & $1 \leq g/w \leq 4$ (*Ou et al.*, 2004; *Choi et al.*, 2006; *Truesdell et al.*, 2006), and up to 50% when both channel walls are covered with LMGs of size $0 \lesssim g/H \lesssim 0.21$ & $0 \lesssim g/w \lesssim 11.1$ (*Maynes et al.*, 2007), where g and w denote the with of the SH MGs and the spacings between them, respectively, and H denotes the full height of the channel. In channel flows with arrays of transverse MGs on the walls, the results show Reynolds number dependence (*Davies et al.*, 2006), with up to 21% DR at $Re_b \approx 8.3$ in micro-channels with transverse SH MGs of size $g/H = 0.4$ & $0.67 \leq g/w \leq 1$ on one wall (*Karatay et al.*, 2013a), up to 30% DR at $4 \lesssim Re_b \lesssim 41$ with MGs of size $0.06 \lesssim g/H \lesssim 0.63$ & $0.88 \leq g/w \leq 2$ (*Hao et al.*, 2009), and up to 13% DR at $150 \leq Re_b \leq 770$ with MGs of size $4 \times 10^{-4} \lesssim g/H \lesssim 8 \times 10^{-4}$ & $0.18 \leq g/w \leq 0.83$ (*Watanabe et al.*, 2007; *Ogata and Shimizu*, 2011) when both the channel walls are covered with SH surfaces. SH surfaces with micro-pillars (*Lee et al.*, 2008) or micro-

posts (*Ogata and Shimizu*, 2011) have also been studied by different groups. It has been suggested that, in the limit of small micro-pillar sizes, when the gas fraction is large, these surfaces outperform SH surfaces with longitudinal or transverse MGs (*Davis and Lauga*, 2010). However, only few experiments have reported DR with SH micro-pillars or micro-posts. In laminar channel flow, *Ou et al.* (2004) have reported DRs of up to 40% with SH square micro-posts of size $0.12 \leq g/H \leq 1.18$ & $0.5 \leq g/w \leq 5$ on one wall, while *Ogata and Shimizu* (2011) have reported only 4% DR with SH square micro-posts of size $g/H \approx 8 \times 10^{-4}$ & $0.63 \leq g/w \leq 3.4$ on one wall.

The physics of flow over SH surfaces has been investigated using Micro-Particle Imaging Velocimetry ($\mu - \mathbf{PIV}$), optical diffraction techniques and nano-rheology. Using $\mu - PIV$, *Ou and Rothstein* (2005) showed that liquids slip along the liquid/gas interfaces between the SH MGs, while the no-slip boundary condition holds on the rest of the surface. Furthermore, their studies showed that the liquid/gas interfaces on the SH surface are not flat. Using optical diffraction techniques, *Rathgen and Mugele* (2010) showed that the interface curvature, which is caused by the pressure difference across the interface, obeys the Young-Laplace law. Nano-rheology measurements of *Steinberger et al.* (2007) in shear-driven flow on a SH surface with circular micro-posts showed that increasing the interface curvature, at positive protrusion angles, leads to a decrease of up to 241% in the resulting slip length in laminar flow, compared to that with flat interfaces. At negative protrusion angles, increasing the interface curvature in laminar flow leads to a decrease of up to 30% in the resulting slip length, compared to that with flat interfaces (*Steinberger et al.*, 2007). Based on results from $\mu - PIV$ in pressure-driven channel flow with SH LMGs, *Tsai et al.* (2009) suggested that the interface curvature leads to a drop of up to 83% in the resulting normalized slip lengths at the SH wall, compared to the values obtained with the analytical solution of *Philip* (1972a). Using $\mu - PIV$ in pressure-driven channel flow with SH transverse

MGs, *Karatay et al.* (2013a) showed that increasing the interface curvature at small positive protrusion angles, up to 10^o, leads to an increase in the resulting DRs, while increasing the interface curvature beyond protrusion angles of 10^o leads to a decrease in the resulting DRs. Furthermore, the detailed velocity measurements using $\mu - PIV$ have been used to suggest that the surface slip on the liquid/gas interfaces of the SH surface is the primary mechanism of SH DR in laminar flow (*Ou and Rothstein*, 2005).

1.2.2 Experimental Results with SH Surfaces in Turbulent Flow

Experiments with SH surfaces in turbulent flow have been less consistent. In pipe flow with SH random micro-textures on the walls experiments have shown no noticeable DR (*Watanabe et al.*, 1999). In micro-channels with arrays of SH LMGs on one or both walls, experiments have shown 0% DR with $g^{+0} \approx 0.2$, $g/w = 1$, MGs on one wall (*Peguero and Breuer*, 2009), 11% DR with $1.3 \leq g^{+0} \leq 2.5$, $g/w = 4$, MGs on one wall (*Woolford et al.*, 2009), and up to 50% DR with $0.7 \leq g^{+0} \leq 4.8$, $g/w = 1$, MGs on both walls (*Daniello et al.*, 2009), where the $+0$ superscript denotes non-dimensionalization with respect to the wall friction-velocity and kinematic viscosity of a no-slip base channel flow at the same bulk Reynolds number as the SH channel. More recently, DRs of up to 75% have been reported in turbulent boundary layer flows with LMGs of size $0.8 \lesssim g^{+0} \lesssim 1.6$ and $1 \leq g/w \leq 19$ (*Park et al.*, 2014), and up to 36% with random roughness of size $k_{rms}^{+0} \approx 0.85$ (*Ling et al.*, 2016).

Despite these remarkable results in laboratory scale experiments, SH DR has not yet evolved into a practical means of turbulent skin-friction control, because under the high shear rates and high pressure fluctuations, typical of turbulent flows, the air pockets in the surface micro-texture cannot be sustained either due to interface collapse (*Zheng et al.*, 2005; *Checco et al.*, 2014), or due to the dissolving of the air pockets into the working liquid (*Samaha et al.*, 2012; *Karatay et al.*, 2013b). This has led to the development of more advanced, hierarchical, micro/nano-textured

surfaces (*Feng et al.*, 2002; *Wang et al.*, 2007; *Kwon et al.*, 2009; *Lee and Kim*, 2009; *Cha et al.*, 2010; *Lee and Kim*, 2011) or liquid infused surfaces (*Wong et al.*, 2011; *Rosenberg et al.*, 2016). With dual scale micro/nano-textured surfaces, nano-scale textures are etched on the sides of the SH micro-textures to increase the allowable contact angles between the sides of the micro-textures and the meniscus (*Lee and Kim*, 2011). At larger contact angles, the liquid/gas meniscus can support larger pressure loads. With liquid infused surfaces, the surface micro-textures are filled with a low viscosity lubricating liquid, replacing the gas pockets in the SH surface micro-textures (*Wong et al.*, 2011). The resulting liquid layer can support large pressure loads and is more durable under high shear rates. However, the DR performance of liquid infused surfaces has so far been modest, with DRs of up to 16% at a viscosity ratio of 260 in laminar Couette flow on a liquid infused surface with micro-posts (*Solomon et al.*, 2014), and DRs of up to 15% at a viscosity ratio of 2.7 in turbulent Taylor-Couette flow on a liquid infused surface with LMGs (*Rosenberg et al.*, 2016). Furthermore, the resulting surface is still prone to drainage of the lubricating liquid into the flow under high shear rates (*Wexler et al.*, 2015).

1.2.3 Analytical and Computational Studies of SH Surfaces in Laminar Flow

Many analytical solutions have been developed for flow over the SH surfaces at the limit of low Reynolds numbers (*Philip*, 1972a,b; *Lauga and Stone*, 2003; *Davis and Lauga*, 2009; *Belyaev and Vinogradova*, 2010; *Davis and Lauga*, 2010). In these analytical solutions, gas recirculation inside the SH micro-textures is neglected and the SH surface is modeled as a pattern of flat shear-free regions interspersed among no-slip regions on a wall (*Philip*, 1972a,b; *Lauga and Stone*, 2003; *Davis and Lauga*, 2009; *Belyaev and Vinogradova*, 2010; *Davis and Lauga*, 2010). Using this assumption, *Philip* (1972a,b) developed analytical solutions for the velocity profiles in shear-driven

flows and pressure-driven channel flows at low Reynolds numbers over SH surfaces with transverse or longitudinal MGs. These analytical solutions show that the key features of flow over the SH surfaces scale with the fraction of shear-free to no-slip surface area, and the geometrical parameters of the SH surface (*Philip*, 1972a,b). These findings were further supported by analytical solutions developed by *Lauga and Stone* (2003) for the slip length in pressure-driven Stokes flow through a pipe with transverse or longitudinal MGs, and the analytical solutions developed by *Davis and Lauga* (2009, 2010) for the slip length in shear-driven Stokes flow over a SH surface with rectangular or circular micro-posts. Using the assumption of flat shear-free liquid/gas interfaces, *Feuillebois et al.* (2009) showed that for a given ratio of shear-free to no-slip surface area, SH LMGs provide the maximum apparent slip in micro-channel flows (*Feuillebois et al.*, 2009). *Belyaev and Vinogradova* (2010) extended these studies to the case of pressure-driven channel flow at low Reynolds number with SH LMGs on one wall, in which the liquid/gas interfaces on the SH surface were low-shear, rather than shear-free, supporting a locally finite slip length. By studying different orientations of the MGs with respect to the flow, *Belyaev and Vinogradova* (2010) showed that flow past the SH LMGs is controlled by the ratio of the local slip length to the MG sizes. In all these studies, the liquid/gas interfaces on the SH surface were modeled as flat.

Gas/liquid interfaces on the SH surfaces, however, are not flat (*Ou and Rothstein*, 2005; *Tsai et al.*, 2009). Measurements on the SH surfaces, using optical diffraction techniques, show that the interface curvature obeys the Young-Laplace law, up to a critical pressure, beyond which the interface irreversibly collapses (*Rathgen and Mugele*, 2010). The effect of interface curvature on SH DR has been investigated in recent analytical (*Sbragaglia and Prosperetti*, 2007; *Crowdy*, 2010, 2016) and computational (*Hyväluoma and Harting*, 2008; *Wang et al.*, 2014) studies in laminar flow. Assuming small deflections around flat shear-free interfaces, *Sbragaglia and*

Prosperetti (2007) developed an analytical solution for the slip length in pressure-driven channel flow with LMGs on one wall, at the limit of very small MG sizes and low Reynolds numbers. Using their analytical solution, *Sbragaglia and Prosperetti* (2007) showed that interface curvature provides two competing effects in laminar flow: (i) it can increase the flow rate in the channel, and the slip length, if the protrusion is negative, or decrease them if the protrusion is positive (*Sbragaglia and Prosperetti*, 2007), due to the changes in the cross-sectional area of the channel, (ii) interface curvature alters the velocity profile on top of the SH surface, resulting in a decrease in the slip length (*Sbragaglia and Prosperetti*, 2007). These studies were extended to shear-driven Stokes flow on SH surfaces with LMGs, for the limit of very small MG widths (*Crowdy*, 2010), and for MGs of arbitrary width (*Crowdy*, 2016). *Wang et al.* (2014) investigated the effect of interface curvature on the slip length in pressure-driven channel flow and pipe flows at low Reynolds numbers with SH LMGs of arbitrary sizes on the walls, using semi-analytical and computational approaches. Based on their analysis, *Wang et al.* (2014) showed that the normalized effective slip length increases monotonically with increasing the interface curvature, in the limit of vanishing micro-texture sizes. In contrast, the normalized effective slip length generally decreases with increasing the interface curvature in the limit of very large micro-texture sizes (*Wang et al.*, 2014).

1.2.4 Analytical and Computational Studies of SH Surfaces in Turbulent Flow

The first DNS studies of turbulent flow over SH surfaces were reported in turbulent channels, in which the effect of the SH surface was modeled as uniform slip on the channel walls (*Min and Kim*, 2004). DRs of up to 30% were reported with uniform streamwise slip, while a DI of up to 26% was reported with spanwise slip. In the case of combined slip in both the streamwise and spanwise directions, smaller DRs

of up to 17% were observed compared to what would be obtained with streamwise slip alone. *Busse and Sandham* (2012) later showed that the combined slip can lead to DR if the magnitude of the streamwise slip length is larger than the spanwise slip length, and DI if the spanwise slip length is larger than the streamwise slip length. However, when the streamwise slip length exceeds $L_{s_x}^{+0} \approx 3.5$, DR is observed regardless of the magnitude of the spanwise slip. *Fukagata et al.* (2006) extended the DNS studies of *Min and Kim* (2004) with uniform slip on the walls to higher Reynolds numbers, and used these DNS results to propose a parametrization of the magnitude of DR in terms of the streamwise and spanwise slip lengths and friction Reynolds number of the base flow, given by $(1/\kappa)ln(Re_{\tau_0}) + F(0) = (1 - DR)\, L_{s_x}^{+0} + (\sqrt{1 - DR}/\kappa)ln(\sqrt{1 - DR}\, Re_{\tau_0}) + \sqrt{1 - DR}\, F(\sqrt{1 - DR}\, L_{s_y}^{+0})$, where $\kappa = 0.41$ is the von Karman constant, $L_{s_x}^{+0}$ and $L_{s_y}^{+0}$ denote the streamwise and spanwise slip lengths, respectively, and F is a function of the spanwise slip length. The logarithmic law of the wall was used in the derivation of this parameterization, and the function F was determined from a curve fit to the DNS data (*Fukagata et al.*, 2006). The approximation for this function was later improved by *Busse and Sandham* (2012) through a more elaborate curve fitting to the DNS data. Later, *Seo and Mani* (2016) proposed a relationship between the streamwise and spanwise slip lengths in *Fukagata et al.* (2006) model and the SH micro-texture sizes.

Later DNS studies considered channels with SH LMGs, transverse MGs, or micro-posts on the walls. In all these studies, the liquid/gas menisci were modeled as flat shear-free interfaces. *Martell et al.* (2009) and *Martell et al.* (2010) reported DRs of up to 25% in turbulent channel flow with SH LMGs of width $16 \leq g^{+0} \leq 110$, $1 \leq g/w \leq 3$ on one wall, 0% DR with transverse MGs of width $g^{+0} \approx 34$, $g/w = 1$ on one wall, and DRs of up to 50% with square micro-posts of width $16 \leq w^{+0} \leq 55$ separated by $34 \leq g^{+0} \leq 166$. Based on their DNS results, *Martell et al.* (2010) proposed that the magnitude of SH DR in turbulent flow scales with the fraction of

shear-free to no-slip surface area and the width of the MGs in wall units. In addition, *Martell et al.* (2010) suggested that the turbulent structures are shifted but otherwise largely unaffected by the presence of the SH wall. *Park et al.* (2013) reported DRs of up to 90% in turbulent channel flow with SH LMGs of width $8.4 \leq g^{+0} \leq 885$ & $1 \leq g/w \leq 15$ on both walls. They attributed the mechanism of SH DR to significant attenuation of the near-wall streamwise vortices on the SH surface and concluded that modification of turbulence structures by the SH surface plays a more significant role in the mechanism of SH DR in turbulent flows than the direct effect resulting from the surface slip (*Park et al.*, 2013). *Jelly et al.* (2014) reported 21.6% DR in turbulent channel flow with SH LMGs of width $g^{+0} \approx 33.75$, $g/w = 1$ on both walls. Based on their DNS results, they suggested that a significant reduction in the strength of the streamwise vortical structures, together with suppression of ejection and sweep motions, occurs in the presence of the SH wall (*Jelly et al.*, 2014). *Türk et al.* (2014) reported DRs of up to 60% in turbulent channel flow with SH LMGs of width $4.4 \leq g^{+0} \leq 140.8$, $1 \leq g/w \leq 3$ on both walls. More recent studies have investigated the effect of a uniform gas layer on DR (*Jung et al.*, 2016). Using a two fluid model, in which a uniform gas layers was placed between the working fluid and the walls of a channel, *Jung et al.* (2016) studied the effect of a gas layer on DR, and suggested that increasing the gas layer thickness on the surface leads to increases in the slip length, slip velocity and the magnitude of DR. In all these studies, however, the gas/liquid interfaces on the SH surface have been modeled as 'idealized' flat boundaries, neglecting the dynamics of the liquid/gas interfaces. *Seo et al.* (2015) studied the stability of the liquid/gas interfaces on the SH surfaces, a posteriori, based on the pressure fields obtained from DNS of turbulent channel flow with 'flat' SH walls. The liquid/gas interfaces on the SH surface in their studies were modeled as a pattern of flat shear-free regions on a no-slip surface. Based on their DNS results, *Seo et al.* (2015) proposed that an upper bound exists for the SH micro-

post sizes, at $g^{+0} \approx 33$ & $w^{+0} \approx 16$, which limits the range of robust operation of the SH surfaces in turbulent flows to low Reynolds numbers.

1.3 The Present Study

Successful implementation of the SH surfaces as a turbulence control strategy in practical applications requires a detailed understanding of the scaling and mechanism of skin-friction DR with SH surfaces in turbulent flow, as well as the pressure and stress loads on the liquid/gas interfaces in the SH surfaces. This understanding is not yet at hand.

The objective of the present study is to contribute to the understanding of skin-friction DR with SH surfaces in wall-bounded turbulent flow environments, using DNS results in turbulent channel flow with SH walls. In chapter § II, the numerical methodology and simulation parameters used for the DNS studies are presented and discussed. In chapter § III the scaling and mechanism of DR in channel flows with a variety of SH micro-patterns on the walls, including LMGs, transverse MGs, and micro-posts, is investigated based on results from DNS. As with all DNS studies performed to date, the liquid/gas interfaces on the SH surface were modeled as 'idealized' flat and shear-free boundaries. In chapter § IV the effect of interface curvature on SH DR is investigated based on results from the first DNS studies performed to date of SH LMGs with curved liquid/gas interfaces. The results are compared to riblets, and it is shown that both SH LMGs and riblets have the same mechanism of DR. These are followed by a summary and conclusions in chapter § V. Possible avenues for future works are discussed in chapter § VI. The material presented in chapter § III have appeared previously in *Rastegari and Akhavan* (2013, 2015, 2016a). The materials presented in chapter § IV are in the process of publication (*Rastegari and Akhavan*, 2016b).

CHAPTER II

Numerical Methodology

2.1 The Lattice Boltzmann Method

Standard Lattice Boltzmann (LB) BGK Methods with single relaxation time (*Succi*, 2001) have been used for all the simulations reported in this thesis. The Lattice Boltzmann Method (LBM) provides an alternative approach for numerical solution of the Navier-Stokes equations. Although it first emerged as an offspring of the Lattice Gas Cellular Automata (LGCA) (*Wolf-Gladrow*, 2000), it has been shown that the LBM can also be derived directly from the Boltzmann equation (*He and Luo*, 1997). This offers a bottom up approach, from the discrete gas kinetic to the continuum hydrodynamics, for the study of fluid mechanics. The method has been the subject of rapid developments in the recent years, with the introduction of multiple relaxation times (*D'Humières et al.*, 2002), and entropic schemes (*Chikatamarla et al.*, 2006). In parallel with these advances, the domain of application of LBM has been extended to a wide variety of problems, including high Mach number (Ma), Non-Newtonian, Multi-Phase, and turbulent flows (*Chen and Doolen*, 1998; *Nourgaliev et al.*, 2003; *Aidun and Clausen*, 2010).

In its basic formulation, LBM tracks the evolution of sets of particle Distribution Function (DF)s, in space and time, based on the Boltzmann equation. The DFs represent the density of particles at time t, near point $\mathbf{x}$, with a velocity, $\mathbf{v}$. Dur-

ing the time increments of the LBM, the distributions stream and collide in space, reproducing the convective/dissipative dynamics of a fluid system.

The Boltzmann equation describes the evolution of a set of DFs in space and time, and is given by (*Wolf-Gladrow*, 2000)

$$\frac{Df}{Dt} = Q(f, f), \tag{2.1}$$

where $f(\mathbf{x}, \mathbf{v}, t)$ and $Q(f, f)$ denote the DF and the collision integral, respectively. The DFs are defined such that $f(\mathbf{x}, \mathbf{v}, t)d^3xd^3v$ represents the probability of finding a particle in the volume d^3x around the point $\mathbf{x}$, with a velocity ranging between $\mathbf{v}$ and $\mathbf{v} + d\mathbf{v}$. The collision integral, $Q(f, f)$, accounts for the inter-particle collisions, and is defined as

$$Q(f, f) = \int d^3v_1 \int d\Omega\sigma(\Omega)|\mathbf{v} - \mathbf{v}_1| \left(f(\mathbf{v}^{'})f(\mathbf{v}_1^{'}) - f(\mathbf{v})f(\mathbf{v}_1) \right), \tag{2.2}$$

with $\sigma(\Omega)$ denoting the differential collision cross section for the particle collisions which transform the velocities from $\mathbf{v}, \mathbf{v}_1$ (incoming) into $\mathbf{v}^{'}, \mathbf{v}_1^{'}$ (outgoing) (*Wolf-Gladrow*, 2000). For analytical and computational simplicity, the collision integral is usually represented with an approximate form, due to *Bhatnagar, Gross, and Krook* (1954) (BGK), as

$$Q(f, f) = -\frac{1}{\tau} \left(f(\mathbf{x}, \mathbf{v}) - f^{(0)}(\mathbf{x}, \mathbf{v}) \right). \tag{2.3}$$

The inter-particle collisions in this approximate form are modeled by a relaxation process, towards a local Equilibrium Distribution Function (EDF), $f^{(0)}(\mathbf{x}, \mathbf{v})$, with a single relaxation time, τ.

Using a finite set of discrete velocities, $\mathbf{c}_i$, the Boltzmann equation (2.1), with the BGK approximation (2.3) for its collision operator, can be discretized in space and

time to give

$$f_i(\mathbf{x}+\mathbf{c}_i\Delta t, t+\Delta t) = f_i(\mathbf{x},t) - \frac{\Delta t}{\tau}(f_i(\mathbf{x},t) - f_i^{(0)}) + \Delta t F_i, \tag{2.4}$$

where $f_i(\mathbf{x},t)$ denotes the DFs at a point $\mathbf{x}$ and time t moving with the discrete velocity $\mathbf{c}_i$s. Equation (2.4) denotes the fundamental equation of single relaxation time LBM (*Wolf-Gladrow*, 2000; *Succi*, 2001), and describes the Lagrangian motion of DFs, during a time increment Δt, within which DFs are relaxed towards a local equilibrium, $f_i^{(0)}$, and stream in space along the discrete velocity directions to the neighboring points. The relaxation time, τ, represents the time rate of this local relaxation. The force term, F_i, represents the force term per unit volume.

A uniform lattice, with spacings of Δx in all directions, is utilized for the solution of equation (2.4). The discrete velocity set, $\mathbf{c}_i$, is defined as $\mathbf{c}_i \equiv c\mathbf{e}_i$, where $c \equiv \Delta x/\Delta t$ is the lattice speed and $\mathbf{e}_i$s are the velocity vector directions. The EDF is defined as a function of the local density, ρ, and velocity, $\mathbf{u}$, by (*Succi*, 2001)

$$f_i^{(0)} = \rho w_i \left(1 + 3\frac{\mathbf{c}_i\cdot\mathbf{u}}{c^2} + \frac{9}{2}\frac{(\mathbf{c}_i\cdot\mathbf{u})^2}{c^4} - \frac{3}{2}\frac{\mathbf{u}\cdot\mathbf{u}}{c^2}\right), \tag{2.5}$$

where w_is are the lattice weight factors, which depend on the set of the discrete velocities. Both the discrete velocity set, $\mathbf{c}_i$, and the lattice weight factors, w_i, are determined based on symmetry preserving requirements (*Cao et al.*, 1997; *Succi*, 2001). The set of discrete velocities are chosen based on the trade off between the stability and computational efficiency (*Mei et al.*, 2000). The larger the set of velocities, the better the stability of the method (*Mei et al.*, 2000). However, a large set of discrete velocities increases the computational costs of the LBM. *Mei et al.* (2000) have shown that a set with 19 three dimensional velocity vectors, D3Q19, provides the best balance between the stability and computational efficiency. This set is shown in figure 2.1, and its corresponding lattice weight factors are listed in table 2.1, and is adopted

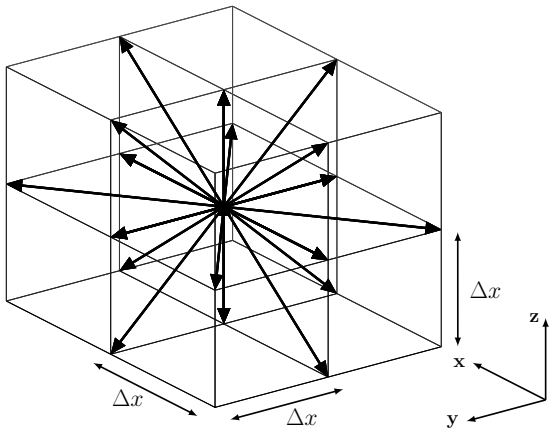

Figure 2.1: Set of discrete velocity vectors for the D3Q19 LBM

i	w_i	$\mathbf{e}_i$
0	$\frac{1}{3}$	$(0,0,0)$
$i=1,\ldots,6$	$\frac{1}{18}$	$(\pm1,0,0),(0,\pm1,0),(0,0,\pm1)$
$i=7,\ldots,18$	$\frac{1}{36}$	$(\pm1,\pm1,0),(\pm1,0,\pm1),(0,\pm1,\pm1)$

Table 2.1: Set of discrete velocity vectors, $\mathbf{e}_i$, and lattice weight factors, w_i, of D3Q19 LBM *Succi* (2001)

in all the computations in the present study.

For computational purposes, equation (2.4) is solved in two separate steps: a collision step

$$f_i^*(\mathbf{x},t) = f_i(\mathbf{x},t) - \frac{\Delta t}{\tau}(f_i(\mathbf{x},t) - f_i^{(0)}) + \Delta t F_i, \tag{2.6}$$

and a streaming step,

$$f_i(\mathbf{x}+\mathbf{c}_i\Delta t, t+\Delta t) = f_i^*(\mathbf{x},t), \tag{2.7}$$

where $f_i^*(\mathbf{x},t)$ denotes the post-collision DF. The collision step corresponds to a computationally local operation, representing the (dissipative) inter-molecular collisions in a particle based system, while the streaming step represents a non-local operation, corresponding to the spatial motion of the particles. It can be shown that in the limit of low Mach (Ma) and Knudsen (Kn) numbers, the Navier-Stokes equations are recovered by the solutions of equation (2.4) (*He and Luo*, 1997; *Succi*, 2001). The

local velocity and density are related to the moments of DFs via (*Succi*, 2001)

$$\rho = \sum_i f_i(\mathbf{x}, t), \qquad \rho\mathbf{u} = \sum_i \mathbf{c}_i f_i(\mathbf{x}, t), \tag{2.8}$$

and the viscosity of the fluid is related to the relaxation time in equation (2.4) through

$$\nu = \frac{c^2 \Delta t}{3}(\frac{\tau}{\Delta t} - \frac{1}{2}). \tag{2.9}$$

The force term, F_i, in equation (2.4) defines the magnitude of the body force per unit volume, $\mathbf{r}$, in the Navier-Stokes equations, via various expressions (*Wolf-Gladrow*, 2000; *Succi*, 2001; *Ladd and Verberg*, 2001; *Guo and Zhao*, 2002). For spatially constant but temporally variable body forces per unit volume of the domain, $\mathbf{r}(t)$, in the Navier-Stokdes equations (*Wolf-Gladrow*, 2000)

$$F_i = \frac{1}{12c^2}\mathbf{c}_i \cdot (\mathbf{r}(t) + \mathbf{r}(t + \Delta t)) \,. \tag{2.10}$$

In internal flows, this forcing function can be specified to maintain a constant friction Reynolds number, Re_τ, or a constant bulk Reynolds number, Re_b, during the course of the simulations.

2.2 Maintaining a Constant Friction Reynolds Number in LB Simulations of Channel Flows

To maintain a constant friction Reynolds number, $Re_\tau \equiv u_\tau h_{eff}/\nu$, in the channel during the course of the simulations, the average pressure gradient in the channel,

$-\langle \partial P/\partial x \rangle$, should be specified as

$$-\langle \frac{\partial P}{\partial x} \rangle = \frac{\rho u_\tau^2}{h_{eff}}, \\ = \left(\frac{u_\tau^2}{c^2}\right)\left(\frac{\rho c^2}{\Delta x}\right)\left(\frac{\Delta x}{h_{eff}}\right), \tag{2.11}$$

where $\langle\,\rangle$ denotes averaging in the periodic directions in the domain, $u_\tau = \sqrt{\tau_w/\rho}$ is the wall friction velocity, h_{eff} is the volume averaged half-height of the channel, and ρ is the density of the fluid. Given the magnitude of the pressure gradient, the body force term in equation (2.4), is specified in 'lattice units' as

$$F_i = -\frac{1}{6c^2}\left(\frac{\Delta x}{\rho c^2}\right)\langle \frac{\partial P}{\partial x} \rangle \mathbf{c}_i \cdot \mathbf{e}_x, \\ = -\frac{1}{6c^2}\left(\frac{u_\tau^2}{c^2}\right)\left(\frac{\Delta x}{h_{eff}}\right)\mathbf{c}_i \cdot \mathbf{e}_x, \tag{2.12}$$

where $\mathbf{e}_x$ denotes the unit vector in the streamwise direction, and u_τ/c is specified as described in section § 2.6. Using the Chapman-Enskog expansion, it can be shown that the resulting scheme provides second order accuracy in space and time (*Wolf-Gladrow*, 2000).

2.3 Maintaining a Constant Bulk Reynolds Number in LB Simulations of Channel Flows

Despite the great potential of LBM for studying turbulent wall-bounded flows (*Chen and Doolen*, 1998; *Eggels*, 1996; *Amati et al.*, 1997; *Lammers et al.*, 2006; *Premnath et al.*, 2009), no method for imposing a constant bulk Reynolds number in LB simulations has been described in the literature before. Here, a method is proposed for imposing and maintaining a constant bulk Reynolds number in LB simulations of channel flows which are periodic in the streamwise and spanwise directions.

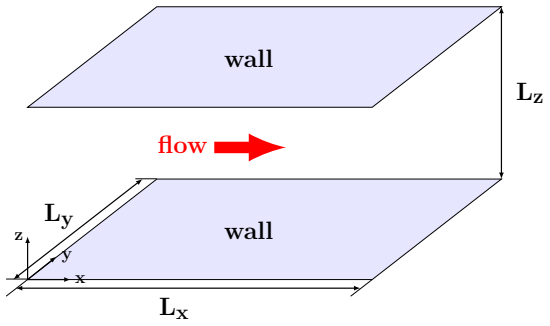

Figure 2.2: Schematic of the problem domain

For flow in a channel, similar to that in figure 2.2, with periodicity in the streamwise and spanwise directions, and no penetration condition on the walls, $\mathbf{u}\cdot\mathbf{n}|_{wall} = 0$, where $\mathbf{n}$ denotes the unit normal vector on the walls, the integral form of the momentum equation reads

$$\mathbf{R} = \frac{\partial}{\partial t}\int_{CV} \rho\mathbf{u}dx^3, \tag{2.13}$$

where $\mathbf{R} = (R_x, R_y, R_z)$, and $\mathbf{u} = (u_x, u_y, u_z)$ denote the the resultant force and velocity vectors, respectively, and the flux terms, $\int_{\partial B}\rho\mathbf{u}\mathbf{u}\cdot d\mathbf{A}$, on the right hand side are equal to zero due to periodicity.

To maintain a constant bulk Reynolds number, $Re_b \equiv q/2\nu$, where q denotes the flow rate per unit spanwise width of the channel, a force equivalent to the resultant force, $\mathbf{R}$, in equation (2.13), should be applied to the flow. The magnitude of the force, R_α, in the alpha-direction should thus satisfy

$$\int_t^{t+\Delta t} R_\alpha dt = \int_{CV}\rho u_\alpha dx^3|_{t+\Delta t} - \int_{CV}\rho u_\alpha dx^3|_t. \tag{2.14}$$

For incompressible flows, or low Mach number ($Ma \ll 1$) compressible flows, the streamwise component of equation (2.14) can be written as

$$\int_t^{t+\Delta t} R_x dt = \rho q_{|_{t+\Delta t}} L_x L_y - \int_{CV}\rho u_x dx^3|_t, \tag{2.15}$$

where L_x and L_y denote the channel lengths in the periodic streamwise and spanwise directions, respectively. Therefore, the force per unit volume of the domain is given by

$$\int_t^{t+\Delta t} r_x dt = \rho q_{|_{t+\Delta t}} \frac{L_x L_y}{\mathscr{V}} - \frac{\int_{CV} \rho u_x dx^3|_t}{\mathscr{V}}. \tag{2.16}$$

where $\mathscr{V} \equiv \int_{CV} dx^3$ denotes the volume of the domain. Using the second order trapezoidal rule, the left side of equation (2.16) can further be expanded to give

$$\frac{\Delta t}{2}\left(r_x(t+\Delta t) + r_x(t)\right) = \frac{\rho q_{|_{t+\Delta t}}}{2h_{eff}} - \frac{\int_{CV} \rho u_x dx^3|_t}{\mathscr{V}} + O(\Delta t^2). \tag{2.17}$$

where $h_{eff} \equiv \dfrac{\mathscr{V}}{2L_x L_y}$ denotes the volume-averaged half-height of the channel.

Similar equations can be derived for other components of the force if a net flow rate in those directions is desired. In the simulations that are reported in this thesis, however, the only non-zero component of the force is in the streamwise direction.

In time marching algorithms for solving the Navier-Stokdes equation, such as LBM, at each time step t, the magnitude of the second term on the right hand side of equation (2.17), $\int_{CV} \rho u_x dx^3|_t/\mathscr{V}$, is known. To impose a constant bulk Reynolds number, $Re_b = q/2\nu$, the magnitude of $q_{|_{t+\Delta t}}$ in the first term should then be set equal to the target flow rate per unit width, q. The force term, F_i, in equation (2.4) of the LBM can be specified using equation (2.10), as

$$F_i = \frac{1}{6c\Delta t}\left(\rho\left(\frac{q}{2c\Delta x}\right)\left(\frac{\Delta x}{h_{eff}}\right) - \left(\frac{\int_{CV} \rho u_x dx^3|_t}{c\Delta x^3}\right)\left(\frac{\Delta x^3}{\mathscr{V}}\right)\right)\mathbf{c}_i \cdot \mathbf{e}_x, \tag{2.18}$$

where $\dfrac{q}{2c\Delta x}$ is specified as described in section § 2.6.

Using the Chapman-Enskog expansion on the basis of ϵ, where ϵ is proportional to the Knudsen number, Kn, it can be shown that the resulting scheme is second

order in space and time (*Wolf-Gladrow*, 2000). Given the expansions

$$f_i = f_i^{(0)} + \epsilon f_i^{(1)} + \epsilon^2 f_i^{(2)} + O(\epsilon^3), \tag{2.19a}$$

$$\mathbf{r} = \epsilon \mathbf{r}, \tag{2.19b}$$

$$\frac{\partial}{\partial t} = \epsilon \frac{\partial}{\partial t_0} + \epsilon^2 \frac{\partial}{\partial t_1}, \tag{2.19c}$$

$$\nabla = \epsilon \nabla_1, \tag{2.19d}$$

where $f_i^{(0)}$ denotes the EDF and the leading order of $\mathbf{r}$ is assumed proportional to ϵ (*Guo and Zhao*, 2002), setting $\Delta \mathbf{x}_i = \Delta t \mathbf{c}_i$, Taylor series expansions of the equations (2.4) and (2.18) around the point $\mathbf{x}$ and time t, use of the expansions (2.19), and separation of the resulting terms based on the order of ϵ, leads to

$$O(\epsilon^0): \quad f_i^{(0)} = f_i^{(0)}, \tag{2.20a}$$

$$O(\epsilon^1): \quad D_i^{(0)} f_i^{(0)} = -\frac{1}{\tau} f_i^{(1)} + \frac{1}{6c^2} \mathbf{c}_i \cdot \mathbf{r}, \tag{2.20b}$$

$$O(\epsilon^2): \quad \frac{\partial}{\partial t_1} f_i^{(0)} + \left(1 - \frac{\Delta t}{2\tau}\right) D_i^{(0)} f_i^{(1)} = -\frac{1}{\tau} f_i^{(2)}, \tag{2.20c}$$

where $D_i^{(0)} \equiv \partial/\partial t_0 + \mathbf{c}_i \cdot \nabla_1$. Assuming that the perturbations from equilibrium do not contribute to the mass and momentum (*Wolf-Gladrow*, 2000), i.e.

$$\sum_i f_i^{(1)} = 0, \quad \sum_i \mathbf{c}_i f_i^{(1)} = 0, \tag{2.21a}$$

$$\sum_i f_i^{(2)} = 0, \quad \sum_i \mathbf{c}_i f_i^{(2)} = 0, \tag{2.21b}$$

taking the first and the second moments of the equation (2.20b) in the velocity space

leads to the Euler equations,

$$\frac{\partial \rho}{\partial t_0} + \nabla_1 \cdot \rho \mathbf{u} = 0, \tag{2.22a}$$

$$\frac{\partial \rho \mathbf{u}}{\partial t_0} + \nabla_1 \cdot \mathbf{\Pi}^{(0)} = \mathbf{r}, \tag{2.22b}$$

where $\mathbf{\Pi}^{(0)} \equiv \sum \mathbf{c}_i \mathbf{c}_i f_i^{(0)}$. Using the properties of the lattice tensors (*Wolf-Gladrow*, 2000), and the definition of the EDF, the tensor $\mathbf{\Pi}^{(0)}$ can be evaluated as $\mathbf{\Pi}^{(0)} = \rho \mathbf{u}\mathbf{u} + \rho c^2/3$.

The same procedure with the equation (2.20c) leads to

$$\frac{\partial \rho}{\partial t_1} = 0, \tag{2.23a}$$

$$\frac{\partial \rho \mathbf{u}}{\partial t_1} + \left(1 - \frac{\Delta t}{2\tau}\right) \nabla_1 \cdot \mathbf{\Pi}^{(1)} = 0, \tag{2.23b}$$

where $\mathbf{\Pi}^{(1)} \equiv \sum_i \mathbf{c}_i \mathbf{c}_i f_i^{(1)}$. Equation (2.20b), together with the equation (2.22), can be used to evaluate this tensor, resulting in

$$\mathbf{\Pi}^{(1)} = -\rho\tau \frac{c^2}{3} \left(\nabla_1 \mathbf{u} + \nabla_1 \mathbf{u}^T\right) + O(Ma^2), \tag{2.24}$$

where $Ma \equiv \sqrt{3} u_{max}/c$ denotes the Mach number, defined based on u_{max}, the maximum velocity in the simulations. The terms of $O(Ma^2)$ are of the same order as the compressibility error of the LBM, and the resulting scheme would provide a deviatoric stress tensor, $\sigma \equiv (1 - 1/\tau) \sum_i \mathbf{c}_i \mathbf{c}_i f_i^{(1)}$, of $O(Ma^2)$, which has the same order of accuracy as the LBM without a forcing term (*Krüger et al.*, 2010).

Substitution of equation (2.24) into the equation (2.23b) and combining equations

(2.22) and (2.23) gives rise to the Navier-Stokes equations,

$$\frac{\partial \rho}{\partial t} + \nabla \cdot \rho \mathbf{u} = 0, \tag{2.25a}$$

$$\frac{\partial \rho \mathbf{u}}{\partial t} + \nabla \cdot \rho \mathbf{u}\mathbf{u} = -\nabla p + \nabla \cdot \left(\rho \nu (\nabla \mathbf{u} + \nabla \mathbf{u}^T)\right) + \mathbf{r}, \tag{2.25b}$$

with the kinematic viscosity, ν, defined by the equation (2.9), and pressure, p, defined as $p \equiv \rho c^2/3$. Terms of the order of $O(\Delta t^2, \epsilon^3, Ma^2)$ have been truncated in the process of the derivation of these equations, hence the resulting scheme is second order in time and space.

2.4 Improving the Accuracy of LBM Using Grid Embedding

To improve the accuracy of the computations near the walls, while maintaining the computational cost at a reasonable level, grid-embedding (*Filippova and Hänel*, 1998; *Lagrava et al.*, 2012; *Touil et al.*, 2014) can be used for the simulations. With grid embedding, conformal patches of fine grids replace the coarser grid in the near wall region, as shown in figure 2.3(a). The flow variables density, ρ, velocity, $\mathbf{u}$, and viscosity, ν, are maintained continuous across the grids. This requires the lattice speed, $c = \Delta x/\Delta t$, to be kept constant on both grids. As a result, the time step size, Δt, and the relaxation time, τ, of the fine grid depend on those of the coarse grid through (*Filippova and Hänel*, 1998; *Lagrava et al.*, 2012)

$$\Delta t_{fine\,grid} = \frac{\Delta t_{coarse\,grid}}{GR}, \tag{2.26}$$

$$\frac{\tau_{fine\,grid}}{\Delta t_{fine\,grid}} = \frac{1}{2} + GR\left(2\frac{\tau_{coarse\,grid}}{\Delta t_{coarse\,grid}} - 1\right), \tag{2.27}$$

where $GR = \Delta x_{coarse\,grid}/\Delta x_{fine\,grid}$ denotes the Grid-embedding Ratio.

Standard LBM is used on both grids. With a grid-embedding ratio of GR, each step of computations begins with one iteration over the coarse grid, followed by GR

iterations over the fine grid, corresponding to the difference between the time step sizes of the grids (*Filippova and Hänel*, 1998; *Lagrava et al.*, 2012). The time step size of the simulation corresponds to the time step size of the coarse grid. With each iteration over the coarse grid, its DFs are advanced from time t to the time $t + \Delta t$. The iterations over the fine grid, advance its DFs to times $t + \Delta t/GR, t + 2\Delta t/GR, ..., t + GR\Delta t/GR$, consecutively. On the transition between the grids, the incoming distribution functions are transfered from the adjacent grid. To reduce the artificial disturbances associated with the data transfer between the grids, fine grid and coarse grid are overlapped on each other (*Lagrava et al.*, 2012), as shown in figure 2.3(b). Fine grid is attached to the second layer of the coarse grid, while the coarse grid is extended $GR + 1$ layers inside the fine grid. Transfer from the fine to the coarse grid is a straightforward copy of the distribution functions to the corresponding destination sites. Due to the difference between the time step sizes and the resolutions of the grids, however, transfer from the coarse to the fine grid requires interpolation, in both time and space. Second order Lagrangian interpolation in time, between the times $t - \Delta t$ and $t + \Delta t$, and third order bi-cubic interpolation in space, using the 27 nearest points on the coarse grid to the point on the fine grid, are used for data transfer between the grids in all the simulations reported in this thesis. In addition, to account for the differences in grid resolutions, during the data transfer the non-equilibrium part of the DFs, $f_i^{ne} = (f_i - f_i^{(0)})$, need to be rescaled (*Filippova and Hänel*, 1998; *Lagrava et al.*, 2012). In transfers from the fine to the coarse grid, non-equilibrium DFs are scaled by (*Filippova and Hänel*, 1998)

$$\alpha = GR \frac{(1 - \frac{\Delta t_{coarse\,grid}}{\tau_{coarse\,grid}})(\frac{\Delta t_{fine\,grid}}{\tau_{fine\,grid}})}{(1 - \frac{\Delta t_{fine\,grid}}{\tau_{fine\,grid}})(\frac{\Delta t_{coarse\,grid}}{\tau_{coarse\,grid}})}. \tag{2.28}$$

In transfers from coarse to the fine grid, on the other hand, non-equilibrium DFs are scaled by $1/\alpha$ (*Filippova and Hänel*, 1998). As a result, a transfer from coarse to the

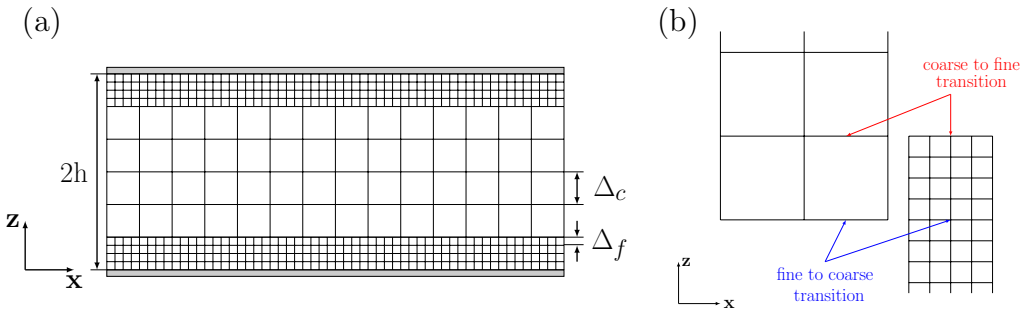

Figure 2.3: Schematic of grid embedding strategy with a grid-embedding ratio of $GR = 4$: (a) side view of the channel; (b) side view of the grid transitions.

fine grid corresponds to

$$f_{i,\,coarse\,grid} = f_i^{(0)} + \alpha f^{ne}_{i,\,fine\,grid}, \tag{2.29}$$

and a transfer from fine to the coarse grid corresponds to

$$f_{i,\,fine\,grid} = f_i^{(0)} + \frac{1}{\alpha} f^{ne}_{i,\,coarse\,grid}. \tag{2.30}$$

Both these rescaling steps preserve the mass and momentum conservation (*Lagrava et al.*, 2012). It should be noted that the equilibrium DF, $f_i^{(0)}$, remain the same, on both the coarse and fine grids, as is required by equation (2.5), due to the continuity of the mass and velocity across the solution domain.

2.5 Boundary Conditions

During the the streaming step of the LB iterations, DFs at each lattice site are updated from the adjacent sites. For the grid points next to the boundaries, however, a complete set of adjacent points does not exist. Various boundary treatment schemes have been suggested to deal with this problem (*Succi*, 2001). In this thesis, half-way bounce back (*Succi*, 2001), local specular reflection (*Ginzburg and Steiner*, 2003) and Central Linear Interpolation (CLI) (*Ginzburg et al.*, 2008) schemes have been used

to impose the no-slip condition on flat boundaries, the free-slip condition on flat or curved boundaries, and the no-slip condition on curved boundaries, respectively.

With the half-way bounce back scheme, the DFs leaving the grid point next to the boundary, 'bounce back' on the wall, returning back to their original lattice site along the opposite velocity vector,

$$f_{-i}(\mathbf{x}, t + \Delta t) = f_i^*(\mathbf{x}, t), \quad if\ \{\mathbf{x} + \mathbf{e}_i\} \in wall, \tag{2.31}$$

as seen in figure 2.4(a), where $-i$ corresponds to the lattice velocity vector $\mathbf{e}_{-i}$ in the opposite direction of $\mathbf{e}_i$, i.e. $\mathbf{e}_{-i} = -\mathbf{e}_i$ (*Succi*, 2001). The bounce back scheme reproduces the no-slip condition on the wall, with second order accuracy, provided that the wall is flat and located exactly in the middle of the grid points (*Succi*, 2001).

With local specular reflection, the DFs leaving the grid point next to the boundary experience a mirror like reflection on the wall,

$$f_{\bar{i}}(\mathbf{x}, t + \Delta t) = f_i^*(\mathbf{x}, t), \quad if\ \{\mathbf{x} + \mathbf{e}_i, \mathbf{x} + \mathbf{e}_{-\bar{i}}\} \in wall, \tag{2.32}$$

as seen in figure 2.4(b), where $\bar{i}$ corresponds to the lattice velocity vector $\mathbf{e}_{\bar{i}}$ in the mirror direction of $\mathbf{e}_i$, i.e. $\mathbf{e}_{\bar{i}} = \mathbf{e}_i - 2(\mathbf{e}_i \cdot \mathbf{n})\mathbf{n}$, and $\mathbf{n}$ denotes the normal to the wall (*Ginzburg and Steiner*, 2003). For grid points in the corners, where two or more mirror directions coincide, the arithmetic mean of all those coinciding DFs is used (*Ginzburg and Steiner*, 2003). The specular reflection scheme reproduces the free-slip condition on the wall, with second order accuracy, provided that the wall is flat, parallel to the grid lines, and located exactly in the middle of the grid points (*Ginzburg and Steiner*, 2003). When dealing with curved surfaces or flat surfaces that are not parallel to the grid lines, a stair-step approximation of the surface is used with local specular reflection, to impose the shear-free boundary condition. With this approximation, the order of accuracy of the boundary condition reduces to one (*Ginzburg and Steiner*,

2003).

The CLI scheme is used to impose the no-slip boundary condition, on curved walls or flat walls which are not parallel to the grid lines, with the second order accuracy (*Ginzburg et al.*, 2008). In this scheme, a combination of DFs of the boundary point and a point in its neighborhood is used for symmetric linear interpolation of the DFs along the lattice velocity vector,

$$f_{-i}(\mathbf{x}, t+\Delta t) = f_i^*(\mathbf{x}, t) + \gamma f_i^*(\mathbf{x} - \mathbf{e}_i \Delta x, t) - \gamma f_{-i}^*(\mathbf{x}, t), \quad if\ \{\mathbf{x}+\mathbf{e}_i\} \in wall, \quad (2.33)$$

where $\gamma = (1-2\delta_i)/(1+2\delta_i)$ is the wigthing factor in the interpolation, with $\delta_i \leqslant 1$ corresponding to the fraction of lattice link which sits inside the fluid domain, $\delta_i = \delta/\Delta$, where Δ and δ denote the full length of the lattice link, and the length of the part which sits inside the fluid domain, respectively, as seen in figure 2.4(c).

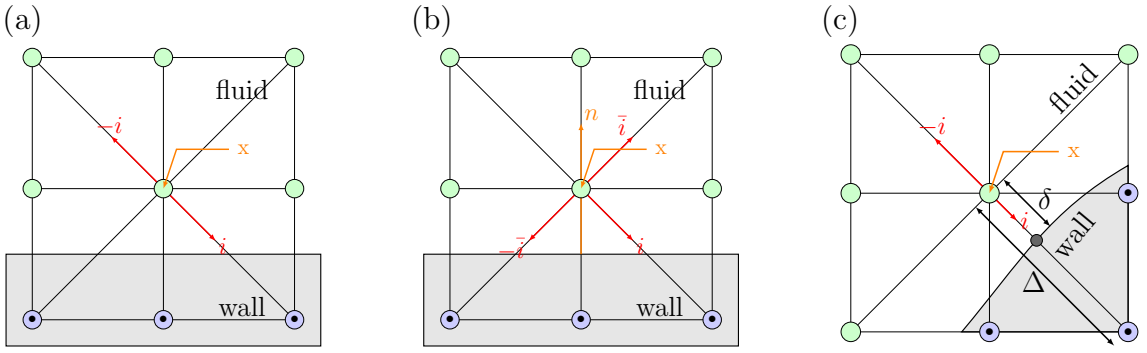

Figure 2.4: Boundary conditions for the LB simulations: (a) half-way bounce back, (b) specular reflection, (c) CLI; ●, fluid grid points; ●, wall grid points.

2.6 Parametrization

To perform fluid flow simulations with LBM, the relaxation time, τ, grid spacing, Δx, and the time step size, Δt, need to be assigned. It is common in the literature to express these parameters in 'lattice units', for which the variables are non-dimensionalized with respect to the grid spacing, Δx, the time step size, Δt, and

the density, ρ.

In simulations in which the bulk Reynolds number, $Re_b = \frac{q}{2\nu}$, is specified, where q denotes the volume flow rate per unit spanwise width in the channel, and ν is the kinematic viscosity, respectively, the relaxation time, τ, in lattice units, can be defined from equation (2.9) as

$$\begin{aligned}\frac{\tau}{\Delta t} =& \frac{3\nu}{c\Delta x} + \frac{1}{2}, \\ =& (\frac{3}{Re_b})(\frac{q}{2c\Delta x}) + \frac{1}{2}.\end{aligned} \tag{2.34}$$

where the lattice speed, $c = \Delta x/\Delta t = 1$ in 'lattice units'. The magnitude of $\frac{q}{2c\Delta x}$ determines the Courant Friedrichs Lewy (CFL) condition in the simulations. The CFL number is defined as

$$\begin{aligned}CFL &= \Delta t \frac{U_{max}}{\Delta x}, \\ &= \frac{U_{max}}{c},\end{aligned} \tag{2.35}$$

where U_{max} denotes the maximum velocity in the domain. It has been suggested that LBM remains stable, for CFL numbers as high as 0.25 (*Lammers et al.*, 2006). Large CFL numbers correspond to large time step sizes, and thus large temporal errors. As a result, in this thesis a small CFL number of $CFL = 0.1$ or $CFL \approx 0.1$ has been used for all the simulations. Given the CFL number, analytical or experimental relations between the bulk velocity and maximum velocity in the channel can be used to find the magnitude of $\frac{q}{2c\Delta x}$ in equations (2.34) and (2.15). In laminar channel

flow, analytical solution of the Navier-Stokdes equations give

$$\begin{aligned}\frac{q}{2c\Delta x} &= (\frac{q}{2ch_{eff}})(\frac{h_{eff}}{\Delta x}),\\ &= (\frac{U_b}{c})(\frac{h_{eff}}{\Delta x}),\\ &= \frac{2}{3}(\frac{U_{max}}{c})(\frac{h_{eff}}{\Delta x}),\\ &= \frac{2}{3}(CFL)(\frac{h_{eff}}{\Delta x}).\end{aligned} \tag{2.36}$$

In turbulent channel flow, experimental correlation of *Dean* (1978) suggests that

$$\begin{aligned}\frac{q}{2c\Delta x} &= (\frac{q}{2ch_{eff}})(\frac{h_{eff}}{\Delta x}),\\ &= (\frac{U_b}{c})(\frac{h_{eff}}{\Delta x}),\\ &= 0.788(\frac{U_{max}}{c})Re_b^{0.0116}(\frac{h_{eff}}{\Delta x}),\\ &= 0.788(CFL)Re_b^{0.0116}(\frac{h_{eff}}{\Delta x}).\end{aligned} \tag{2.37}$$

It should be noted that with this parameterization, in channel flow simulations with micro-textured walls, the magnitude of the CFL condition is set to $CFL \approx 0.1$. The slight deviation of the CFL condition, from 0.1, is caused by the changes in the magnitude of the bulk velocity, U_b, as a result of the changes in the cross sectional area of the channel due to the presence of the micro-textures on the walls. In the simulations of fully developed steady state laminar flows, or stationary turbulent flows, however, this slight deviation does not have any effect on the results.

When flow is driven by a constant pressure gradient, the magnitude of the relaxation time in lattice units is determined based on the friction Reynolds number of

the flow, $Re_\tau = u_\tau h_{eff}/\nu$, using the equation (2.9),

$$\begin{aligned}\frac{\tau}{\Delta t} =& \frac{3\nu}{c\Delta x} + \frac{1}{2}, \\ =& (\frac{3}{Re_\tau})(\frac{h_{eff}}{\Delta x})(\frac{u_\tau}{c}) + \frac{1}{2}.\end{aligned} \tag{2.38}$$

where u_τ denotes the wall-friction velocity in the channel. The magnitude of the CFL number can then be determined from analytical or experimental relations between u_τ and U_{max}. In laminar channel flow, analytical solutions give

$$\begin{aligned}(\frac{u_\tau}{c})(\frac{h_{eff}}{\Delta x}) &= 2(\frac{U_{max}}{c})Re_\tau^{-1}(\frac{h_{eff}}{\Delta x}), \\ &= 2(CFL)Re_\tau^{-1}(\frac{h_{eff}}{\Delta x}),\end{aligned} \tag{2.39}$$

while in turbulent channel flow, experimental correlations suggest that (*Dean*, 1978)

$$\begin{aligned}(\frac{u_\tau}{c})(\frac{h_{eff}}{\Delta x}) &= 0.110(\frac{U_{max}}{c})Re_\tau^{-0.1296}(\frac{h_{eff}}{\Delta x}), \\ &= 0.110(CFL)Re_\tau^{-0.1296}(\frac{h_{eff}}{\Delta x}).\end{aligned} \tag{2.40}$$

The total number of iterations required to reach a non-dimensional time of one, as defined by $TU_{max}/h = 1$, is given by

$$\begin{aligned}\frac{T}{dt} &= \frac{h}{\Delta t U_{max}}, \\ &= \frac{h}{\Delta x}\frac{c}{U_{\max}}, \\ &= \frac{h}{\Delta x}\frac{1}{CFL}.\end{aligned} \tag{2.41}$$

In turbulent flow simulations, at a bulk Reynolds number of $Re_b = 3600$, statistical steady state is achieved after around 100 non-dimensional times, $TU_{max}/h = 100$, corresponding to around 6 eddy turnover times, Tu_τ/h, after initialization of the

flow. The simulations are continued afterwards, for about 300 non-dimensional times, $TU_{max}/h = 300$, corresponding to 18 eddy turnover times, Tu_τ/h, to provide enough statistical samples for data analyses.

For a well-resolved DNS, the magnitude of the grid spacing, Δx, should be of the same order as the kolmogorov scale, η. For fully developed turbulent channel flow, it can be shown that $\eta^+ \approx 1.5$ (*Pope*, 2000), where + denotes non-dimensionalization with respect to the wall-friction velocity, u_τ, and the kinematic viscosity of the flow, ν. In this thesis, a grid spacing of $\Delta x^+ \lesssim 2$, corresponding to $\Delta x/h \lesssim 2/Re_\tau$, has been used for all the simulations. This grid spacing is comparable to those used in LB DNS of turbulent channel flow by other investigators (*Lammers et al.*, 2006; *Bespalko et al.*, 2012).

2.7 Initialization

Without proper initialization with appropriate disturbance fields, LB DNS in channel flow results in a laminar solution, regardless of the Re_b. To achieve turbulent flow, LB DNS can be initialized in two ways, using the turbulent velocity and pressure fields resulting from Direct Numerical Simulation (DNS) with other numerical schemes, such as pseudo-spectral methods, or from the velocity and pressure fields which correspond to laminar flow plus a superposition of finite-amplitude 2D and infinitesimal secondary 3D eigenmodes of the Orr-Sommerfeld equation, as described in *Orszag and Patera* (1983).

With either set of initial conditions, the DFs for LB DNS can be initialized using first order approximations obtained from the Chapman-Enskog expansions (2.19), given by

$$f_i \approx f_i^{(0)} + \epsilon f_i^{(1)}. \tag{2.42}$$

Here, $f_i^{(0)}$ denotes the EDF, defined in terms of the local velocity and density through

the equation (2.5), and $\epsilon f_i^{(1)}$ can be approximated by (*Latt*, 2007; *Latt and Chopard*, 2008)

$$\epsilon f_i^{(1)} \approx -\frac{3\tau w_i}{c^2}\left(\mathbf{Q}_i : \rho\nabla\mathbf{u} - \mathbf{c}_i\nabla : (\rho\mathbf{u}\mathbf{u}) + \frac{3}{2c^2}(\mathbf{c}_i \cdot \nabla(\mathbf{Q}_i : \rho\mathbf{u}\mathbf{u})\right), \tag{2.43}$$

where the tensor $\mathbf{Q}_i$ is defined as $\mathbf{Q}_i = \mathbf{c}_i\mathbf{c}_i - c^2/3\mathbf{I}$, with $\mathbf{I}$ denoting the identity tensor, $\mathbf{u}$ is the macroscopic velocity field, and the density, ρ, is related to the pressure field through $p = \rho c^2/3$. In practice, the non-linear terms in equation (2.43) can be neglected, resulting in the linear approximation

$$\epsilon f_i^{(1)} \approx -\frac{3\tau w_i}{c^2}\left(\mathbf{Q}_i : \rho\nabla\mathbf{u}\right), \tag{2.44}$$

which reproduces the same stress tensor as equation (2.43) (*Latt and Chopard*, 2008).

Second order finite difference approximations were utilized to evaluate the derivatives in equations (2.43) or (2.44), using the given velocity and pressure fields. The results were then used to initialize the DFs.

2.8 Domain Decomposition and Parallelization

A two dimensional domain decomposition strategy was used to parallelize the LB simulations that are presented in this thesis. Specifically, the simulation domain was divided into a two dimensional array of sub-domains, in a toroidal topology, as shown in figures 2.5. To perform the simulations, each sub-domains was assigned to a separate processor of a parallel computer. The decomposition of the domain does not have any effect on the collision step, due to the locality of the collisions. For the streaming step, however, the DFs leaving a sub-domain are transfered to the neighboring sub-domain during a data transfer step, for which the MPI2 routines are employed (*Gropp et al.*, 1999). Using the persistent non-blocking communication

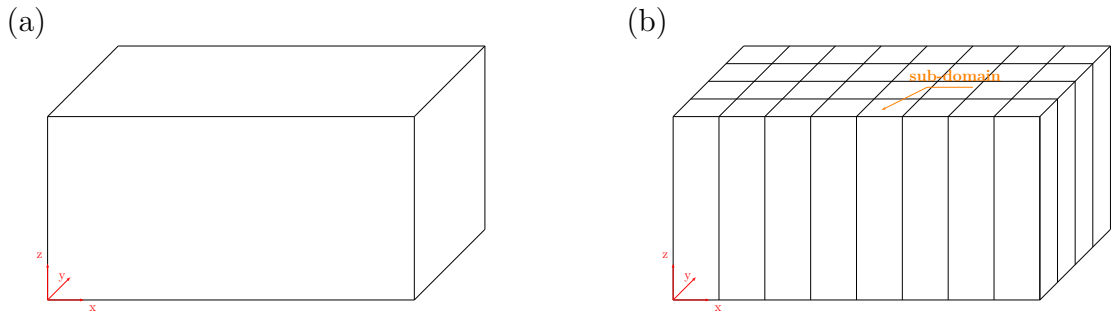

Figure 2.5: Domain Decomposition for the LB DNS of channel flow: (a) base domain; (b) partitioned domain;

mode to overlap the communications with the computations at the lowest message overhead, the parallel performance of the code has been maximized (*Gropp et al.*, 1999). The single process performance of the LBM was also optimized significantly using cache optimization and vectorization (*Wilke et al.*, 2003; *Wellein et al.*, 2006).

The parallel performance of the code was tested in a turbulent channel flow, corresponding to the geometry of the planned studies, both with grid embedding and without it. This would present, in addition, the gains and overheads associated with the grid embedding strategy. Use of the grid embedding is necessary for the simulations presented in this thesis, due to the small size of the SH micro-grooves. The simulations were performed in channel of size $5h \times 2.5h \times 2h$ in the streamwise , spanwise, and wall-normal directions, respectively, at a bulk Reynolds number of $Re_b = q/2\nu = 3600$ corresponding to $Re_\tau = u_\tau h/\nu \approx 223$. The simulations without grid refinement was performed with resolutions of $1024 \times 512 \times 223$, in the streamwise, spanwise and wall-normal directions, respectively, corresponding to a uniform grid spacing of $\Delta^+ \approx 2$ wall units in all three directions. In tests of LBS DNS with grid-embedding, a grid spacing of $\Delta_c^+ \approx 2$ wall units on the coarse grid, and $\Delta_f^+ \approx 1$ wall units on the fine grid, were used, corresponding to a grid refinement ratio of 2. The resolutions used for the tests correspond to grid resolutions of $2048 \times 1024 \times 28$ (nw) / $1024 \times 512 \times 195$ (core)/ $2048 \times 1024 \times 28$ (nw) and $2048 \times 1024 \times 120$ (nw) /

$1024 \times 512 \times 103$ (core) / $2048 \times 1024 \times 120$ (nw), in the streamwise, spanwise and wall-normal directions, respectively, and 'nw' denotes the region near the wall, for which the finer grid was used.

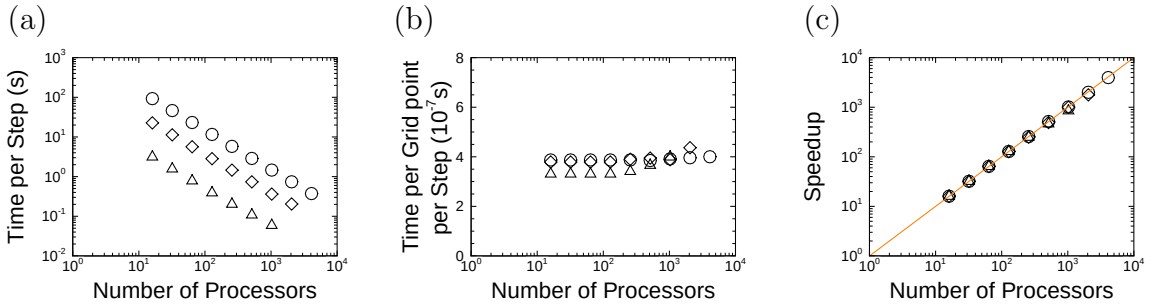

Figure 2.6: Parallel performance of the LB code on TACC DELL Linux Cluster (STAMPEDE) for DNS of turbulent channel flow: (a) CPU time per step vs. number of processors, (b) time per grid point per step vs. number of processors, (c) speedup. △, LB DNS without grid-embedding in small channel, resolution $512 \times 256 \times 223$; ◊, LB DNS with grid-embedding, $GR = 4$, in small channel, resolution $2048 \times 1024 \times 120$ (nw)/ $512 \times 256 \times 103$ (core)/ $2048 \times 1024 \times 120$ (nw); ◯, LB DNS with grid-embedding, $GR = 4$, in large channel, resolution $8192 \times 4096 \times 120$ (nw)/ $2048 \times 1024 \times 103$ (core)/ $8192 \times 4096 \times 120$ (nw); ——, ideal linear speedup.

Figure 2.6 displays the results of the tests in terms of parallel performance, based on results obtained on TACC DELL Linux cluster (Stampede). Figure 2.6(a) shows the drop of the cpu time spent per each time step of the simulation, as more processors are used. In figure 2.6(b) the time spent per each grid point per each time step of the simulation are presented, revealing the minimal overhead associated with grid embedding. Despite the presence of overhead associated with data transfer and interpolations required in the grid-embedding scheme, the time spent per each grid point per time step goes form 3.6×10^{-7} to 4.5×10^{-7} (sec), for all the cases, indicating less than 25% overhead for grid-embedding. Figure 2.6(c) shows the resulting parallel speedup. Based on these results, it can be concluded that LBM codes used in this thesis achieve a parallel efficiency of at least 97% on up to 1024 processes, suggesting that the code scales well on thousands of processors of TACC Stampede.

2.9 Verification of Numerical Methods

A number of numerical tests were performed to verify the validity and accuracy of the LB simulations. These tests include error convergence studies of LB DNS of Hagen-Poiseuille flow and laminar open channel flow at zero Froude number, $Fr = 0$, comparisons of LB DNS, grid-embedded LB DNS and pseudo-spectral DNS results in turbulent channel flow with no-slip walls, comparisons of LB DNS results and experiments in turbulent open channel flow at zero Froude number, $Fr = 0$, and comparisons of LB DNS results, experiments, and analytical solutions in laminar channel flow with 'idealized' flat or curved Super-Hydrophobic (SH) Longitudinal Micro-Groove (LMG)S on the walls. These test are described below.

The second order accuracy of the proposed scheme was verified through the convergence studies on the L_2 norm of the relative error,

$$L_2(\mathbf{e}_u) = \sqrt{\frac{\sum |u_{an} - u_{sim}|^2}{\sum |u_{an}|^2}}, \tag{2.45}$$

for LB simulations in Hagen-Poiseuille flow and in laminar open channel flow at zero Froude number, $Fr \equiv U_b/\sqrt{gH} = 0$, where u_{an} and u_{sim} denote the velocity profiles from the analytical solution and its corresponding LB simulation, respectively, and H and g represent the full height of the channel and the gravitational acceleration, respectively. Simulations were performed by maintaining a constant mass flow rate between two parallel walls, with periodicity imposed in the streamwise and spanwise directions, and no-slip or free slip conditions on the walls. Each set of simulations was performed at bulk Reynolds numbers of $Re_b = 25$ and 250. Half way bounce back (*Succi*, 2001) and specular reflection (*Benzi et al.*, 2006; *Ginzburg and Steiner*, 2003) schemes were used for imposing the no-slip and slip boundary conditions in the simulations, respectively. A set of wall-normal lattice resolutions of $N_z = h/\Delta x = 10$, 20, 40 and 80 was used for the studies. The corresponding resolutions in the

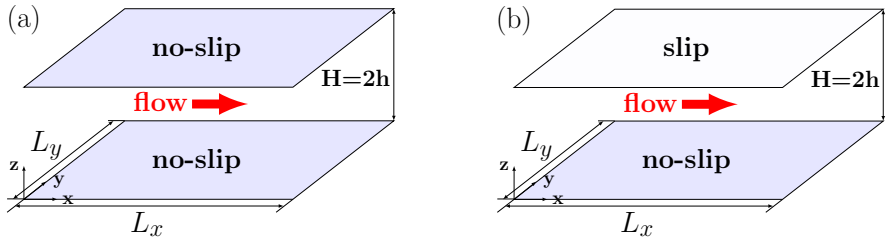

Figure 2.7: Schematic of the channels used in the simulations: (a) channel flow with no-slip walls; (b) open channel flow.

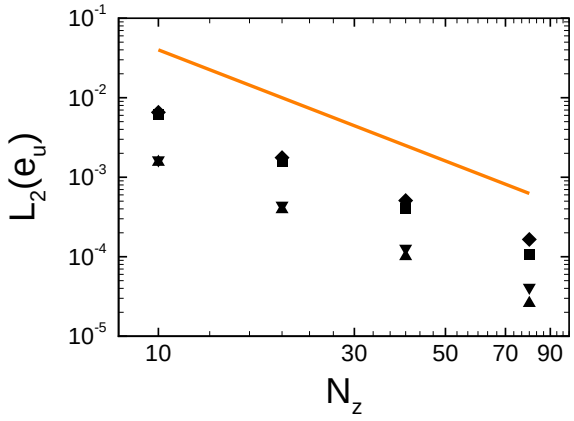

Figure 2.8: Convergence of the L_2 norm of the relative error, in LB simulations of Hagen-Poiseuille flow and zero Froude number open channel flow at constant mass flow rate: ■, ♦, Hagen-Poiseuille flow, $Re_b = q/2\nu = 25$ and 250, respectively; ▲, ▼, zero Froude number open channel flow, $Re_b = q/2\nu = 25$ and 250, respectively; ——, the second order slope.

streamwise and spanwise directions were irrelevant, due to the spatial periodicity, and thus were set to 1. To obtain second order convergence in the LB simulations on successively refined grids, it is necessary to perform all the simulations with a similar relaxation time (*Holdych et al.*, 2004). To ensure this, the CFL number in the simulations needs to be varied (*Holdych et al.*, 2004). Consequently, corresponding to the set of wall-normal lattice resolutions, a set of CFL numbers of $CFL = 0.1$, 0.05, 0.025, and 0.0125 were used for the simulations. The second order convergence in the L_2 norm of the relative error is shown in figure 2.8.

The accuracy of LBM in turbulent flow was verified through comparison of the

results from LB DNS in turbulent channel flow with results from pseudo-spectral DNS and experiments. Three cases were studied, corresponding to turbulent channel flow with no-slip walls in a small and a large channel, and turbulent open channel flow at zero Froude number. The simulations in turbulent open channel flow were performed without grid-embedding. The simulations in turbulent channel flow with no-slip walls were performed with grid embedding, in a small channel, and without grid-embedding, in a small and a large channel, to assess the accuracy of the grid-embedding strategy, and investigate the effect of the channel size on the results.

LB DNS of turbulent channel flow with no-slip walls was performed at a bulk Reynolds number of $Re_b = 3600$, corresponding to a friction Reynolds number of $Re_\tau \equiv u_\tau h/\nu \approx 227$, based on Dean's correlation (*Dean*, 1978). A channel of size $L_x \times L_y \times L_z = 5h \times 2.5h \times 2h$ in the streamwise, spanwise and wall-normal directions, respectively, was used for LB DNS in small channel and pseudo-spectral DNS, as shown in Fig. 2.7(a). A channel of size $L_x \times L_y \times L_z = 20h \times 10h \times 2h$ in the streamwise, spanwise and wall-normal directions, respectively, was used for LB DNS in large channel. A uniform Fourier grid in the streamwise and spanwise directions, with resolutions of $\Delta_x^+ \approx 8$ and $\Delta_y^+ \approx 4$, respectively, and a Chebyshev grid, with a resolution of $0.07 \lesssim \Delta_z^+ \lesssim 4.5$, in the wall-normal direction, was used for the pseudo-spectral DNS. For the LB DNS without grid- embedding, in small and large channels, the lattice spacing was set at $\Delta^+ \approx 2$. The corresponding lattice resolutions were $512 \times 256 \times 221$ in the streamwise, spanwise and wall-normal directions, respectively, for the simulations in small channel, and $2048 \times 1024 \times 221$ in the streamwise, spanwise and wall-normal directions, respectively, for the simulations in large channel. For the LB DNS with grid-embedding, lattice spacings of $\Delta_c^+ \approx 2$ and $\Delta_f^+ \approx 0.5$ were used on the coarse grid at $z^+ \gtrsim 30$ and the fine grid at $z^+ \lesssim 30$, respectively, corresponding to a grid ratio of $GR = 4$. Half way bounce back scheme was utilized for imposing the no-slip conditions on the walls (*Succi*, 2001). The simulations were initialized

from fully developed turbulent velocity and pressure fields obtained from DNS of turbulent channel flow with pseudo-spectral methods. The statistical steady state in LB DNS results was established within 100 non-dimensional times, $tU_c/h = 100$. Results were averaged over a statistical window of $tU_c/h = 300$ afterwards. This time span corresponds to 18 eddy turnover times, $tu_\tau/h \approx 18$. LB DNS without grid-embedding, when driven under a constant mass flow rate, results in a skin-friction coefficient of $C_f \equiv \tau_w/0.5\rho U_b^2 = 0.007686$ in small channel, and a skin-friction coefficient of $C_f = 0.007765$ in the large channel, which are within 1% and 0.6% of $C_f = 0.007610$ predicted by pseudo-spectral DNS in small channe, respectively, and within 3% and 2% of $C_f = 0.007925$ predicted by Dean's correlation (*Dean*, 1978), respectively, while LB DNS with grid-embedding and $GR = 4$, in small channel, predicted a friction coefficient of $C_f = 0.007603$ within 0.1% and 4.1% of the C_f predicted by pseudo-spectral DNS, and Dean's correlation (*Dean*, 1978), respectively, as shown in figure 2.9(a).

Figure 2.9(b-h) show the comparison of results from LB DNS, with and without grid-embedding, with results from pseudo-spectral DNS in turbulent channel flow with now slip walls at $Re_b = 3600$. The corresponding Re_τ values are 223, and 224, for the LB DNS without grid-embedding, in small and large channels, respectively, and 222, and 222, for LB DNS with grid-embedding, and pseudo-spectral DNS, in small channels, respectively. The normalized profiles of the mean streamwise velocity, $\bar{U}^+$, turbulence intensities, $(\overline{u_i^2}^{1/2})^+$, and Reynolds shear stress, $\overline{uw}^+$, match with those of pseudo-spectral DNS to within 1% error, as shown in figures 2.9(b-e). The normalized profiles of the root-mean-square (rms) pressure fluctuations, $(\overline{p^2}^{1/2})^+$, however, were within 4% and 6% of that from the pseudo-spectral DNS in LB DNS without grid-embedding and with grid-embedding, respectively, as shown in figure 2.9(f). This deviation is caused by $O(Ma^2)$ terms (*Qian and Orszag*, 1993; *Lammers et al.*, 2006). Similar errors have been reported in LB DNS of turbulent channel flow with imposed

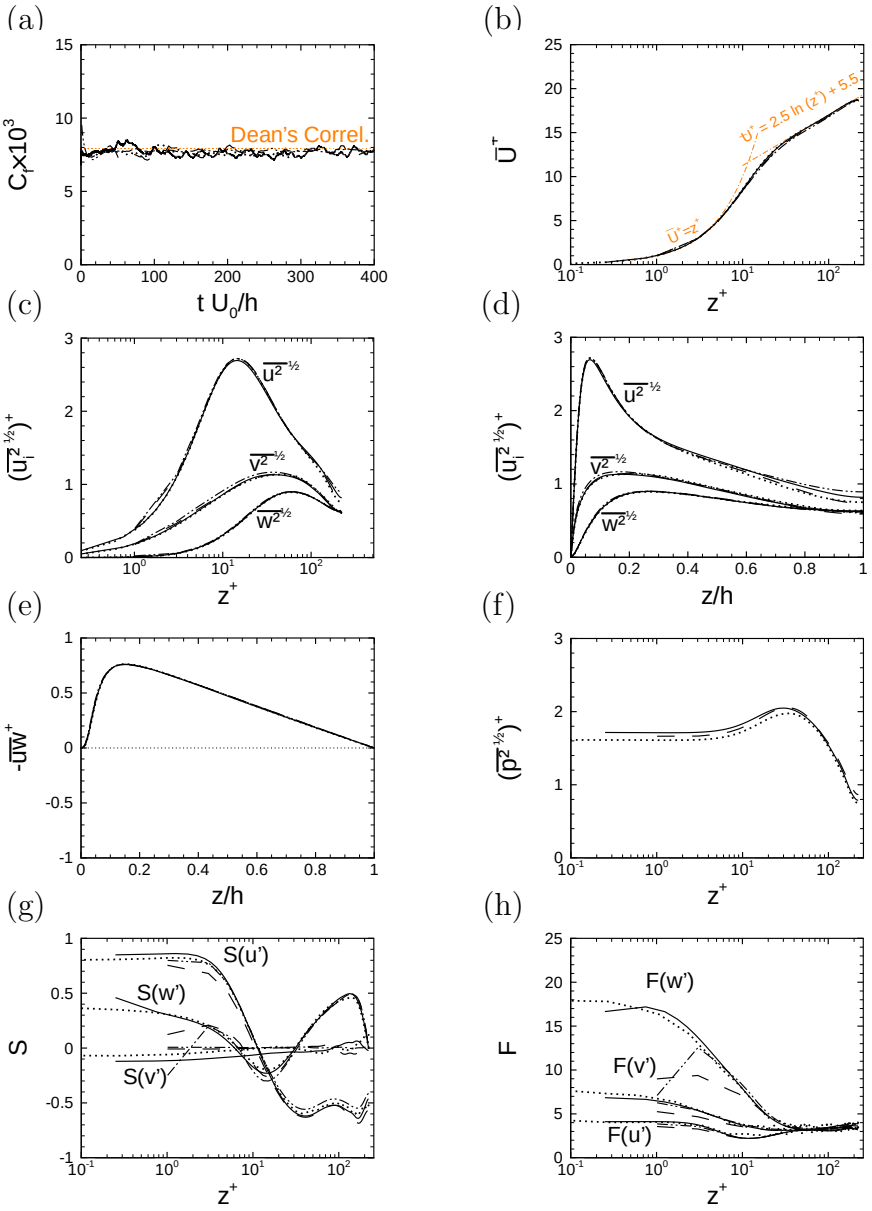

Figure 2.9: LB DNS of turbulent channel flow with no-slip walls compared to pseudo-spectral DNS and Dean's experimental correlation (*Dean*, 1978): (a) skin-friction coefficient, C_f; (b) mean velocity profile, $\overline{U}^+$; (c,d) rms velocity fluctuations, $\overline{u_i^2}^{1/2+}$; (e) Reynolds shear stresses, $\overline{uw}^+$; (f) rms pressure fluctuations, $\overline{p^2}^{1/2+}$; (g) skewness; (h) flatness; - - -, LB DNS without grid-embedding, in small channel; $-\cdot\cdot-\cdot\cdot-$, LB DNS without grid-embedding, in large channel; ——, LB DNS with grid-embedding, $GR = 4$ up to $z^+ \approx 30$, in small channel; $\cdots$, pseudo-spectral DNS, in small channel.

constant pressure gradient by other investigators (*Lammers et al.*, 2006; *Premnath et al.*, 2009; *Bespalko et al.*, 2012). The skewness profiles, shown in figure 2.9(g), agree well with those of pseudo-spectral DNS, except for LB DNS results without grid-embedding, in small and large channels, at $z^+ \lesssim 5$, where LB DNS without grid-embedding does not have adequate resolution. Using grid-embedding in LB DNS remedies this shortcoming. Similarly, the flatness profiles, shown in figure 2.9(h), also agree well with those of pseudo-spectral DNS, except for LB DNS results without grid-embedding, in small and large channels, at $z^+ \lesssim 10$, due to its relativly coarse resolution in this region.

Figure 2.10 shows the profiles of two point velocity correlations, $R_{\alpha\alpha}$, with separation in streamwise, Δx, or spanwise, Δy, directions, defined as

$$R_{\alpha\alpha}(\Delta x, z) = \frac{\langle \overline{u_\alpha(x,y,z) u_\alpha(x+\Delta x,y,z)} \rangle}{\langle \overline{u_\alpha(x,y,z) u_\alpha(x,y,z)} \rangle}, \tag{2.46}$$

$$R_{\alpha\alpha}(\Delta y, z) = \frac{\langle \overline{u_\alpha(x,y,z) u_\alpha(x,y+\Delta y,z)} \rangle}{\langle \overline{u_\alpha(x,y,z) u_\alpha(x,y,z)} \rangle} \tag{2.47}$$

and the one dimensional energy spectra, as a function of the streamwise, k_x, and spanwise, k_y, wave numbers, defined as

$$E_{\alpha\alpha}(k_x, z) = \frac{2}{\pi} \langle \overline{\tilde{u}_\alpha(k_x,k_y,z) \tilde{u}^*_\alpha(k_x,k_y,z)} \rangle, \tag{2.48}$$

$$E_{\alpha\alpha}(k_y, z) = \frac{2}{\pi} \langle \overline{\tilde{u}_\alpha(k_x,k_y,z) \tilde{u}^*_\alpha(k_x,k_y,z)} \rangle, \tag{2.49}$$

where $\tilde{u}_\alpha(k_x, k_y, z)$ denotes the two-dimensional Fourier transform of $u_\alpha(x, y, z)$,

$$\tilde{u}_\alpha(k_x, y, z) = \int_{-\infty}^{\infty} \int u(x,y,z) e^{-2\pi\sqrt{-1}(k_x x + k_y y)} dx dy, \tag{2.50}$$

which is evaluated by a real to complex Fast Fourier Transform (FFT) (*Frigo and Johnson*, 1998), and the superscript $*$ denotes the complex conjugate.

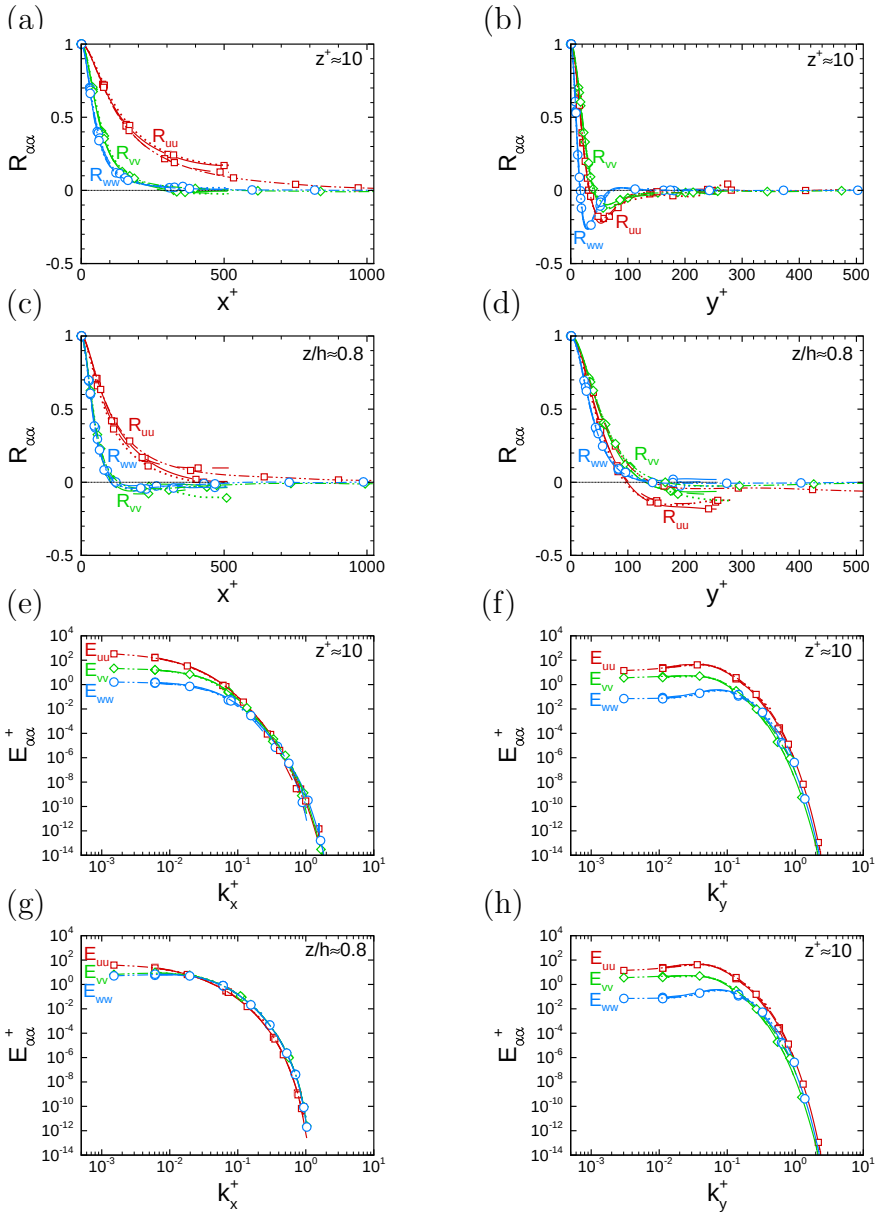

Figure 2.10: Two point velocity autocorrelations and one dimensional energy spectra in LB DNS of turbulent channel flow with no-slip walls compared to pseudo-spectral simulations: (a-d) two point velocity autocorrelations, $R_{\alpha\alpha}$; (e-h) one dimensional energy spectra, $E^{+}_{\alpha\alpha}$; −−□−−, −−◇−−, −−○−−, LB DNS on uniform grid, streamwise, uu, spanwise, vv, and wall-normal, ww, components, respectively; −··−□−··−, −··−◇−··−, −··−○−··−, LB DNS in large channel on uniform grid, streamwise, uu, spanwise, vv, and wall-normal, ww, components, respectively; —□—, —◇—, —○—, grid-embedded LB DNS, streamwise, uu, spanwise, vv, and wall-normal, ww, components, respectively; ···□···, ···◇···, ···○···, pseudo-spectral DNS, streamwise, uu, spanwise, vv, and wall-normal, ww, components, respectively.

The two point correlations in figures 2.10(a,c,e,g) all agree well with those obtained from pseudo-spectral DNS. Near the walls, at $z^+ \approx 10$, for both the LB DNS and pseudo-spectral DNS, all the two point velocity correlations drop to zero at large streamwise and spanwise separations, save for the streamwise velocity correlation as a function of streamwise separation, $R_{uu}(\Delta x^+, z^+)$, as seen in figures 2.10(a,c). This behavior of $R_{uu}(\Delta x^+, z^+)$, is caused by the small channel sizes used for the simulations. The streamwise separation at which $R_{uu}(\Delta x^+, z^+)$ drops to zero corresponds to the length of the streamwise velocity streaks, of ~ 1000 wall units (*Smith and Metzler*, 1983). As a result, due to the imposed periodicity in the streamwise direction, a channel twice as long as the streamwise velocity streaks, of ~ 2000 wall units, is required for $R_{uu}(\Delta x^+, z^+)$ to drop to zero. The small channel used for the simulations, with a streamwise length of $L_x^+ \approx 1024$, however, can only contain one full size streak. As a result, $R_{uu}(\Delta x^+, z^+)$ does not drop to zero in this channel. All correlations, including the $R_{uu}(\Delta x^+, z^+)$, however, agree well with those obtained in the large channel, as seen in figures 2.10(a-d), suggesting that the small channel sizes have not had any effect on the turbulence structures. The streamwise velocity correlation, $R_{uu}(\Delta x^+, z^+)$, drops to zero at the streamwise separation of $\Delta x^+ \approx 1000$, for LB DNS in the large channel. Figure 2.10(b) shows that the streamwise velocity correlation, R_{uu}, obtains its local minimum at a spanwise separation of $\Delta y^+ \approx 55$, predicting an average streak-spacing of 110 wall units, in agreement with the predictions of pseudo-spectral DNS and the numerical simulations of *Kim et al.* (1987). In addition, figure 2.10(c) shows that the wall-normal velocity correlation obtains its local minimum at a spanwise separation of $\Delta y^+ \approx 28$, predicting an average diameter of 28 wall units for the near wall streamwise vortices. This is also in good agreement with the prediction of pseudo-spectral DNS, and the observations made by other investigators (*Kim et al.*, 1987). Furthermore, away from the walls, at $z/h \approx 0.8$, all the correlations obtained from LB DNS without grid-embedding in the small and large channels, and from LB

DNS with grid-embedding in the small channel, agree well with those obtained from the pseudo-spectral DNS in the small channel, as seen in figures 2.10(c,d), suggesting that the size of the large scales of the turbulence have been predicted correctly in the simulations. The one dimensional energy spectra in figures 2.10(e-h), also, show good agreement between the results obtained from LB DNS without grid-embedding in small and large channels, those obtained from LB DNS with grid-embedding in a small channel, and those obtained from pseudo-spectral DNS in a small channel, for the entire range of the wave numbers.

To test the validity of the slip BCs in turbulent flow, simulations were performed in turbulent open channel flow, at zero Froude number, driven under a constant mass flow rate, and the results were compared to experimental data of *Komori et al.* (1993). These simulations were performed at a bulk Reynolds number of $Re_b \equiv U_b H/\nu = 4000$, corresponding to a $Re_\tau \equiv u_\tau H/\nu \approx 250$ in channels of size $L_x \times L_y \times L_z = 2.5H \times 2.5H \times H$ in the streamwise, spanwise and wall-normal directions, respectively, where H is the full channel height. Shear-free and no-slip boundary conditions were imposed on the top and bottom walls of the channel, respectively, as shown in figure 2.7(b). Half-way bounce back (*Succi*, 2001) and specular reflection (*Benzi et al.*, 2006; *Ginzburg and Steiner*, 2003) schemes were utilized for implementing the no-slip and free slip boundary conditions, respectively. Simulations were performed with a resolution of $512 \times 256 \times 221$ in the streamwise, spanwise and wall-normal directions, respectively, corresponding to lattice spacings of $\Delta^+ \approx 1.1$.

The simulation was initialized from fully developed turbulent flow field resulting from LB DNS in turbulent channel flow with no-slip walls. Once a fully developed turbulent state was established in the open channel, the results were averaged over a time window of $tU_c/h = 300$, corresponding to $tu_\tau/h \approx 19$, or 19 eddy-turnover times.

Figure 2.11 shows the results from LB DNS compared to LDA measurements

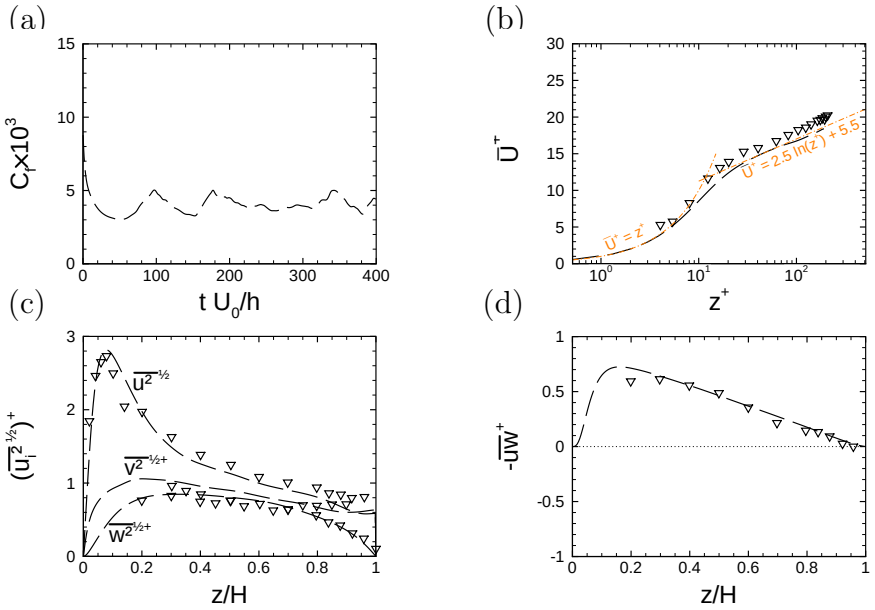

Figure 2.11: LB DNS of zero Froude number turbulent open channel flow compared to the LDA of *Komori et al.* (1993) for turbulent open channel flow: (a) skin-friction coefficient, C_f; (b) mean velocity profile, $\overline{U}^+$; (c) rms velocity fluctuations, $\overline{u_i^2}^{1/2+}$; (d) Reynolds shear stresses, $\overline{uw}^+$; —— ——, LB DNS of zero Froude number turbulent open channel flow at $Re_b = U_b H/\nu = 4000$; $\bigtriangledown$, LDA in turbulent open channel at $Re_b = U_b H/\nu \approx 3000$ (*Komori et al.*, 1993).

of *Komori et al.* (1993) in a low Froude number turbulent open channel at $Re_b = q/2\nu = U_b H/2\nu \approx 1500$ ($Re_\tau = u_\tau H/\nu \approx 160$). The normalized profiles of the mean streamwise velocity, $\bar{U}^+$, turbulence intensities, $(\overline{u_i^2}^{1/2})^+$ and the Reynolds shear stress, $\overline{uw}^+$, show a similar behavior as in turbulent channel flow with no-slip walls, as is expected for turbulent open channel flows at low Fr numbers (*Borue et al.*, 1995). Here + denotes non-dimensionalization with respect to the wall-friction velocity of the no-slip wall, $u_{\tau_{no-slip}}$, and the kinematic viscosity of the flow, ν. Near the no-slip wall, the normalized profiles of the mean streamwise velocity, $\bar{U}^+$, turbulence intensities, $(\overline{u_i^2}^{1/2})^+$ and the Reynolds shear stress, $\overline{uw}^+$, all agree with the LDA mesurements, to within the accuracy of the measurements, as seen in figures 2.11(b-d). LB DNS predicts the existence of a linear viscous sub-layer, and a logarithmic layer, in the normalized mean velocity profile, and the location of the maximum in the normalized profiles of the turbulence intensities, at $z^+ \approx 15$, in agreement with the experiments of *Komori et al.* (1993), as seen in figures 2.11(b,c). Near the free surface, however, LB DNS under-predicts the normalized magnitudes of the mean velocity, and the turbulence intensities, compared to the experiments of *Komori et al.* (1993), as seen in figures 2.11(b-c). This error arises from the difference of the Reynolds numbers, in the LB DNS and the experiments, and the possible fluctuations of the interface in the experiments. LB DNS, however, predicts an isotropic behavior for the streamwise and spanwise turbulence intensities, near the free surface, in agreement with the experiments (*Komori et al.*, 1993), as seen in figure 2.11(c).

The accuracy of LB DNS in the presence of SH walls was verified by performing simulations in laminar channel flows with 'idealized', flat longitudinal arrays of slip/no-slip stripes on one wall, and comparing the results to the analytical solution of *Philip* (1972a) and experimental data of *Ou and Rothstein* (2005). The results are shown in figure 2.12. LB DNS predicts Drag Reduction (DR)s, slip lengths, and slip velocities in agreement with the analytical solution of *Philip* (1972b), as shown in

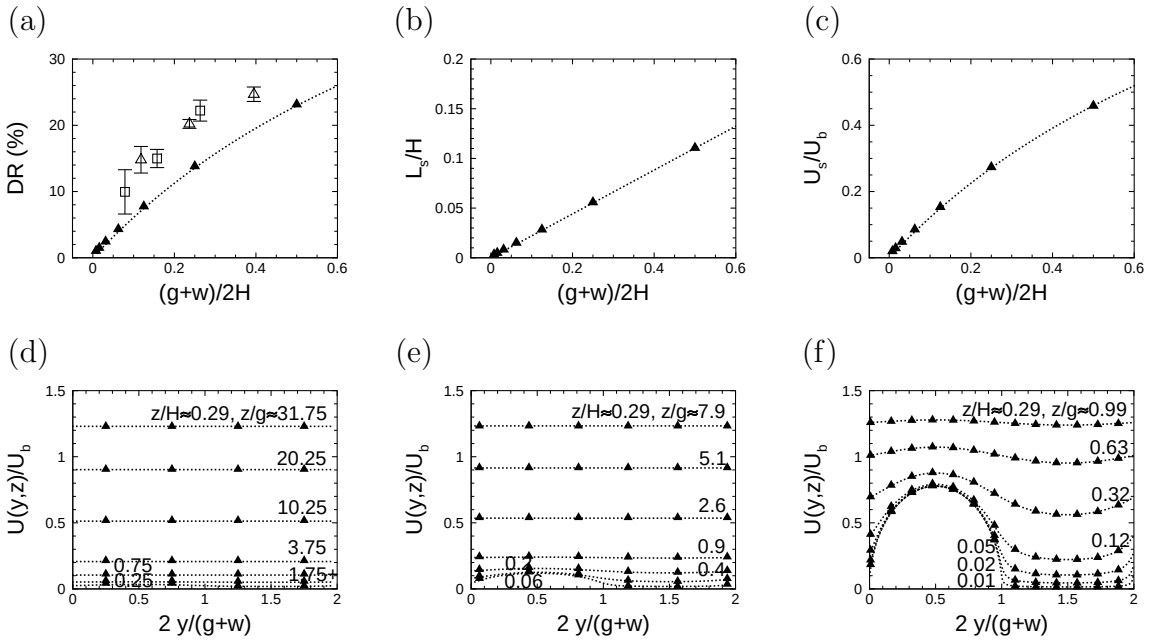

Figure 2.12: Verification of LB DNS in laminar channel flow with idealized, flat SH stripes on one wall: (a) percent drag reduction; (b) ratio of slip length to channel height; (c) ratio of slip velocity to bulk velocity; (d,e,f) spanwise variation of the streamwise velocity at different wall-normal locations: (d) $(g+w)/2H = 0.009$, $(1.1\%DR)$, (e) $(g+w)/2H = 0.036$, $(2.8\%DR)$, (f) $(g+w)/2H = 0.29$, $(15.6\%DR)$, $0 < 2y/(g+w) < 1$ slip surface, $1 < 2y/(g+w) < 2$ no-slip surface; ▲, LB DNS at $Re_b = q/2\nu = U_bH/2\nu = 50$, longitudinal slip/no-slip stripes with $g = w$ on one wall; △, experiments of *Ou and Rothstein* (2005) in laminar flow, longitudinal micro-grooves with $g = w$ on one wall; $\cdots$, analytical solution of *Philip* (1972a,b), longitudinal slip/no-slip stripes with $g = w$ on one wall.

figure 2.12(a-c). Here DR is defined as $DR = (C_f^0 - C_f)/C_f^0$, where C_f is the average skin-friction coefficient on the two channel walls, one of which has the slip/no-slip pattern and the other is a regular no-slip wall, and C_f^0 is the skin-friction coefficient in a channel at the same Re_b with no-slip walls. Experiments show similar trends in DR, but the magnitudes of DRs are slightly higher. The presence of the SH surface gives rise to a spanwise variation in the mean streamwise velocity, which persists up to a distance of $z \approx g$ from the SH wall, as shown in figures 2.12(d-f). These variations are also predicted by the analytical solution of *Philip* (1972a), as shown in figures 2.12(d-f).

Finally, to verify the accuracy of LB DNS on curved gas/liquid SH interfaces, simulations were performed in laminar channel flow with SH LMGs with static curved liquid/gas interfaces on both the walls, and the results were compared with the numerical simulations of *Wang et al.* (2014). Similar to that in numerical simulations of *Wang et al.* (2014), the liquid/gas interfaces on the SH LMGs in the LB DNS studies were modeled as curved shear-free interfaces, with the curvature of the interfaces obtained from the solutions of the Young-Laplace equation. The simulations were performed with Micro-Groove (MG)s of size $(g + w)/2H = 0.049$ & $g/w = 1$, corresponding to the MG sizes in the simulations of *Wang et al.* (2014). Three different interface curvatures of $\kappa/g = 1$, 1.732, and 2, corresponding to interface protrusion angles of $\theta = -30^o$, -60^o and -90^o, respectively, were chosen for the studies, where κ is the interface curvature, and interface protrusion angle is measured as shown in fig-

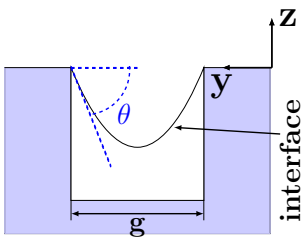

Figure 2.13: Front view of LMG with the interface protrusion.

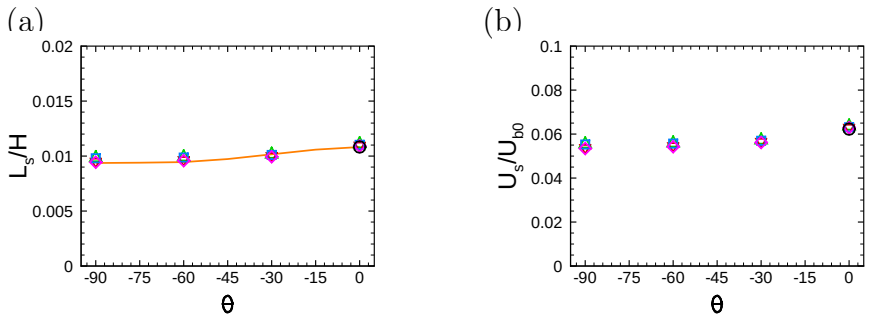

Figure 2.14: Grid resolution studies in laminar channel flow with SH LMGs of size $g/w = 1$ & $(g+w)/2H = 0.049$ with curved liquid/gas interfaces on both walls: (a) L_s/H; (b) U_s/U_{b_0}; ○, analytical solution of *Philip* (1972b); △, LB DNS without grid-embedding, $\Delta/g = 1/32$; ▽, LB DNS without grid-embedding, $\Delta/g = 1/64$; □, LB DNS with grid-embedding, $\Delta/g = 1/32$, $GR = 4$; ◇, LB DNS with grid-embedding, $\Delta/g = 1/64$, $GR = 4$; ——, numerical simulations of *Wang et al.* (2014).

ure reffig:element. A constant flow rate, corresponding to a bulk Reynolds number of $Re_b = q/2\nu = 150$, was maintained in the channel for the simulations. Grid resolution studies were performed using LB DNS with and without grid-embedding, for grid sizes of $\Delta/g = 1/32$ & $1/64$ in the simulations without grid-embedding and grid sizes of $\Delta_f/g = 1/32$ & $1/64$ and $GR = \Delta_c/\Delta_f = 4$ in the simulations with grid-embedding. Figures 2.14(a,b) show the resulting slip lengths, L_s/H, and slip velocities, U_s/U_{b_0}, obtained with the two grids, where U_{b_0} denotes the bulk flow velocity of a base channel flow with no-slip walls at the same flow Reynolds number, $Re_b = q/2\nu$, as the SH channel. For comparison, results from the simulations of *Wang et al.* (2014) are also shown in figure 2.14(a). Grid independence was achieved with $\Delta/g = 1/64$ for all the protrusion angles studied. LB DNS results show grid-independence with less than 3.5% difference between the two grid resolutions. Furthermore, LB DNS results with and without grid-embedding at a given grid resolution show agreement to within 0.7%.

CHAPTER III

SH Surfaces with 'Idealized' Flat Liquid/Gas Interfaces

3.1 Magnitude of DR in Channel Flow with Idealized SH walls

As a first step in the study of turbulent DR with SH surfaces, SH surfaces have been modeled as 'idealized' surfaces (*Martell et al.*, 2010; *Park et al.*, 2013; *Jelly et al.*, 2014; *Türk et al.*, 2014). With 'idealized' SH surfaces, the liquid/gas interfaces on the SH micro-textures are modeled as flat, shear-free areas interspaced among no-slip regions on the wall. For steady, fully-developed, turbulent flow in a homogeneous channel, with any periodic pattern of 'idealized' SH micro-texture on the walls, the streamwise Reynolds-averaged momentum equation is given by

$$\frac{\partial}{\partial x}(\nu\frac{\partial \bar{U}}{\partial x} - \overline{uu} - \bar{U}\bar{U}) + \frac{\partial}{\partial y}(\nu\frac{\partial \bar{U}}{\partial y} - \overline{uv} - \bar{U}\bar{V}) + \frac{\partial}{\partial z}(\nu\frac{\partial \bar{U}}{\partial z} - \overline{uw} - \bar{U}\bar{W}) = \frac{1}{\rho}\frac{\partial \bar{P}}{\partial x} \tag{3.1}$$

where the overbar denotes Reynolds-averaging, $\bar{U}$, $\bar{V}$, $\bar{W}$ and u, v, w denote the streamwise (x), spanwise (y), and wall-normal (z) components of the mean and fluctuating velocity fields, respectively, and $\bar{P}$ denotes the mean pressure. A similar

equation also applies in laminar flow, but with $\overline{V}$, $\overline{W}$, $\overline{uv}$ and $\overline{uw}$ all set to zero.

Averaging equation (3.1) over the periodic pattern of the SH surface micro-texture in the streamwise and spanwise directions, and integrating in the wall-normal direction gives

$$\nu\langle\frac{\partial\bar{U}}{\partial z}\rangle - \langle\overline{uw}\rangle - \langle\bar{U}\bar{W}\rangle = \langle u_\tau^2\rangle(1-\frac{z}{h}), \tag{3.2}$$

where $\langle\,\rangle$ denotes averaging in wall-parallel directions over the periodic pattern of the SH micro-texture, and $\langle u_\tau\rangle \equiv \sqrt{-\langle\partial\overline{P}/\partial x\rangle h/\rho}$ is the average wall-friction velocity in the SH channel.

Integration of equation (3.2) in the wall-normal direction, once from 0 to z, and again from 0 to h (*Fukagata et al.*, 2002), and use of the boundary condition $\langle\bar{U}\rangle|_{wall} = U_s$, gives

$$C_f = \frac{6}{Re_b}(1-\frac{U_s}{U_b}) + 3C_f\int_0^1\left[-\langle\overline{uw}\rangle^+ - \langle\bar{U}\bar{W}\rangle^+\right](1-\xi)\,d\xi, \tag{3.3}$$

where $C_f \equiv 2\langle u_\tau\rangle^2/U_b^2$ is the friction coefficient, $\xi = z/h$ is the normalized wall-normal coordinate, and the $+$ superscript denotes non-dimensionalization with respect to the average wall-friction velocity, $\langle u_\tau\rangle$, and kinematic viscosity, ν, in the SH channel. Equation (3.3) extends to SH channel flows the analytical formulation originally developed by *Fukagata et al.* (2002) for the breakdown of skin-friction drag into its constituting elements on smooth no-slip walls, which was later generalized to geometrically complex no-slip surfaces by *Peet and Sagaut* (2009). Here, the analysis is taken further to derive an exact analytical expression for the magnitude of DR in SH channel flow. To this end, equation (3.3) is rearranged as

$$C_f = \frac{6}{Re_b}\left(1-\frac{U_s}{U_b}\right)\left(\frac{1}{1-3I^+}\right), \tag{3.4}$$

where $I^+ = \int_0^1\left[-\langle\overline{uw}\rangle^+ - \langle\bar{U}\bar{W}\rangle^+\right](1-\xi)\,d\xi$, and I^+ is bounded by $0 < I^+ < 1/3$ per

(3.2). In channel flows with no-slip walls, equation (3.4) reduces to $C_f^0 = (6/Re_b)/(1-3I^{+0})$, where $I^{+0} = \int_0^1 [-\langle\overline{uw}\rangle^{+0}](1-\xi)d\xi$.

Defining the Drag Reduction (DR) as $DR \equiv (C_f^0 - C_f)/C_f^0$, an expression for the magnitude of DR in SH channel flow can then be obtained as

$$\begin{aligned} DR &= \frac{U_s}{U_b} + \left(1 - \frac{U_s}{U_b}\right)\left(\frac{3\varepsilon}{1-3I^+}\right) \\ &= \frac{U_s}{U_b} + O(\varepsilon), \end{aligned} \tag{3.5}$$

where $\varepsilon = I^{+0} - I^+$ is the difference between the values of the integrals in the base channel flow with no-slip walls and the SH channel flow.

Equation (3.5) gives an exact analytical expression for the magnitude of DR in laminar or turbulent SH channel flow, while providing a breakdown of the DR into: (i) contributions arising from the effective slip at the wall, captured in the U_s/U_b term, and (ii) contributions arising from modifications to the turbulence structure and dynamics and any additional secondary mean flows established in the SH channel, captured in the $O(\varepsilon)$ term. In laminar flow, where $I^{+0} = I^+ = \varepsilon = 0$, the magnitude of DR is given by $DR = U_s/U_b$, and DR is entirely due to the effective slip at the wall. In turbulent flow, the magnitude of DR is given by $DR = U_s/U_b + O(\varepsilon)$, where U_s/U_b represents the contribution of the effective slip on the wall to DR, while $\varepsilon = I^{+0} - I^+$ is a measure of the differences between the structure of turbulence in the SH channel and any secondary mean flows established in the SH channel compared to a base channel flow with no-slip walls. The relative importance of each of these terms in turbulent flow can be assessed using results from DNS.

3.2 DNS Studies

Roles of the effective slip on the walls versus modifications to the turbulence dynamics within the flow in the mechanism of DR by SH surfaces were quantified

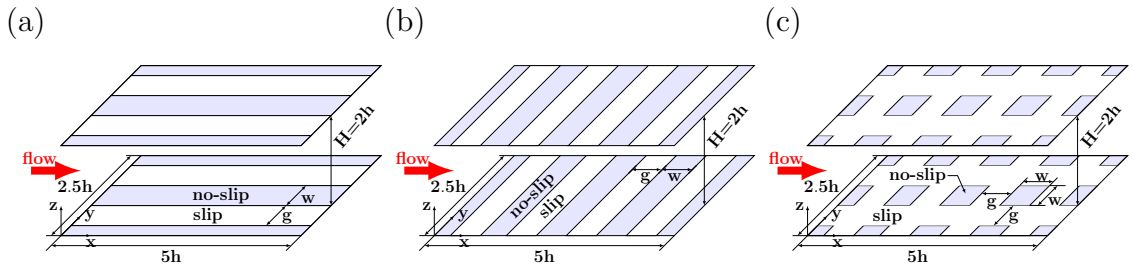

Figure 3.1: Schematic of the SH channels and the coordinate system: (a) longitudinal MG; (b) transverse MG; (c) micro-posts.

using data obtained with Lattice Boltzmann (LB) Direct Numerical Simulation (DNS) in laminar and turbulent SH channel flow with various patterns of longitudinal or transverse MG or micro-posts on both walls. In these DNS studies, the liquid/gas interfaces on the SH surfaces were modelled as 'idealized' flat, shear-free boundaries, similar to previous analytical (*Philip*, 1972a) and computational (*Martell et al.*, 2010; *Park et al.*, 2013; *Jelly et al.*, 2014; *Türk et al.*, 2014) studies.

The simulations were first performed in channels of size $5h \times 2.5h \times 2h$, in the streamwise (x), spanwise (y), and wall-normal (z) directions, respectively. A constant flow rate was maintained in the channel during the course of all simulations, corresponding to a bulk Reynolds number of $Re_b = 3600$. Grid spacings of $\Delta^{+0} \approx 2$ in all three directions was used for the simulations in turbulent flow. All the simulations were initialized from a fully developed base turbulent channel flow with no-slip walls at $Re_b = 3600$, corresponding to $Re_{\tau_0} \equiv u_{\tau_0} h/\nu \approx 223$.

A total of fifteen cases, with SH surface micro-patterns consisting of longitudinal MG, transverse MG, or micro-posts, g/w ratios of 1, 7, 15, and geometric parameters of $0.01 \leq (g+w)/2H \leq 0.29$, corresponding to $4 \lesssim g^{+0} \lesssim 128$, were studied, as shown in figure 3.1 and table 3.1. Here $H = 2h$ denotes the full-height of the channel, and the parameters (g/w) and $(g+w)/2H$ arise from analytical solutions in laminar SH channel flow with longitudinal or transverse MG (*Philip*, 1972a). For comparison, these fifteen cases were also studied by DNS in the laminar flow regime at $Re_b = 50$.

pattern	longitudinal MG												transverse MG						micro-posts		
Channel	$5h \times 2.5h \times 2h$												$20h \times 10h \times 2h$			$5h \times 2.5h \times 2h$			$5h \times 2.5h \times 2h$		
(g/w)	1	1	1	1	1	1	7	7	7	7	15	15	7	7	15	1	1	7	1	1	7
SFF	1/2	1/2	1/2	1/2	1/2	1/2	7/8	7/8	7/8	7/8	15/16	15/16	7/8	7/8	15/16	1/2	1/2	7/8	3/4	3/4	63/64
$(g+w)/2H$	0.01	0.02	0.04	0.07	0.14	0.29	0.04	0.04	0.07	0.07	0.14	0.14	0.04	0.07	0.14	0.02	0.07	0.07	0.02	0.07	0.07
$g^{+0}(turb)$	4	8	16	32	64	128	28	28	56	56	120	120	28	56	120	8	32	56	8	32	56
$w^{+0}(turb)$	4	8	16	32	64	128	4	4	8	8	8	8	4	8	8	8	32	8	8	32	8
GR	1	1	1	1	1	1	1	2	1	2	1	2	1	1	1	1	1	1	1	1	1
$DR\text{-}lam$	2%	3%	5%	9%	17%	28%	22%	-	33%	-	58%	-	-	-	-	3%	6%	24%	9%	18%	73%
$(U_s/U_b)_{lam}$	0.02	0.03	0.05	0.09	0.17	0.28	0.22	-	0.33	-	0.58	-	-	-	-	0.03	0.06	0.24	0.09	0.18	0.73
$DR\text{-}turb$	5%	11%	18%	23%	33%	47%	52%	49%	64%	61%	83%	81%	52%	64%	83%	-4%	2%	20%	14%	29%	81%
$(U_s/U_b)_{turb}$	0.05	0.1	0.15	0.23	0.32	0.37	0.43	0.44	0.55	0.56	0.72	0.75	0.43	0.54	0.72	0.04	0.07	0.25	0.15	0.31	0.67

Table 3.1: SH surface geometries, resulting slip velocities, and DRs in laminar & turbulent channel flow.

Furthermore, effects of the grid resolution and the channel size on the resulting normalized slip velocities, DRs, turbulent statistics and kinetic energy dynamics were also investigated using grid embedded LB DNS and LB DNS in large channels, respectively, as reported in table 3.1. These studies were focoused on SH surfaces with LMGs, due to their superior DR performance. Three cases with the highest DRs, corresponding to SH LMGs of size $g^{+0} \approx 28$ & $g/w = 7$, $g^{+0} \approx 56$ & $g/w = 7$, and $g^{+0} \approx 120$ & $g/w = 15$, wrere used for these studies. The simulations with grid-embedding were performed in channels of size $5h \times 2.5h \times 2h$, in the streamwise, spanwise, and wall-normal directions, respectively. Grid spacings of $\Delta_c^{+0} \approx 2$ and $\Delta_f^{+0} \approx 1$ in all three directions, on the coares grid and the fine grid, respectively, corresponding to a grid-embeding ratio of $GR = 2$, were used for these simulations. The fine grid in the simulations was extended up to $z \approx 1.5g$ away from the walls. Coarse grid covered the rest of the domain. Large channel simulations were performed in channels of size $20h \times 10h \times 2h$, in the streamwise, spanwise, and wall-normal directions, respectively. Grid spacings of $\Delta^{+0} \approx 2$ in all three directions was used for the large channel simulations. Both the grid-embedded, and the large channel simulations were performed by maintaining a constant flow rate in the channel during the coarse of the simulations, corresponding to a bulk Reynolds number of $Re_b = 3600$. Fully developed base turbulent channel flows with no-slip walls at $Re_b = 3600$, corresponding to $Re_{\tau_0} \equiv u_{\tau_0} h/\nu \approx 223$, were used for initializing all the simulations. The grid-embedded LB DNS was initialized using Distribution Function (DF)s obtained from LB DNS without grid embedding, in the base channel flow with no-slip walls, using the second order Lagrange interpolation in space. Large channel simulations were initialized using DFs obtained from LB DNS without grid-embedding in base channel flows with no-slip walls at the same domain size as the large channels. In all the cases, the resulting turbulent flow settled into a statistically steady state within a non-dimensional time of $tU_0/h \lesssim 100$. Figure 3.2 shows the time evolution of the

skin-friction coefficient in the simulations.

3.3 Results

Table 3.1 presents the slip velocities and DRs obtained in laminar and turbulent SH channel flow with LMGs, transverse MGs, and micro-posts of size g/w = 1, 7, 15. The largest slip velocities of $U_s/U_b = 0.72$, and the highest DRs of $DR = 83\%$, in turbulent flow, are obtained with SH LMGS of size $g^{+0} \approx 120$ & $g/w = 15$. The resulting slip velocities, and DRs, obtained in the small channels, are within 1% of those obtained in the large channels, suggesting that the channel size does not affect the results. In addtition, the resulting slip velocities and DRs, obtained with LB DNS without grid-embedding, are to within 7.7% of those obtained with grid-embedding, with a grid-embedding ratio of $GR = 2$, suggesting that grid independence has been achieved with the simulations.

3.3.1 The Magnitude of DR in Laminar and Turbulent SH Channel Flow

Figure 3.3(a) shows the DRs obtained in the present study in laminar and turbulent SH channel flow with LMGs, transverse MGs, and micro-posts of size g/w = 1, 7, 15, as a function of the geometric parameter $(g + w)/2H$. Also shown are the DNS data of *Park et al.* (2013), obtained in turbulent channel flow at $Re_{\tau_0} \approx 180$, 395, 590 with LMGs and $g/w \approx 1$, 3, 7, 16, and the DNS data of *Türk et al.* (2014) in turbulent channel flow at $Re_{\tau_0} \approx 180$ with LMGs and $g/w = 1$. The DNS of *Türk et al.* (2014) were performed under an imposed constant pressure gradient, for which *Türk et al.* (2014) report the increase in the bulk velocity in the presence of SH walls, compared to the base turbulent channel flow with no-slip walls, with an imposed constant pressure gradient. The DRs for the DNS of *Türk et al.* (2014) were estimated using the relation $DR = (C_f^0 - C_f)/C_f^0 = 1 - (U_{b_0}/U_b)^2$. However, it should be noted that this expression assumes a different Re_b in the SH channel compared to

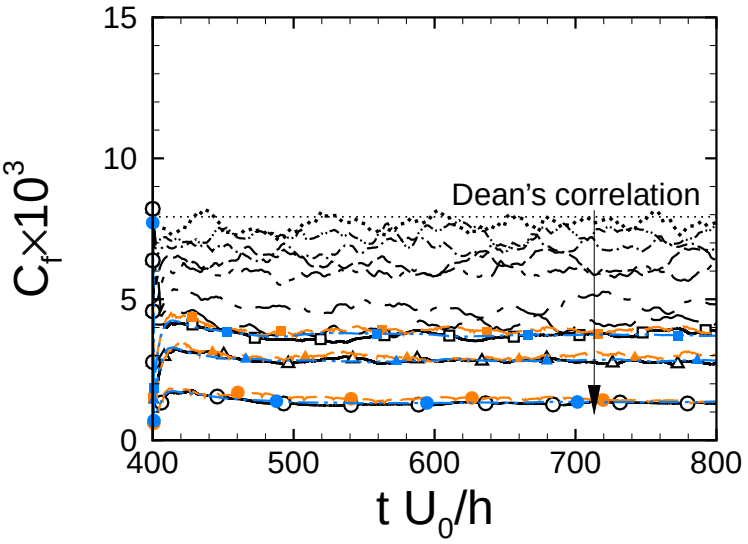

Figure 3.2: Time evolution of the skin-friction coefficient in turbulent channel flow with SH walls: $\cdots$, no-slip channel flow at $Re_{\tau_0} \approx 223$, without grid-embedding; $-\cdot\cdot-\cdot\cdot-$, $g^+ = w^+ \approx 4$, 5.0%DR, without grid-embedding; $-\cdot-\cdot-$, $g^+ = w^+ \approx 8$, 10.9%DR, without grid-embedding; ---, $g^+ = w^+ \approx 16$, 18.2%DR, without grid-embedding; ——$\cdot\cdot$——, $g^+ = w^+ \approx 32$, 22.6%DR, without grid-embedding; —$\cdot$—, $g^+ = w^+ \approx 64$, 38.2%DR, without grid-embedding; —— ——, $g^+ = w^+ \approx 128$, 47.3%DR, without grid-embedding; —□—, $g^+ \approx 28, w^+ \approx 4$, 51.6%$DR$, without grid-embedding; —△—, $g^+ \approx 56, w^+ \approx 8$, 63.5%$DR$, without grid-embedding; —○—, $g^+ \approx 120, w^+ \approx 8$, 83.2%$DR$, without grid-embedding; – –■– –, $g^+ \approx 28, w^+ \approx 4$, 49.2%$DR$, with grid-embedding, $GR = 2$; – –▲– –, $g^+ \approx 56, w^+ \approx 8$, 61.4%$DR$, with grid-embedding, $GR = 2$; – –●– –, $g^+ \approx 120, w^+ \approx 8$, 81.1%$DR$, with grid-embedding, $GR = 2$; – $\cdot\cdot$ –■– $\cdot\cdot$ –, $g^+ \approx 28, w^+ \approx 4$, 51.8%$DR$, large channel, without grid-embedding; – $\cdot\cdot$ –▲– $\cdot\cdot$ –, $g^+ \approx 56, w^+ \approx 8$, 63.7%$DR$, large channel, without grid-embedding; – $\cdot\cdot$ –●– $\cdot\cdot$ –, $g^+ \approx 120, w^+ \approx 8$, 82.8%$DR$, large channel, without grid-embedding; $\cdots$ (thin), Dean's correlation (*Dean*, 1978).

the base flow, and thus overestimates the magnitude of DR compared to the standard definition of DR, for which C_f and C_f^0 are evaluated at the same Re_b. For each category of SH surface micro-pattern, the DNS data show a trend for increase in DR with increasing $(g+w)/2H$ or g/w, at a given Re_{τ_0}. The DNS data of *Park et al.* (2013) also show a trend for increase in DR with increasing Re_{τ_0} for LMGs. For each category of SH surface micro-pattern, the DRs in laminar flow follow similar trends to those in turbulent flow. However, for a given SH surface micro-pattern, the magnitude of DR in turbulent flow is higher than that in laminar flow, by 143% to 267% with longitudinal MG, and by 10% to 61% with micro-posts, as shown in figure 3.3(a) and table 3.1. These trends are reversed with transverse MG, for which the DRs in turbulent flow are always lower than the corresponding cases in laminar flow, and in some cases even negative, indicating a Drag Increase (DI) in the presence of the SH surface. The significantly higher DRs observed in turbulent flow compared to laminar flow with LMGs has led a number of investigators (*Daniello et al.*, 2009; *Martell et al.*, 2010; *Rothstein*, 2010; *Park et al.*, 2013) to conclude that the enhanced DRs observed in turbulent flow must be due to mechanisms beyond the effective slip on the wall, such as modifications to the turbulence dynamics.

However, when the same DR data is plotted as a function of U_s/U_b, as shown in figure 3.3(b), the DRs from all DNS databases in laminar and turbulent flow, for all SH surface micro-patterns, nearly collapse and cluster around the line $DR = U_s/U_b$. In laminar flow, the magnitude of DR exactly matches U_s/U_b for all SH surface micro-patterns, as shown in table 3.1, confirming that DR in laminar flow is entirely due to the effective slip on the walls. In turbulent flow, the magnitude of DR either falls slightly above U_s/U_b, as with LMGs or micro-posts with high SFF, or slightly below U_s/U_b, as with transverse MGs or micro-posts with moderate SFF ratio. These reflect the effect of the $O(\varepsilon)$ term in equation (3.5), and indicate that changes to the structure and dynamics of turbulence within the flow can lead to either a further

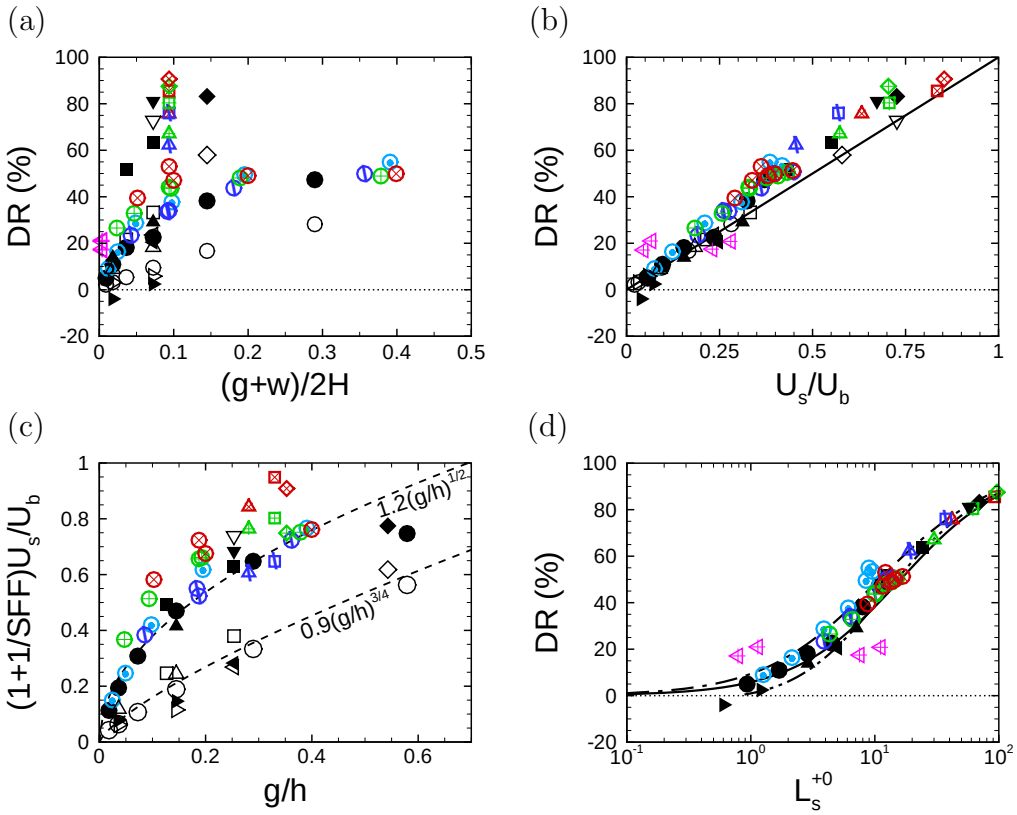

Figure 3.3: Scaling of DR and U_s/U_b in laminar and turbulent channel flow: (a) DR as a function of the geometric parameter $(g+w)/2H$ for different g/w and Re_{τ_0}; (b) DR as a function of the average slip velocity U_s/U_b; (c) average slip velocity on the slip surfaces, $(1+1/SFF)U_s/U_b$, as a function of g/h; (d) DR as a function of the slip length L_s^{+0}. ●, ■, ◆, present study, $Re_{\tau_0} \approx 223$, longitudinal MG, $g/w = 1$, 7, 15, respectively; ▶, ◀, present study, $Re_{\tau_0} \approx 223$, transverse MG, $g/w = 1$, 7, respectively; ▲, ▼, present study, $Re_{\tau_0} \approx 223$, micro-posts, $g/w = 1$, 7, respectively; ◯, □, ◇, present study, $Re_b = 50$, longitudinal MG, $g/w = 1$, 7, 15, respectively; ▷, ◁, present study, $Re_b = 50$, transverse MG, $g/w = 1$, 7, respectively; △, ▽, present study, $Re_b = 50$, micro-posts, $g/w = 1$, 7, respectively; ◯, △, □, DNS of *Park et al.* (2013), $Re_{\tau_0} \approx 180$, $g/w = 1$, 3, 7, respectively; ⊕, ⧋, ⊞, ◈, DNS of *Park et al.* (2013), $Re_{\tau_0} \approx 395$, $g/w = 1$, 3, 7, 15, respectively; ⊗, ⧊, ⊠, ◈, DNS of *Park et al.* (2013), $Re_{\tau_0} \approx 590$, $g/w = 1$, 3, 7, 15, respectively; ⊙, DNS of *Türk et al.* (2014), $Re_{\tau_0} = 180$, $g/w = 1$; ⧓, experiments of *Daniello et al.* (2009), $2450 \leq Re_b \leq 4000$, $g = w = 30\mu m$, MG on one wall; ——, $DR = U_s/U_b$ in (b), and $DR = L_s^{+0}/[1 + (Re_b/Re_{\tau_0})]$ with $Re_b = 3600$, $Re_{\tau_0} \approx 223$ in (d); –·–·–, –··–··–, analytical expressions of *Fukagata et al.* (2006) for uniform streamwise slip and uniform combined slip, respectively, at $Re_{\tau_0} \approx 223$.

DR or a DI beyond the DRs resulting from the effective slip on the walls. For the former, the modifications to the turbulence dynamics lead to a normalized Reynolds shear stress, $-\langle\overline{uw}\rangle^+$, in the SH channel which is lower than that in the base flow, thus making ε positive. For the latter, the modifications the modifications to the turbulence dynamics lead to a normalized Reynolds shear stress, $-\langle\overline{uw}\rangle^+$, in the SH channel which is slightly higher than that in the base flow, thus making ε negative. The SH surface micro-pattern in the latter case acts similar to surface roughness, enhancing the Reynolds shear stress. However, these additional DRs or DIs, resulting from modifications to the turbulence dynamics, are in all cases small and contribute no more than 10% to 15% additional DR with LMGs and micro-posts of high SFF, and no more than 10% DI with transverse MGs or micro-posts of moderate SFF. In all cases, 80% to 100% of the total DR arises from the effective slip on the walls.

The higher DRs observed in turbulent flow compared to laminar flow arise primarily from the higher normalized average slip velocities on the slip surfaces, $(1 + 1/SFF)U_s/U_b$, which can be achieved in turbulent flow compared to laminar flow with a given SH surface micro-pattern, as shown in figure 3.3(c), not from mechanisms beyond the effective slip on the wall. The only exceptions are transverse MGs and micro-posts with high SFF, for which the normalized average slip velocities in laminar and turbulent flow become comparable, either because the orientation of the MGs relative to flow direction makes the flow regime immaterial, as with transverse MGs, or because the nature of the flow is predominantly inviscid, as with micro-posts of high SFF.

Using the relations $U_s^+ = L_s^+$ and $U_s/U_b = L_s^{+0}(1 - DR)Re_{\tau_0}/Re_b$, equation (3.5) can be rearranged to give an expression for the magnitude of DR in terms of the slip length,

$$DR = \frac{L_s^{+0}}{L_s^{+0} + \frac{Re_b}{Re_{\tau_0}}} + O(\varepsilon). \tag{3.6}$$

Similar to equation (3.5), the scaling given by equation (3.6) remains valid in both

laminar and turbulent SH channel flow. However, unlike earlier similar expressions (*Fukagata et al.*, 2006), no assumptions about the shape of the mean velocity profile or the SH surface micro-pattern is required in the derivation of equation (3.6). Good agreement is seen in figure 3.3(d) between equation (3.6) and all available DNS data. Reasonable agreement is also seen in figures 3.3(b, d) between equations (3.5) and (3.6) and experimental data (*Daniello et al.*, 2009) for which the slip velocities were reported.

3.3.2 Turbulence Statistics

The roles of the effective slip on the wall and modifications to the turbulence dynamics within the flow in the mechanism of turbulent DR with SH surfaces can be further clarified by examining the one-point turbulence statistics and TKE budget in the SH channel. Due to their superior DR performance in turbulent flow, SH surfaces with Longitudinal Micro-Groove (LMG)s were used for these investigations.

The presence of SH LMGs on the channel walls gives rise to spanwise variations in all Reynolds-averaged quantities in turbulent flow, within a 'surface layer' of thickness $z \approx g$. Figure 3.4 shows such spanwise variations in the Reynolds-averaged streamwise velocity. Similar spanwise variations exist in all the Reynolds-averaged turbulence statistics, including the Reynolds stresses. The latter gives rise to the development of a secondary mean flow, in the form of pairs of counter-rotating vortices (*Rastegari and Akhavan*, 2013; *Jelly et al.*, 2014; *Türk et al.*, 2014), within the 'surface layer' of size $z \lesssim g$, as shown in figure 3.5. Presence of these vortices is also predicted by the equation for the mean streamwise vorticity, $\bar{\Omega}_x$, in turbulent channel flow (*Perkins*, 1970),

$$\bar{V}\frac{\partial\bar{\Omega}_x}{\partial y} + \bar{W}\frac{\partial\bar{\Omega}_x}{\partial z} = \left(\frac{\partial^2}{\partial y^2} - \frac{\partial^2}{\partial z^2}\right)(-\overline{vw}) + \frac{\partial^2}{\partial y \partial z}\left(\overline{v^2} - \overline{w^2}\right) + \frac{1}{Re_b}\nabla^2\bar{\Omega}_x, \qquad (3.7)$$

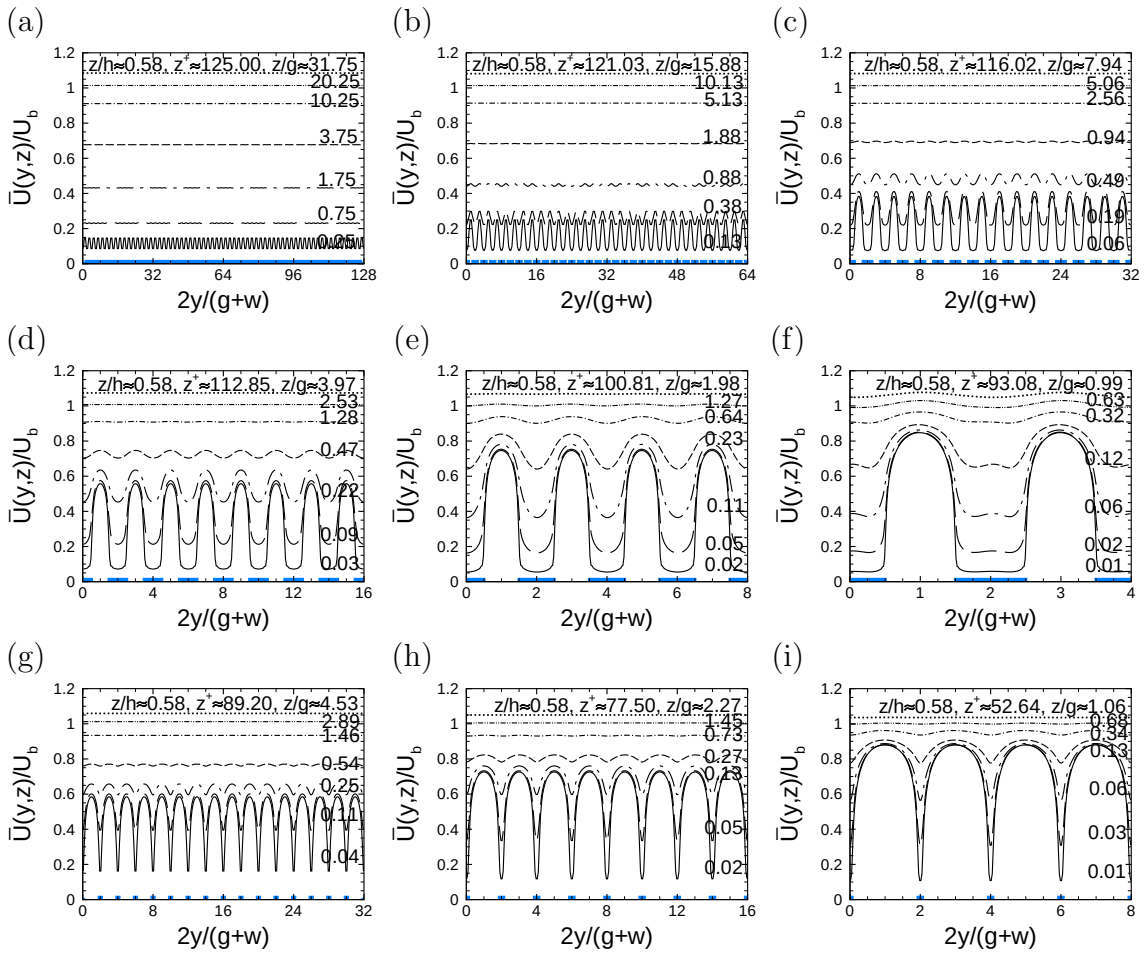

Figure 3.4: Spanwise variation of the mean streamwise velocity in turbulent channel flow with SH walls: (a) $g^{+0} = w^{+0} \approx 4$, $5.0\%DR$; (b) $g^{+0} = w^{+0} \approx 8$, $10.9\%DR$; (c) $g^{+0} = w^{+0} \approx 16$, $18.2\%DR$; (d) $g^{+0} = w^{+0} \approx 32$, $22.6\%DR$; (e) $g^{+0} = w^{+0} \approx 64$, $38.2\%DR$; (f) $g^{+0} = w^{+0} \approx 128$, $47.3\%DR$; (g) $g^{+0} \approx 28, w^{+0} \approx 4$, $51.9\%DR$; (h) $g^{+0} \approx 56, w^{+0} \approx 8$, $63.5\%DR$; (i) $g^{+0} \approx 120, w^{+0} \approx 8$, $83.2\%DR$; ——, $z/h \approx 0.01$; —— ——, $z/h \approx 0.01$; —·—, $z/h \approx 0.03$; - - -, $z/h \approx 0.07$; –·–·–, $z/h \approx 0.19$; –··–··–, $z/h \approx 0.37$; · · ·, $z/h \approx 0.58$; blue lines indicate location of no-slip surfaces.

in which the first two terms on the right hand side represent production of $\bar{\Omega}_x$ by turbulent stresses. For turbulent channel flow with SH LMGs on the walls, $\overline{vw} = 0$, as is evident from the DNS results, and thus the $\bar{\Omega}_x$ production by the first term is negligible. However, the spanwise variations in the turbulent stresses, $\overline{v^2}$ and $\overline{w^2}$, lead to the production of mean streamwise vorticity in the flow, through the second term on the right hand side of equation (3.7).

Both this secondary mean flow and the spanwise variations in the Reynolds-averaged turbulence statistics need to be properly accounted for to obtain accurate turbulence statistics in the SH channel. To facilitate comparison of these statistics to those in turbulent channel flows with no-slip walls, all Reynolds-averaged statistics in the SH channel are reported here after performing an additional spanwise average, $\langle\,\rangle$, over the pattern of slip and no-slip surfaces on the SH walls.

Figures 3.6(a-c) show the normalized profiles of the spanwise-averaged mean streamwise velocity, $\langle\bar{U}\rangle^+$, turbulence intensities, $\{\langle\bar{u_i^2}\rangle^+\}^{1/2}$, and shear stresses, $\langle\tau_{xz}\rangle^+$, in the SH channel, compared to a base channel flow with no-slip walls, where the superscript + denotes non-dimensionalization with respect to the wall-friction velocity, u_τ and kinematic viscosity, ν, of the corresponding flow. The mean velocity profiles display increasing slip velocity with increasing DR, as shown in figure 3.6(a) and table 3.1. The resulting mean velocities profiles are offset from those obtained in large channels, by 1%, and from those obtained with grid-embedding, by up to 7%, concomitant with the differences in the magnitude of the slip velocities on the SH wall, as seen in figure 3.6(a) and table 3.1. With the average slip velocity subtracted, the mean streamwise velocity profiles, $\langle\bar{U}\rangle^+ - U_s^+$, in the SH channel display a progressive thinning of the buffer layer, along with a downward shift of the logarithmic layer, with increasing DR. These features are in stark contrast to other examples of drag reduced turbulent flow, for which DR is generally accompanied by a thickening of the buffer layer and an upward shift of the logarithmic layer (*Bushnell and Hefner*, 1990). The

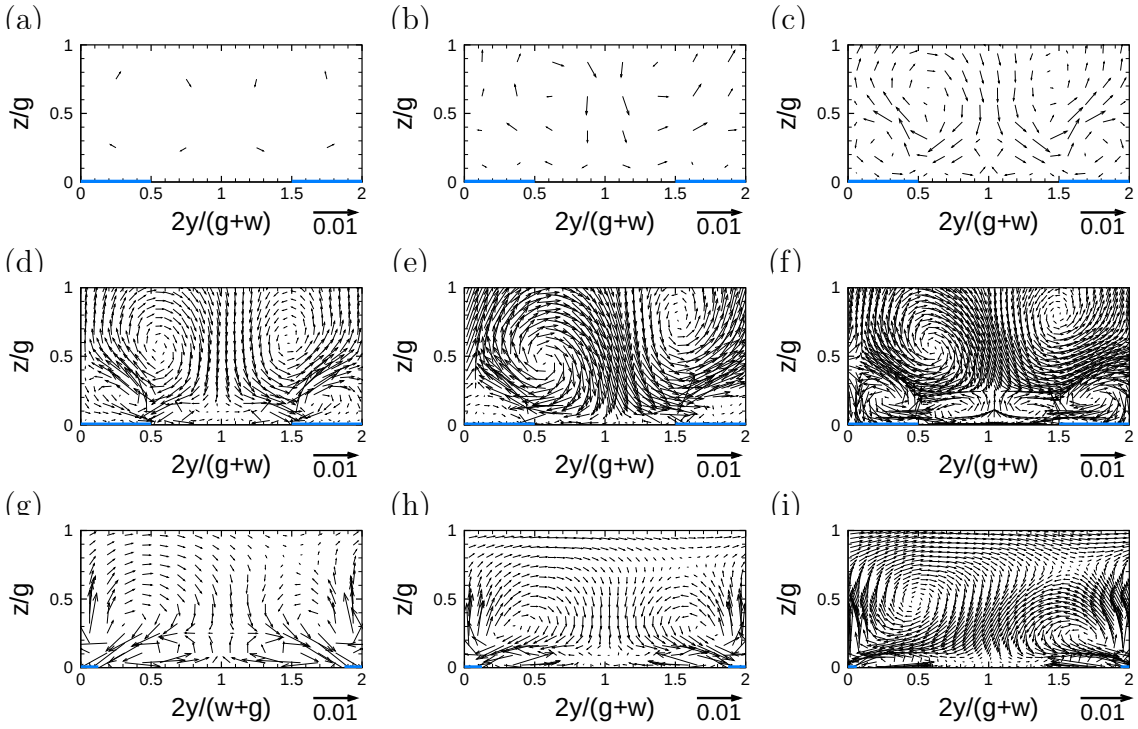

Figure 3.5: Vector plots of the secondary mean flow in turbulent channel flow with SH walls, (a) $g^{+0} = w^{+0} \approx 4$, 5.0%$DR$; (b) $g^{+0} = w^{+0} \approx 8$, 10.9%$DR$; (c) $g^{+0} = w^{+0} \approx 16$, 18.2%$DR$; (d) $g^{+0} = w^{+0} \approx 32$, 22.6%$DR$; (e) $g^{+0} = w^{+0} \approx 64$, 38.2%$DR$; (f) $g^{+0} = w^{+0} \approx 128$, 47.3%$DR$; (g) $g^{+0} \approx 28, w^{+0} \approx 4$, 51.9%$DR$; (h) $g^{+0} \approx 56, w^{+0} \approx 8$, 63.5%$DR$; (i) $g^{+0} \approx 120, w^{+0} \approx 8$, 83.2%$DR$; blue lines indicate location of no-slip surfaces.

difference lies in the mechanism of DR in the present flow, which is primarily the effective slip on the walls. The presence of this effective slip leads to weaker gradients of the mean streamwise velocity over the slip surfaces up to distances of $z \approx g$, as shown in figure 3.4, which when mixed and averaged with the mean streamwise velocities over the no-slip surfaces, leads to weaker gradients in $\langle \bar{U} \rangle^+$ within the 'surface-layer', and manifests as a progressive thinning of the buffer layer and a downward shift of the logarithmic layer in the profiles of $\langle \bar{U} \rangle^+ - U_s^+$.

Figure 3.6(c) shows the normalized profiles of the spanwise-averaged Reynolds shear stress, $\langle \tau_{R,xz} \rangle^+ \equiv -\langle \overline{uw} \rangle^+$, viscous shear stress, $\langle \tau_{v,xz} \rangle^+ \equiv \langle \partial \overline{U} / \partial y \rangle^+$, mean convective stress, $\langle \tau_{c,xz} \rangle^+ \equiv -\langle \bar{U}\bar{W} \rangle^+$, and total stress, $\langle \tau_t \rangle^+ \equiv \langle \tau_{R,xz} \rangle^+ + \langle \tau_{v,xz} \rangle^+ + \langle \tau_{c,xz} \rangle^+$, in the SH channel, compared to the base flow. The normalized profiles of the Reynolds shear stress display a progressive drop in their peak magnitudes compared to the base flow, with increasing DR. However, the magnitudes of these drops are nowhere as large as those observed at comparable DR with other means of skin-friction DR. Indeed, the profiles of normalized Reynolds shear stress remain comparable to those which would be observed in a turbulent channel flow with no-slip walls at the Re_τ of the drag reduced SH channel flow, as shown in figure 3.6(c). This keeps the differences between the Reynolds shear stress in the SH flow and that in the base flow small, thus keeping the $O(\varepsilon)$ term in equation (3.5) small. The normalized profiles of the viscous shear stress, $\langle \tau_{v,xz} \rangle^+$, reflect the changes in the slope of the mean velocity profiles observed in figure 3.6(b). In computing the total balance of shear stresses, in addition to the Reynolds and viscous shear stresses, a small contribution is also observed from the mean convective stress, $-\langle \bar{U}\bar{W} \rangle^+$, arising from the secondary mean flow in the channel. With this contribution, the total stress shows good agreement with the theoretical line $\langle \tau_t \rangle^+ = (1 - z/h)$, as required by equation (3.2). These secondary flows are found to make a negligible contribution to the $O(\varepsilon)$ term in equation (3.5). It should be noted that all the profiles in figure 3.6(c)

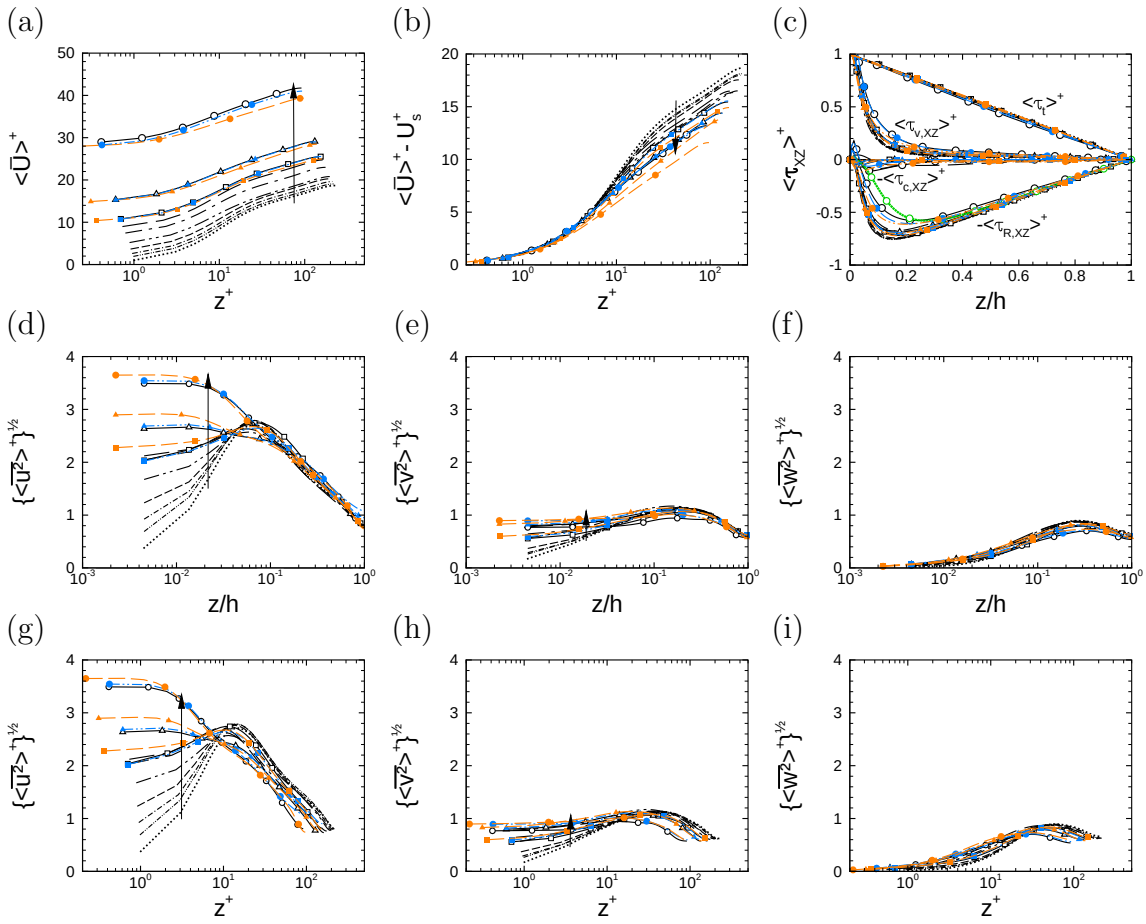

Figure 3.6: Spanwise-averaged turbulence statistics in channel flow with SH walls: (a) mean streamwise velocity; (b) mean streamwise velocity with the slip velocity subtracted; (c) Reynolds shear stress $\langle\tau_{R,xz}\rangle^+ = -\langle\overline{uw}\rangle^+$, viscous shear stress $\langle\tau_{v,xz}\rangle^+ = \langle\partial\bar{U}/\partial z\rangle^+$, convective stress $\langle\tau_c\rangle^+ = -\langle\bar{U}\bar{W}\rangle^+$, and total shear stress $\langle\tau_t\rangle^+ = \langle\tau_{R,xz}\rangle^+ + \langle\tau_{v,xz}\rangle^+ + \langle\tau_c\rangle^+$; (d,e,f) streamwise, $\langle\overline{u^2}\rangle^{1/2+}$, spanwise, $\langle\overline{v^2}\rangle^{1/2+}$, and wall-normal, $\langle\overline{w^2}\rangle^{1/2+}$, turbulence intensities; (g,h,i) streamwise, spanwise and wall-normal turbulence intensities; $\cdots$, no-slip channel flow at $Re_{\tau_0} \approx 223$, without grid-embedding; $-\cdot\cdot-\cdot\cdot-$, $g^+ = w^+ \approx 4$, $5.0\%DR$, without grid-embedding; $-\cdot-\cdot-$, $g^+ = w^+ \approx 8$, $10.9\%DR$, without grid-embedding; - - -, $g^+ = w^+ \approx 16$, $18.2\%DR$, without grid-embedding; ——$\cdot\cdot$——, $g^+ = w^+ \approx 32$, $22.6\%DR$, without grid-embedding; —$\cdot$—, $g^+ = w^+ \approx 64$, $38.2\%DR$, without grid-embedding; —— ——, $g^+ = w^+ \approx 128$, $47.3\%DR$, without grid-embedding; —□—, $g^+ \approx 28, w^+ \approx 4$, $51.6\%DR$, without grid-embedding; —△—, $g^+ \approx 56, w^+ \approx 8$, $63.5\%DR$, without grid-embedding; —○—, $g^+ \approx 120, w^+ \approx 8$, $83.2\%DR$, without grid-embedding; – –■– –, $g^+ \approx 28, w^+ \approx 4$, $49.2\%DR$, with grid-embedding, $GR = 2$; – –▲– –, $g^+ \approx 56, w^+ \approx 8$, $61.4\%DR$, with grid-embedding, $GR = 2$; – –●– –, $g^+ \approx 120, w^+ \approx 8$, $81.1\%DR$, with grid-embedding, $GR = 2$; $-\cdot\cdot-$■$-\cdot\cdot-$, $g^+ \approx 28, w^+ \approx 4$, $51.8\%DR$, large channel, without grid-embedding; $-\cdot\cdot-$▲$-\cdot\cdot-$, $g^+ \approx 56, w^+ \approx 8$, $63.7\%DR$, large channel, without grid-embedding; $-\cdot\cdot-$●$-\cdot\cdot-$, $g^+ \approx 120, w^+ \approx 8$, $82.8\%DR$, large channel, without grid-embedding; $\cdots$ (green), no slip channel flow at $Re_{\tau_0} \approx 100$, without grid-embedding.

fall within 1% of those obtained in the large channels, suggesting that the channel size has not affected on the results. Furthermore, LB DNS results obtained without grid embedding show differences of up to 10% with those obtained with grid-embedded LB DNS, with $GR = 2$, due to the low resolution in the near-wall region. Beyond $z/h \approx 0.2$, however, the differences are negligible, as seen in figure 3.6(c), and all the profiles collapse.

Figures 3.6(d-i) show the normalized profiles of the spanwise-averaged turbulence intensities in the SH channel compared to the base flow. Within a 'surface layer' of size $z \lesssim g$, the normalized streamwise, spanwise, and to a lesser extent wall-normal turbulence intensities are enhanced compared to the base flow, as shown in figures 3.6(d-i). Outside of the 'surface layer', the normalized profiles of the turbulence intensities approach those in the base flow, save for differences which can be attributed to the lower Re_τ of the drag reduced flow compared to the base flow, as is suggested by comparing the figures 3.6(d-f) with figures 3.6(g-i). It will be shown in section § 3.3.3 that the enhanced production of turbulence intensities within the 'surface layer' arises from the spanwise gradients of the mean streamwise velocity, $\partial\overline{U}/\partial y$, at the boundary between the slip and no-slip stripes (see figure 3.4). This enhanced production occurs in the streamwise component of the turbulence kinetic energy, $\langle\overline{u^2}\rangle$, and is transferred to the other components through the pressure-strain transport term. Furthermore, the normalized profiles of the spanwise-averaged turbulence intensities all fall within 1% of those obtained in large channels, suggesting that the channel size has no effect on the results. In addition, near the walls, within a region of $z^+ \lesssim 5$, the normalized profiles of the spanwise-averaged turbulence intensities obtained with LB DNS without grid-embedding show a difference of up to 10% with those obtained with grid-embedding, with $GR = 2$, due to the low resolution in this region, as seen in figures 3.6(g-i). Outside this region, however, for $z^+ \gtrsim 5$, all the differences disappear, as seen in figures 3.6(g-i), suggesting that the effect of grid resolution is limited to

the near-wall region.

Furthermore, the presence of spanwise gradients in the mean streamwise velocity, $\partial\bar{U}/\partial y$ (see figure 3.4), gives rise to an additional Reynolds shear stress, $\tau^+_{R,xy} = -\overline{uv}^+$, in the SH channel, as shown in figure 3.7. This Reynolds shear stress is anti-symmetric over the spanwise extent of the slip or no-slip stripes, and thus leads to a zero stress when averaged over the periodic pattern of the SH surface, $\langle\tau_{R,xy}\rangle^+ = 0$. However, as will be shown in more details in § 3.3.3, it leads to an additional turbulence production term, $-\langle\overline{uv}\partial\bar{U}/\partial y\rangle^+$. It is this term which gives rise to enhanced production of turbulence at distances of $z \lesssim g$ in figure 3.6.

3.3.3 Turbulence Kinetic Energy Dynamics

The features described in the previous section are also borne out in the dynamics of turbulence kinetic energy (TKE). In stationary turbulence, the TKE dynamics in the α direction is governed by (*Hinze*, 1975)

$$\frac{D}{Dt}\frac{\overline{u_\alpha u_\alpha}}{2} = P_{\alpha\alpha} - \varepsilon_{\alpha\alpha} + t^{(\Sigma)}_{\alpha\alpha} + \Pi_{\alpha\alpha}, \tag{3.8}$$

where,

$$\begin{aligned}
P_{\alpha\alpha} &= -\overline{u_\alpha u_\gamma}\frac{\partial\bar{U}_\alpha}{\partial x_\gamma},\\
\varepsilon_{\alpha\alpha} &= 2\nu\overline{s_{\alpha\gamma}\frac{\partial u_\alpha}{\partial x_\gamma}},\\
t^{(\Sigma)}_{\alpha\alpha} &= t^{(R)}_{\alpha\alpha} + t^{(press)}_{\alpha\alpha} + t^{(v)}_{\alpha\alpha}\\
&= -\frac{1}{2}\frac{\partial}{\partial x_\gamma}\overline{u_\alpha u_\alpha u_\gamma} - \frac{1}{\rho}\frac{\partial}{\partial x_\alpha}\overline{pu_\alpha} + 2\nu\frac{\partial}{\partial x_\gamma}\overline{u_\alpha s_{\alpha\gamma}},\\
\Pi_{\alpha\alpha} &= \frac{1}{\rho}\overline{p\frac{\partial u_\alpha}{\partial x_\alpha}}.
\end{aligned}$$

Here, $P_{\alpha\alpha}$ is the rate of TKE production per unit mass, $\varepsilon_{\alpha\alpha}$ is the rate of viscous dissipation, $t^{(R)}_{\alpha\alpha}$, $t^{(press)}_{\alpha\alpha}$, and $t^{(v)}_{\alpha\alpha}$ are the rates of TKE transport by turbu-

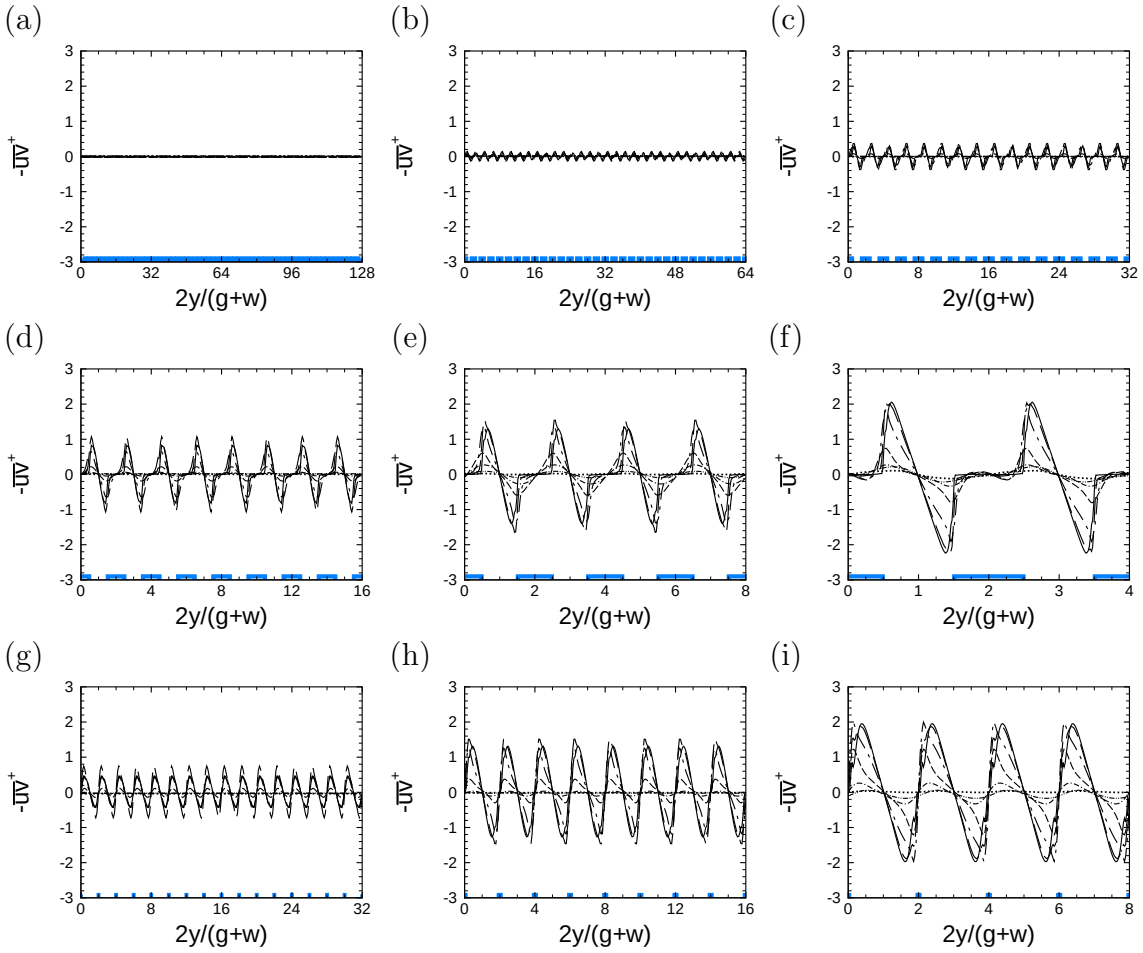

Figure 3.7: Spanwise variation of the Reynolds stress, $\tau^+_{R,xy} = -\overline{uv}$, in turbulent channel flow with SH walls: (a) $g^{+0} = w^{+0} \approx 4$, 5.0%$DR$; (b) $g^{+0} = w^{+0} \approx 8$, 10.9%$DR$; (c) $g^{+0} = w^{+0} \approx 16$, 18.2%$DR$; (d) $g^{+0} = w^{+0} \approx 32$, 22.6%$DR$; (e) $g^{+0} = w^{+0} \approx 64$, 38.2%$DR$; (f) $g^{+0} = w^{+0} \approx 128$, 47.3%$DR$; (g) $g^{+0} \approx 28, w^{+0} \approx 4$, 51.9%$DR$; (h) $g^{+0} \approx 56, w^{+0} \approx 8$, 63.5%$DR$; (i) $g^{+0} \approx 120, w^{+0} \approx 8$, 83.2%$DR$; line types as in figure 3.4.

lent fluctuations, pressure fluctuations and viscous stresses, respectively, which constitute the total transport, $t^{(\Sigma)}_{\alpha\alpha}$. Also, $\Pi_{\alpha\alpha}$ is the pressure-strain correlation, and $s_{\alpha\gamma} = 1/2(\partial u_\alpha/\partial x_\gamma + \partial u_\gamma/\partial x_\alpha)$ is the fluctuating strain-rate tensor. No summation is implied over the index α.

Summation of equation (3.8) over all α directions gives the TKE balance as (*Hinze*, 1975)

$$\frac{D}{Dt}\overline{k^2} = P_{ii} - \varepsilon_{ii} + t^{(\Sigma)}_{ii}, \tag{3.9}$$

where $\overline{k^2} = \overline{u_i^2}/2$ is the turbulence kinetic energy per units mass, and the pressure-strain term is eliminated because $\Pi_{ii} = 0$.

Figures 3.8 and 3.9 show the spanwise-averaged balance of Turbulence Kinetic Energy (TKE) and its components in the SH channel, respectively. When normalized with the bulk variables, h and U_b, the production, dissipation, and transport of TKE in the SH channel display significant drops compared to the base flow, as shown in figures 3.8(a-c), consistent with the presence of DR and the lower Re_τ in the SH channel. When normalized in wall units, however, the profiles of TKE production, $\langle P\rangle^+$, and dissipation, $\langle\varepsilon\rangle^+$, collapse to those in the base flow outside of the 'surface layer' ($z \gtrsim g$), while within the 'surface layer' ($z \lesssim g$), there is additional production and dissipation of TKE compared to the base flow, as shown in figure 3.8(d). Similar to that in regular turbulent channel flows, here, production of turbulence only occurs in the streamwise component. However, in addition to the usual production of streamwise TKE due to the gradients of the mean streamwise velocity in the wall-normal direction, $-\langle\overline{uw}\partial\bar{U}/\partial z\rangle$, there is now additional production of streamwise TKE due to gradients of the mean streamwise velocity in the spanwise direction, $-\langle\overline{uv}\partial\bar{U}/\partial y\rangle$, as shown in figures 3.8(e). The normalized production through $-\langle\overline{uw}\partial\bar{U}/\partial z\rangle$ is little changed from that in the base flow at low DR, but displays a small drop from the base flow values throughout the cross-section of the channel at high DR, as shown in figure 3.8(e). The production due to $-\langle\overline{uv}\partial\bar{U}/\partial y\rangle$ occurs inside the 'surface layer', within

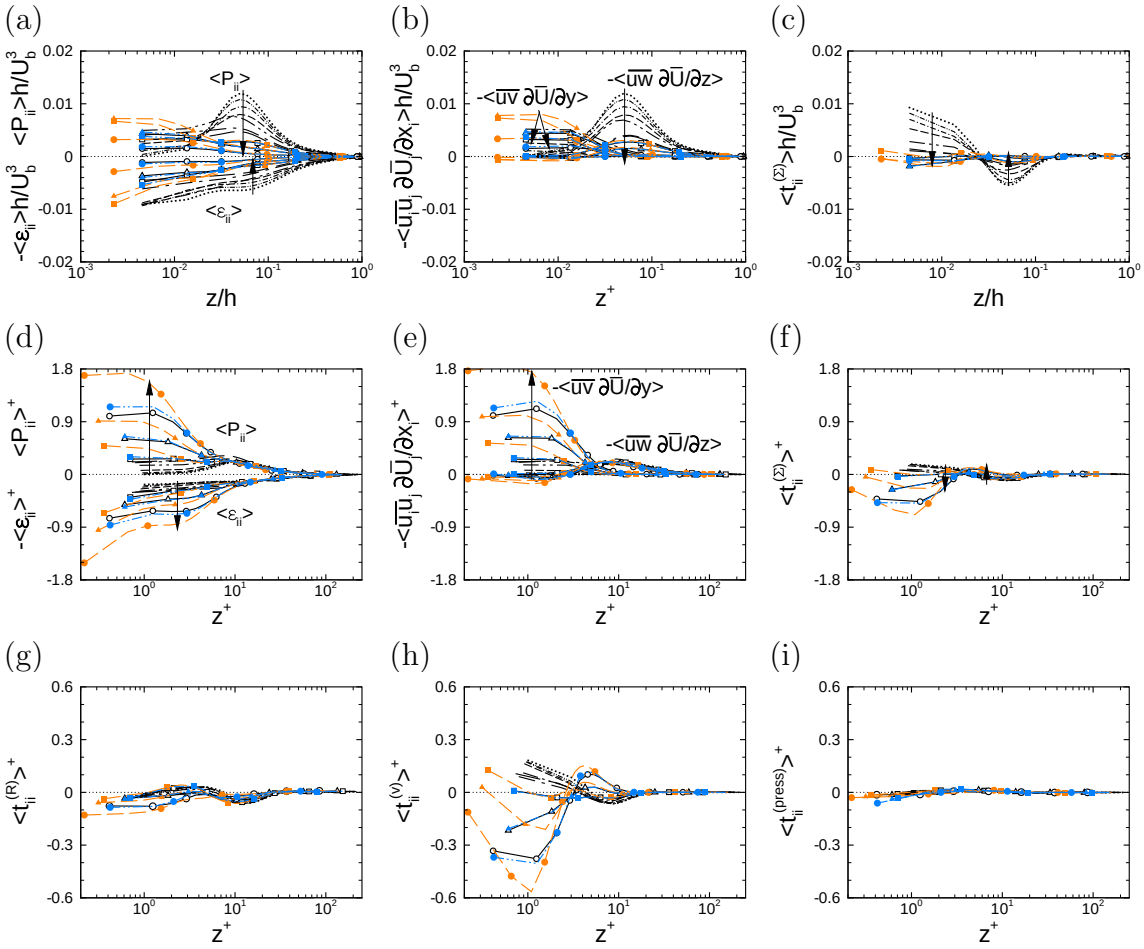

Figure 3.8: Spanwise-averaged turbulence kinetic energy budget in channel flow with SH walls: (a) production $\langle P_{ii} \rangle^+$ and dissipation, $\langle \varepsilon \rangle^+$; (b,c) breakdown of the production term; (d) transport by the fluctuating Reynolds stress, $\langle t_{ii}^{(R)} \rangle^+$; (e) transport by the fluctuating viscous stress, $\langle t_{ii}^{(v)} \rangle^+$; (f) transport by the fluctuating pressure, $\langle t_{ii}^{(press)} \rangle^+$; (g) total transport, $\langle t_{ii}^{(\Sigma)} \rangle^+$; line types as in figure 3.6.

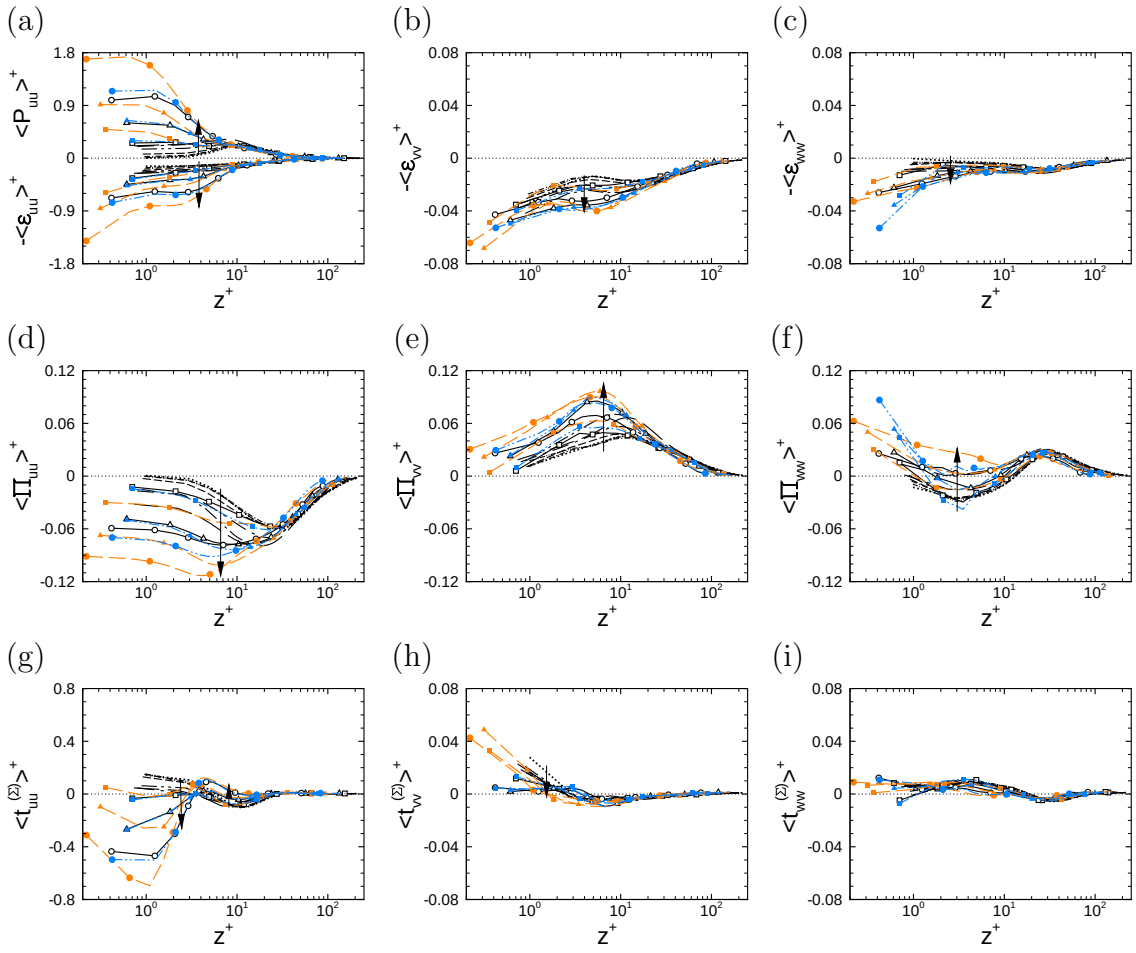

Figure 3.9: Spanwise-averaged budgets of streamwise, spanwise and wall normal turbulence kinetic energy in channel flow with SH walls: (a,b,c) turbulence production, $\langle P_{\alpha\alpha}\rangle^+$, dissipation, $\langle \epsilon_{\alpha\alpha}\rangle^+$, and total transport, $\langle t^{(\Sigma)}_{\alpha\alpha}\rangle^+ = \langle t^{(v)}_{\alpha\alpha} + t^{(press)}_{\alpha\alpha} + t^{(R)}_{\alpha\alpha}\rangle^+$; (d,e,f) pressure strain correlation, $\langle \Pi_{\alpha\alpha}\rangle^+$; (g,h,i) sum of transport terms, $\langle t^{(\Sigma)}_{\alpha\alpha}\rangle^+ = \langle t^{(v)}_{\alpha\alpha} + t^{(press)}_{\alpha\alpha} + t^{(R)}_{\alpha\alpha}\rangle^+$; line types as in figure 3.6.

$z \lesssim g$ from the walls, as shown in figure 3.8(e). This is where there are spanwise gradients in the mean streamwise velocity, mainly over the SH LMGs (see figure 3.4). This additional production due to $-\langle\overline{uv}\partial\bar{U}/\partial y\rangle$, however, is not drag reducing, but gives rise to enhanced streamwise turbulence intensities, $\langle\overline{uu}\rangle$, which is further transferred to the spanwise $\langle\overline{vv}\rangle$ and wall-normal $\langle\overline{ww}\rangle$ components through the pressure-strain correlation, as shown in figures 3.9(d-f). This leads to enhanced $\Pi^+_{\alpha\alpha}$ terms at $z \lesssim g$ as seen in figures 3.9(d-f), and the trends in the turbulence intensities observed at $z \lesssim g$ in figures 3.6(d-i).

These results all show that the effect of the SH surface on the dynamics of turbulence remains confined to a thin 'surface layer' near the walls, within the region $z \lesssim g$, where there is additional production of TKE, by $-\langle\overline{uv}\partial\bar{U}/\partial y\rangle$, over the SH LMGs. This enhanced TKE production is balanced locally by viscous dissipation within the 'surface layer', in low DR regime, as shown in figure 3.8(f). In the high DR regime, the additional production of TKE within the 'surface layer' cannot be fully dissipated locally, thus it is transported to the interior of the flow, mainly though the viscous transport mechanisms, as seen in figure 3.8(h), where it is dissipated. This leads to a reversal in the sign of the transport terms within the 'surface layer', compared to the base flow, as shown in figures 3.8(f,h). The main effect of the SH surface on the dynamics of turbulence is thus additional production of TKE within a 'surface layer' of thickness on the order of the width of the SH MG. This effect, however, is not drag reducing, but turbulence enhancing. Outside of this 'surface layer', the normalized dynamics of turbulence in the SH channel proceeds as in channel flows with no-slip walls at the Re_τ of the SH channel flow. Collectively, these results indicate that the effect of the SH surface on the internal dynamics of turbulence is small, and the dominant mechanism of turbulent DR with SH surfaces remains the effective slip on the wall.

It should be noted that, due to the strongly inhomogeneous nature of this flow, the

commonly used 'isotropic' definitions of the viscous dissipation, $\varepsilon_{ii} = \nu\overline{(\partial u_i/\partial x_j)^2}$, and the viscous transport, $t_{ii}^{(v)} = \nu\partial^2\overline{k^2}/\partial x_j^2$, differ from the correct thermodynamic definitions, and the correct definitions have to be used for the comparisons (*Corrsin*, 1953).

3.3.4 Vortex Structures

Features similar to those that appeared in the turbulence statistics and TKE budget, are also observed in the vorticity field over the Super-Hydrophobic (SH) surface. Figure 3.10 displays the normalized profiles of the spanwise averaged root-mean-square (rms) vorticity fluctuations in the SH channel, compared to a base channel flow with no-slip walls. Within the 'surface layer' of size $z \lesssim g$ near the SH walls, there is enhanced vorticity fluctuations in all directions, as seen in figures 3.10(a-c). Outside of the 'surface layer', however, the normalized profiles of the spanwise-averaged vorticity fluctuations revert back to those of the no-slip wall, once again suggesting that effect of the SH surface on the dynamics of turbulence remains confined to a narrow region near the wall. Furthermore, LB DNS results fall within 1% of those obtained in the large channel, suggesting that the channel size has not had any effect on the results. In addition, LB DNS results with grid embedding, with $GR = 2$, remain within 10% of those obtained without grid-embedded. These differences, however, all are limited to a region of width $z^+ \lesssim 5$ near the SH walls. Beyond $z^+ \approx 5$, there is no difference between the LB DNS results obtained without grid-embedding and those obtained with grid-embedding, suggesting that the grid resolution has only affected the results within $z^+ \lesssim 5$.

Within the 'surface layer', with $z \lesssim g$, figure 3.10(a) shows that with increasing the width of the SH LMGs, the local maximum of the normalized profile of the streamwise vorticity fluctuations moves towards the wall, while its minimum disappears. On a flat no-slip wall, the normalized profile of the streamwise vorticity fluctuations, in

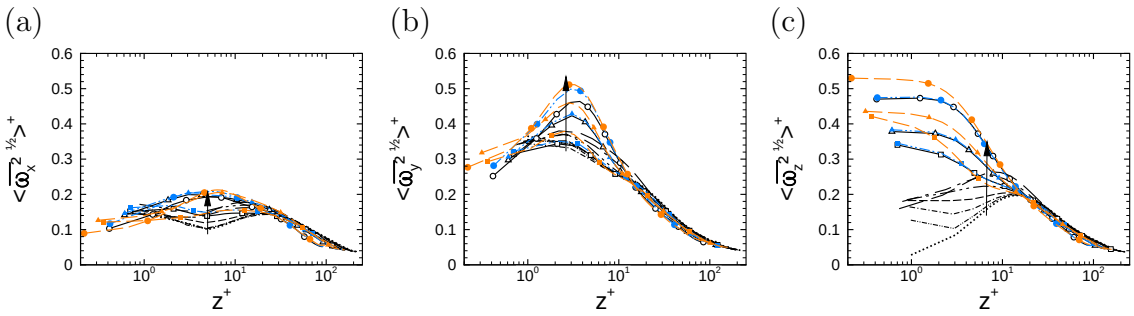

Figure 3.10: Spanwise-averaged root mean square (rms) vorticity fluctiations in channel flow with SH walls: (a) streamwise component, $\langle\overline{\omega_x^2}\rangle^{1/2+}$; (b) spanwise component, $\langle\overline{\omega_y^2}\rangle^{1/2+}$; (c) wall-normal component, $\langle\overline{\omega_z^2}\rangle^{1/2+}$; line types as in figure 3.6.

wall units, contains a local maximum, at $z^+ \approx 20$, and a local minimum, at $z^+ \approx 5$ (*Kim et al.*, 1987). It has been suggested that the location of its local maximum corresponds to the average location of the centers of the streamwise vortices near the wall (*Kim et al.*, 1987). These near-wall streamwise vortices, induce streamwise vorticity of the opposite sign on the wall, due to the no-slip condition (*Kim et al.*, 1987). Since the streamwise vorticity must become zero somewhere between the center of the vortex and the wall, *Kim et al.* (1987) have suggested that the local minimum of the normalized profile of the streamwise vorticity fluctuations, in wall units, corresponds to the average location of the edge of the vortices. The average radius of the streamwise vortices, in wall units, corresponds to the difference between the locations of these extrema (*Kim et al.*, 1987). On a slip surface, however, the streamwise vortices do not induce streamwise vorticity of the opposite sign. As a result, they would stay closer to the wall. In agreement with *Kim et al.* (1987)'s interpretation of the extrema of the normalized streamwise vorticity fluctuations, figure 3.10(a) shows that with increasing the width of the SH LMGs, the local maximum of the streamwise vorticity fluctuations moves towards the wall, while its minimum disappears.

Furthermore, within the 'surface layer', with $z \lesssim g$, increasing the width of the SH LMGs leads to an increase in the normalized magnitudes of the spanwise vorticity

fluctuations, as shown in figure 3.10(b). Similar behavior is also observed with the normalized magnitudes of the wall-normal vorticity fluctuations in this region, as seen in figure 3.10(c). Investigation of the vortex structures over the SH surface suggests that formation of spanwise shear layers of $\partial u/\partial y$ between the high speed flow on the slip regions and the low speed flow on the adjacent no-slip regions leads to the development of additional wall-normal vorticity on the SH surface, which is further observed in figure 3.10(c). The resulting wall-normal vorticity is then bent and stretched under the mean spanwise shear, $\partial \bar{U}/\partial y$, leading to the formation of additional spanwise vorticity, observed in figure 3.10(b).

All the changes in the vorticity dynamics over the SH surface, however, are confined to the 'surface layer', in $z \lesssim g$. Outside this region, the normalized dynamics of turbulence reverts back to that of regular wall-bounded turbulent flows, as seen in figures 3.10(a-c). As a result, DR with the SH surfaces is a surface phenomenon, without any significant effect on the dynamics of turbulence in the core region.

CHAPTER IV

Effect of Interface Deformation and Comparison to Riblets

The Direct Numerical Simulation (DNS) studies reported in chapter § III, and all other simulations of Super-Hydrophobic (SH) surfaces in turbulent flow reported in the literature to date (*Min and Kim*, 2004; *Fukagata et al.*, 2006; *Martell et al.*, 2009, 2010; *Busse and Sandham*, 2012; *Park et al.*, 2013; *Jelly et al.*, 2014; *Türk et al.*, 2014; *Seo et al.*, 2015; *Jung et al.*, 2016), are based on an idealization of SH surfaces in which the liquid/gas interfaces are assumed to be flat. The liquid/gas interfaces on real SH surfaces, however, are not flat, but deform under the influence of pressure and surface tension forces, according to the Young-Laplace equation (*Ou and Rothstein*, 2005; *Tsai et al.*, 2009; *Rathgen and Mugele*, 2010). Experimental (*Steinberger et al.*, 2007; *Tsai et al.*, 2009; *Karatay et al.*, 2013a), analytical (*Sbragaglia and Prosperetti*, 2007; *Crowdy*, 2010, 2016) and computational studies (*Wang et al.*, 2014) in laminar flow have shown that interface curvature can have negligible or significant effect on the resulting slip lengths and Drag Reductions (DRs) obtained with the SH surfaces, depending on the size, geometry and orientation of the surface micro-texture relative to the flow domain, and whether the protrusion angle is positive or negative. In laminar channel flow with SH Longitudinal Micro-Grooves (LMGs) of size $0.64 \lesssim (g+w)/h \lesssim 2.56$ & $g/w = 1$ on one wall, experiments have suggested that a small negative

protrusion angle can lead to decreases of 66% to 83% in the resulting slip lengths (*Tsai et al.*, 2009), compared to the values obtained with the analytical solution of *Philip* (1972a). In laminar channel flow with SH transverse Micro-Grooves (MGs) of size $1.6 \lesssim (g+w)/h \lesssim 2$ & $0.67 \lesssim g/w \lesssim 1$ on one wall, and positive protrusion angles, *Karatay et al.* (2013a) have shown that, increasing the protrusion angle up to 10^o leads to a monotonic increase, of up to 7%, in the resulting slip lengths, while increasing the interface protrusion angle beyond 10^o leads to a monotonic drop, of up to 30%, compared to flat interfaces. Experiments of *Steinberger et al.* (2007) with a vibrating sphere over a bubble mattress have shown that at negative protrusion angles, increasing the protrusion angle leads to a monotonic decrease, of up to 30%, in the resulting slip length, while at positive protrusion angles, increasing the interface protrusion angle leads to a monotonic drop, of up to 241%, in the resulting slip length, compared to that with flat interfaces. Analytical solutions in laminar flow suggest that in the limit of vanishing confinement ratios, $(g+w)/h \to 0$, and shear-free fractions, $g/w \to 0$, the normalized slip length only depends on the interface protrusion angle (*Crowdy*, 2010). Negative protrusion angles lead to monotonic drops, of up to 20%, in the resulting slip lengths, while positive protrusion angles give rise to monotonic increases, of up to 80% (*Crowdy*, 2010). Increasing the shear-free fraction, g/w, makes the dependence of the normalized slip lengths to the protrusion angles stronger (*Wang et al.*, 2014), resulting in monotonic drops, of up to 30%, in the resulting slip lengths, with positive protrusion angles, and monotonic increases, of up to 270%, with negative protrusion angles, as shown by the computational studies of *Wang et al.* (2014) and analytical studies of *Crowdy* (2016). At larger confinement ratios, $(g+w)/h$, computational studies in channels with SH LMGs suggest that there are two distinct regimes for the effect of interface protrusion angle on the slip length, depending on the magnitude of the confinement ratio, $(g+w)/h$ (*Wang et al.*, 2014). With small confinement ratios, $(g+w)/h \sim 0.2$, and a shear-free fraction of

$g/w = 0.75$, negative protrusion angles lead to monotonic drops, of up to 18%, in the resulting slip length, while positive protrusion angles lead to monotonic increases, of up to 100% (*Wang et al.*, 2014). With large confinement ratios, $(g + w)/h \sim 3$, and $g/w = 0.75$, negative protrusion angles lead to monotonic increases, of up to 240%, in the resulting slip length, while positive protrusion angles lead to monotonic drops, of up to 100% (*Wang et al.*, 2014). The effect of interface deformation on DR with SH surfaces in turbulent flow, however, has not been studied before.

In this chapter, a first set of DNS studies of the effect of interface deformation on DR with SH LMGs in turbulent channel flow is reported. The liquid/gas interfaces in these studies were assumed to be stationary, curved and shear-free. Interface protrusion angles of $\theta = 0^o$, -30^o, -60^o and -90^o were studied in the simulations. In addition, the same geometries as those formed by the interfaces of the SH LMGs are investigated as riblets, by replacing the shear-free boundary conditions with no-slip, to compare the mechanism of DR with riblets to SH LMGs.

4.1 DNS Studies

To investigate the effect of interface curvature, a set of DNS studies were performed in turbulent channel flow with SH LMGs on the walls. The liquid/gas interfaces on the SH LMGs were modeled as stationary, curved, shear-free boundaries, with the meniscus shape determined from the balance between the pressure difference across the interface and surface tension, as given by the Young-Laplace equation (*De Gennes et al.*, 2002; *Rathgen and Mugele*, 2010)

$$\Delta\tilde{P} = -\frac{1}{We_{\tau_0}}\,\tilde{\nabla}\cdot\mathbf{n}. \tag{4.1}$$

Here, $\Delta\tilde{P} = \Delta P/\rho u_{\tau_0}^2$ is the non-dimensional Laplace pressure across the meniscus, $We_{\tau_0} = \rho u_{\tau_0}^2 g/\sigma$ is the Weber number, σ is the surface tension, g is the width of the

SH LMGs, $\mathbf{n}$ is the unit normal to the interface, and $\tilde{\nabla} \cdot ()$ denotes the divergence operator in the non-dimensional coordinate system, $(\tilde{\xi}, \tilde{\eta}, \tilde{\zeta}) = (\xi/g, \eta/g, \zeta/g)$, defined using a local coordinate system (ξ, η, ζ) centered on the SH LMG, as shown in figure 4.1.

Equation (4.1) can be integrated analytically, between $-1/2 \leq \tilde{\eta} \leq 1/2$, subject to the boundary conditions $(d\tilde{\zeta}/d\tilde{\eta})|_{(\tilde{\eta}=0)} = 0$ and $\tilde{\zeta}|_{(\tilde{\eta}=\pm 1/2)} = 0$, to give the shape of the interface, $\tilde{F}(\tilde{\eta}, \tilde{\kappa})$, as

$$\tilde{F}(\tilde{\eta}, \tilde{\kappa}) = -\frac{1}{2\tilde{\kappa}}(2\sqrt{1 - \tilde{\kappa}^2\tilde{\eta}^2} - \sqrt{4 - \tilde{\kappa}^2}), \tag{4.2}$$

where $\tilde{\kappa} = \Delta\tilde{P}\, We_{\tau_0}$ is the non-dimensional curvature of the interface, which is related to the interface protrusion angle through

$$\theta = tan^{-1}\left(\frac{\tilde{\kappa}}{2\sqrt{1 - (\tilde{\kappa}/2)^2}}\right). \tag{4.3}$$

Static interface protrusion angles of $\theta = 0^o$ ($\kappa = 1$), corresponding to flat interfaces, $\theta = -30^o$, -60^o, and -90^o ($\kappa = 2$), corresponding to maximum negative protrusion angles, were investigated by DNS. Although negative protrusion angles beyond -30^o cannot be sustained on smooth SH walls, because of the theoretical limit on the maximum possible contact angle on smooth surface (150^o) (*Nishino et al.*, 1999), this limit can be bypassed by using hierarchical, dual-structured SH surfaces in which nano-scale textures are etched on the sides of surface micro-textures (*Lee and Kim*, 2009). Hence, the full range of protrusion angles was studied by DNS.

Furthermore, to compare the mechanism of DR with SH surfaces to that with riblets, a set of DNS studies was performed in turbulent channel flow with scallop shaped riblets on the walls. The riblets in these DNS studies had the same geometries as those formed by the SH LMG interfaces, with the slip boundary condition on the curved interfaces replaced with the no-slip condition.

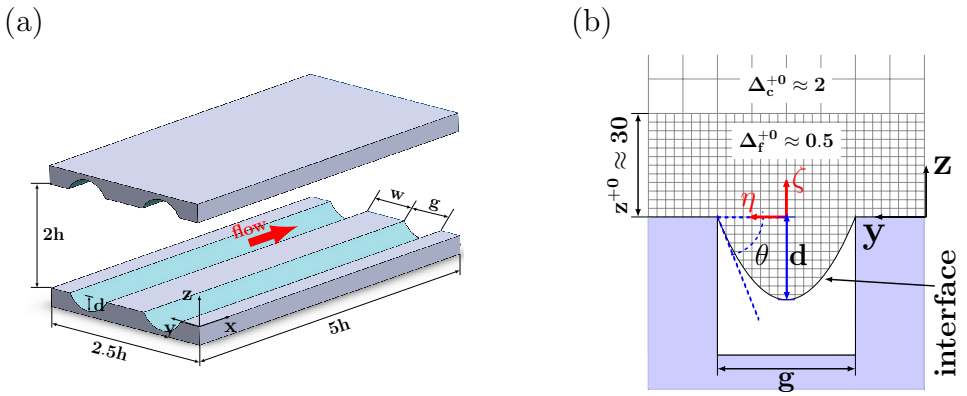

Figure 4.1: (a) Schematic of the channel and the coordinate system; (b) detailed view of the MG and the computational grid.

All the DNS studies were performed in channels of size $5h \times 2.5h \times 2h$, in the streamwise (x), spanwise (y), and wall-normal (z) directions, respectively. Grid-embedding, with $GR = 4$, was used for all the simulations. The fine grid in these studies extended from the domain boundaries up to a distance of $z^{+0} \approx 30$ away from the walls, as shown in figure 4.1. Grid resolutions of $2048 \times 1024 \times 56$ in the streamwise, spanwise, and wall-normal directions, respectively, on the fine grids, and $512 \times 256 \times 197$ in the streamwise, spanwise, and wall-normal directions, respectively, on the coarse grid, were employed in the simulations. The corresponding grid spacings were $\Delta_c^{+0} \approx 2$, and $\Delta_f^{+0} \approx 0.5$ on the coarse and fine grids, respectively, in all three directions. All the simulations were initialized from a fully developed base turbulent channel flow with no-slip walls, and $GR = 4$ grid-embedding ratio at a bulk Reynolds number of $Re_b \equiv q/2\nu = 3600$, corresponding to a friction Reynolds number $Re_{\tau_0} \approx 222$. The simulations with SH LMGs were first initialized from this base flow DNS by maintaining a constant pressure gradient in the channel. The magnitude of this pressure gradient was adjusted several times during this initial stage, to drive the flow towards the target bulk Reynolds number, $Re_b = 3600$. Once the target bulk Reynolds number was obtained, the simulations were continued by maintaining a constant flow rate in the channel.

A total of twenty one cases, corresponding to SH LMGs or riblets of size $g^{+0} \approx 14$,

28, 56 and $g/w = 7$ were studied, as reported in table 4.1. With each set of SH LMGs sizes, interface protrusion angles of $\theta = 0^o$, -30^o, -60^o, and -90^o, corresponding to non-dimensional interface curvatures of $\tilde{\kappa} = 0$, 1, 1.736, and 2, respectively, were studied in the simulations. With the interface protrusion angles of $\theta = -30^o$, -60^o, and -90^o, the slip boundary condition on the curved interfaces of the SH LMGs was replaced with the no-slip condition, to investigate DR with riblets. For comparison, all these simulations were also repeated in laminar channel flow, at $Re_b = 150$.

4.2 The Magnitude of DR in Channel Flows with Micro-Textured Walls

To analyze the results obtained with DNS, an analytical expression for the breakdown of DR in laminar and turbulent channel flows with any pattern of micro-texture on the walls, was derived. This expression separates the contributions arising from different sources to DR. Using the results obtained from DNS, the effect of each of these contributions can be evaluated and compared.

For a stationary turbulent flow in a channel with any pattern of micro-texture on the walls, the streamwise Reynolds-averaged momentum equation, is given by

$$\frac{\partial}{\partial x}(\nu\frac{\partial \bar{U}}{\partial x} - \overline{uu} - \bar{U}\bar{U}) + \frac{\partial}{\partial y}(\nu\frac{\partial \bar{U}}{\partial y} - \overline{uv} - \bar{U}\bar{V}) + \frac{\partial}{\partial z}(\nu\frac{\partial \bar{U}}{\partial z} - \overline{uw} - \bar{U}\bar{W}) = \frac{1}{\rho}\frac{\partial \bar{P}}{\partial x}, \tag{4.4}$$

where the overbar denotes Reynolds-averaging, $\bar{U}$, $\bar{V}$, $\bar{W}$ and u, v, w are the streamwise (x), spanwise (y), and wall-normal (z) components of the mean and fluctuating velocity fields, respectively, and $\bar{P}$ is the mean pressure. Equation (4.4) can also describe steady, laminar flow in a channel with any pattern of micro-textures on the walls, if u, v, and w are all set equal to zero.

In a channel large enough to accommodate the largest of turbulence structures,

	$(g+w)/2H$	0.018	0.018	0.018	0.018	0.036	0.036	0.036	0.036	0.072	0.072	0.072	0.072
	g^{+0}	14	14	14	14	28	28	28	28	56	56	56	56
	w^{+0}	2	2	2	2	4	4	4	4	8	8	8	8
	θ	0°	-30°	-60°	-90°	0°	-30°	-60°	-90°	0°	-30°	-60°	-90°
SH LMGs	DR_{lam}	13.1%	12.8%	12.8%	12.8%	20.5%	19.9%	19.7%	20.0%	32.5%	31.5%	31.8%	32.7%
	DR_{slip}	13.1%	12.7%	12.6%	12.5%	20.5%	19.6%	19.2%	19.0%	32.5%	30.8%	30.1%	29.6%
	DR_{Q_g}	-	0.1%	0.2%	0.3%	-	0.3%	0.5%	1.0%	-	0.7%	1.7%	3.1%
	DR_{turb}	36.6%	38.5%	37.2%	36.1%	48.2%	53.1%	48.1%	38.4%	59.5%	63.3%	59.6%	55.8%
	DR_{slip}	31.1%	26.9%	26.0%	26.0%	44.4%	39.4%	40.5%	45.3%	57.1%	55.1%	57.4%	60.6%
	DR_{ϵ}	5.5%	11.4%	10.8%	9.4%	3.8%	13.2%	6.5%	-9.3%	2.4%	6.9%	-0.9%	-11.2%
	$DR_{\langle\tau_c\rangle}$	-0.1%	-0.3%	-0.2%	-0.3%	-1.9%	-3.9%	-1.2%	-6.3%	-2.6%	-1.4%	-7.6%	-9.5%
	$DR_{\langle\tau_R\rangle}$	5.6%	11.7%	11.0%	9.7%	5.7%	17.1%	7.7%	-3.0%	5.0%	8.3%	6.7%	-1.7%
	$DR_{\langle\tau_R\rangle,Re_{\tau_s}}$	11.0%	8.4%	8.3%	8.4%	14.6%	10.6%	12.2%	17.6%	17.0%	14.4%	17.4%	21.5%
	$DR_{\langle\tau_R\rangle,mod}$	-5.4%	3.3%	2.7%	1.3%	-8.9%	6.5%	-4.5%	-20.6%	-12.0%	-6.1%	-10.7%	-23.2%
	DR_{Q_g}	-	0.2%	0.4%	0.7%	-	0.5%	1.1%	2.4%	-	1.3%	3.1%	6.4%
Riblets	DR_{lam}	-	1.2%	2.2%	3.0%	-	2.4%	4.4%	5.8%	-	4.9%	8.4%	11.2%
	DR_{slip}	-	1.2%	2.2%	3.0%	-	2.4%	4.3%	5.7%	-	4.8%	8.2%	10.7%
	DR_{Q_g}	-	0.0%	0.0%	0.0%	-	0.0%	0.1%	0.1%	-	0.1%	0.2%	0.5%
	DR_{turb}	-	1.2%	5.9%	10.9%	-	3.0%	5.9%	9.0%	-	2.1%	0.9%	-8.5%
	DR_{slip}	-	5.6%	9.4%	11.8%	-	11.2%	18.9%	23.8%	-	22.5%	36.6%	43.7%
	DR_{ϵ}	-	-4.4%	-3.6%	-1.0%	-	-8.3%	-13.2%	-15.3%	-	-20.7%	-36.8%	-54.8%
	$DR_{\langle\tau_c\rangle}$	-	-1.9%	-1.4%	-1.2%	-	-0.4%	-2.4%	-3.1%	-	-4.2%	-10.7%	-24.5%
	$DR_{\langle\tau_R\rangle}$	-	-2.5%	-2.2%	0.2%	-	-7.9%	-10.8%	-12.2%	-	-16.5%	-26.1%	-30.3%
	$DR_{\langle\tau_R\rangle,Re_{\tau_s}}$	-	1.4%	3.8%	4.3%	-	4.1%	8.2%	10.0%	-	10.7%	20.5%	28.6%
	$DR_{\langle\tau_R\rangle,mod}$	-	-3.9%	-6.0%	-4.1%	-	-12.0%	-19.0%	-22.2%	-	-27.2%	-46.6%	-58.9%
	DR_{Q_g}	-	0.0%	0.1%	0.1%	-	0.1%	0.2%	0.5%	-	0.3%	1.1%	2.6%

Table 4.1: Breakdown of DR in laminar and turbulent channel flow with SH LMGs or riblets.

with periodic boundary conditions in the streamwise and spanwise directions, averaging equation (4.4) over the wall-parallel directions, and integrating in the wall-normal direction from the tip of the surface micro-indentations at $z = 0$, to a height z inside the channel gives

$$\nu\langle\frac{\partial\bar{U}}{\partial z}\rangle - \langle\overline{uw}\rangle - \langle\bar{U}\bar{W}\rangle = -\frac{h}{\rho}\langle\frac{\partial\bar{P}}{\partial x}\rangle\left(1-\frac{z}{h}\right). \tag{4.5}$$

Here, $\langle\ \rangle$ denotes averaging in the wall-parallel directions, h denotes the nominal half-height of the channel, defined as the distance between the tips of the surface micro-indentations on the center of the channel, as seen in figure 2.7(a), and we have used $\left(\nu\langle\partial\bar{U}/\partial z\rangle - \langle\overline{uw}\rangle - \langle\bar{U}\bar{W}\rangle\right)|_{z=0} = -\langle\partial\overline{P}/\partial x\rangle h/\rho$, which is required by the force balance in the channel between $z = 0$ and $z = 2h$.

Integration of equation (4.5) in the wall-normal direction, once from 0 to z, and again from 0 to h (*Fukagata et al.*, 2002; *Peet and Sagaut*, 2009; *Rastegari and Akhavan*, 2015), gives

$$-\frac{h}{\rho U_{b_0}^2}\langle\frac{\partial\bar{P}}{\partial x}\rangle\left(1-3\int_0^1\left(\frac{-\langle\overline{uw}\rangle-\langle\bar{U}\bar{W}\rangle}{-\frac{h}{\rho}\langle\frac{\partial\bar{P}}{\partial x}\rangle}\right)(1-\chi)\,d\chi\right) = \frac{3}{Re_b}\left(1-\frac{Q_g}{Q}-\frac{U_s}{U_{b_0}}\right), \tag{4.6}$$

where U_{b_0} is the bulk velocity in a 'base' turbulent channel flow with smooth no-slip walls at the same bulk Reynolds number, $Re_b \equiv q/2\nu$, hence the same flow rate per unit spanwise width, $q \equiv Q/L_y$, and the same flow rate, Q, as the channel with micro-textured walls, and a cross-sectional area, A_0, equal to the 'nominal' cross-sectional area, A_n, of the channel with micro-textured walls, as defined by the area enclosed between the tips of the surface micro-indentations on the opposing walls of the channel; Q_g is the volume flow rate through the micro-texture indentations; $U_s \equiv \langle\bar{U}\rangle|_{z=0}$ is the average slip velocity at the tip of the surface micro-texture; and $\chi = z/h$ is the non-dimensional wall-normal coordinate. Equation (4.6) can be

rearranged as

$$-\frac{h}{\rho U_{b_0}^2}\langle\frac{\partial \bar{P}}{\partial x}\rangle = \frac{3}{Re_b}\left(1-\frac{Q_g}{Q}-\frac{U_s}{U_{b_0}}\right)\left(\frac{1}{1-3I}\right), \tag{4.7}$$

where the integral I is defined as

$$\begin{aligned} I &= \frac{1}{-\langle\frac{\partial \bar{P}}{\partial x}\rangle\frac{h}{\rho}}\int_0^1 \left(-\langle\overline{uw}\rangle - \langle\bar{U}\bar{W}\rangle\right)(1-\chi)\,d\chi \\ &= \frac{1}{-\langle\frac{\partial \bar{P}}{\partial x}\rangle\frac{h}{\rho}}\int_0^1 \left(\langle\tau_R\rangle + \langle\tau_c\rangle\right)(1-\chi)\,d\chi \\ &= I_{\langle\tau_R\rangle} + I_{\langle\tau_c\rangle}. \end{aligned} \tag{4.8}$$

The integral I denotes the contributions of the Reynolds shear stress, $\langle\tau_R\rangle \equiv -\langle\overline{uw}\rangle$, and any mean convective shear stresses, $\langle\tau_c\rangle \equiv -\langle\bar{U}\bar{W}\rangle$, to the overall wall shear stress in the channel with micro-textured walls, and I is bounded by $0 < I < 1/3$ per equation (4.5). For the base channel flow with smooth no-slip walls, equation (4.7) reduces to

$$-\frac{h}{\rho U_{b_0}^2}\langle\frac{\partial \bar{P}}{\partial x}\rangle_0 = \frac{3}{Re_b}\left(\frac{1}{1-3I_0}\right), \tag{4.9}$$

where

$$\begin{aligned} I_0 &= \frac{1}{-\langle\frac{\partial \bar{P}}{\partial x}\rangle_0\frac{h}{\rho}}\int_0^1 -\langle\overline{uw}\rangle_0\,(1-\chi)d\chi \\ &= \frac{1}{-\langle\frac{\partial \bar{P}}{\partial x}\rangle_0\frac{h}{\rho}}\int_0^1 \langle\tau_R\rangle_0\,(1-\chi)d\chi \\ &= I_{\langle\tau_R\rangle_0}. \end{aligned} \tag{4.10}$$

Defining the DR as

$$DR \equiv \left(1-\frac{C_d}{C_{d_0}}\right), \tag{4.11}$$

the magnitude of DR can be expressed as

$$DR \equiv \left(1 - \frac{C_d}{C_{d_0}}\right) = \left(1 - \frac{\left(\frac{F_d}{\rho(Q/A_n)^2 A}\right)}{\left(\frac{F_{d_0}}{\rho(Q/A_0)^2 A_0}\right)}\right) = \left(1 - \frac{\langle \frac{\partial \bar{P}}{\partial x} \rangle}{\langle \frac{\partial \bar{P}}{\partial x} \rangle_0}\right), \tag{4.12}$$

where $C_d \equiv F_d \,/\, [\rho\ (Q/A_n)^2 A]$ and $C_{d_0} \equiv F_{d_0} \,/\, [\rho\ (Q/A_0)^2 A_0]$ are the drag coefficients, F_d and F_{d_0} are the drag forces, A and A_0 are the cross-sectional areas, and (Q/A_n) and (Q/A_0) are the characteristic velocities in the channel with micro-textured walls and the base channel flow, respectively. Here, the characteristic velocity in the channel with micro-textured walls has been defined using its 'nominal' cross-sectional area, A_n, instead of its actual cross-sectional area, A, because many surface micro-textures do not allow any net flow rate through the micro-indentations, and even with micro-texture, such as SH LMGs or riblets, which do allow a flow through, both the present DNS studies, as well as prior investigations (*García-Mayoral and Jiménez*, 2011), show that the fractional flow rate, Q_g/Q, through the SH LMG or riblet indentations is disproportionately low compared to the fractional cross-sectional area, A_g/A, of the micro-grooves, such that (Q/A_n) provides a much better estimate of the characteristic velocity in the micro-textured channel than (Q/A).

Substitution of equations (4.7) and (4.9) into equation (4.12) gives the magnitude of DR as

$$\begin{aligned} DR &= \left\{\frac{U_s}{U_{b_0}}\right\} + \left\{(1 - \frac{U_s}{U_{b_0}} - \frac{Q_g}{Q})(\frac{3\varepsilon}{1-3I})\right\} + \left\{\frac{Q_g}{Q}\right\} \\ &= \{DR_{slip}\} + \{DR_\varepsilon\} + \left\{DR_{Q_g}\right\}, \end{aligned} \tag{4.13}$$

where $\varepsilon = (I_0 - I)$ is the difference between the values of the I integrals in the base channel flow and the channel flow with micro-textured walls.

The quantity $\varepsilon = (I_0 - I) = (I_{\langle \tau_R \rangle_0} - I_{\langle \tau_R \rangle} - I_{\langle \tau_c \rangle})$ in equation (4.13) is a measure of the differences in the normalized structure and dynamics of turbulence and the mean

flow in the channel with micro-textured walls compared to the base turbulent channel flow with smooth no-slip walls. These two effects can be separated by decomposing ε into

$$\varepsilon = \varepsilon_{\langle\tau_R\rangle} + \varepsilon_{\langle\tau_c\rangle}, \tag{4.14}$$

where $\varepsilon_{\langle\tau_R\rangle} = (I_{\langle\tau_R\rangle_0} - I_{\langle\tau_R\rangle})$ represents the changes in the normalized structure of the turbulence, and $\varepsilon_{\langle\tau_c\rangle} = (-I_{\langle\tau_c\rangle})$ represents any changes in the structure of the mean flow. The contributions to $\varepsilon_{\langle\tau_R\rangle}$, in turn, can be further decomposed into two effects: (a) changes in $\langle\tau_R\rangle$ attributable to the drop in the friction Reynolds number of the flow due to the presence of the slip velocity at the tip of surface micro-indentations, and (b) other changes in $\langle\tau_R\rangle$ attributable to other modifications to the structure and dynamics of turbulence due to the presence of the surface micro-textures on the walls. These two effects can be separated by decomposing $\varepsilon_{\langle\tau_R\rangle}$ into

$$\varepsilon_{\langle\tau_R\rangle} = \varepsilon_{\langle\tau_R\rangle,Re_{\tau_s}} + \varepsilon_{\langle\tau_R\rangle,mod}, \tag{4.15}$$

where $\varepsilon_{\langle\tau_R\rangle,Re_{\tau_s}} = (I_{\langle\tau_R\rangle_0} - I_{\langle\tau_R\rangle,Re_{\tau_s}})$ represents the change in the I integral in a smooth-walled, no-slip turbulent channel flow when the friction Reynolds number is dropped from Re_{τ_0} to Re_{τ_s}, where $Re_{\tau_s} = Re_{\tau_0}\sqrt{(1 - U_s/U_{b_0})}$ is the friction Reynolds number which would be obtained in the channel with micro-textured walls based on the effect of the wall slip-velocity alone, and $\varepsilon_{\langle\tau_R\rangle,mod} = (I_{\langle\tau_R\rangle,Re_{\tau_s}} - I_{\langle\tau_R\rangle})$ represents any other changes in the I integral due to the presence of the micro-texture on the walls, and $I_{\langle\tau_R\rangle,Re_{\tau_s}} = 1/(-\langle\partial\bar{P}/\partial x\rangle_{Re_{\tau_s}} h/\rho)\int_0^1 -\langle\overline{uw}\rangle_{Re_{\tau_s}}(1-\chi)d\chi$ is the I integral in a smooth-walled, no-slip turbulent channel flow with friction Reynolds number equal to Re_{τ_s}.

Using this decomposition, equation (4.13) can be written as

$$\begin{aligned}
DR &= \left\{\frac{U_s}{U_{b_0}}\right\} + \left\{\left(1 - \frac{U_s}{U_{b_0}} - \frac{Q_g}{Q}\right)\left(\frac{3\varepsilon}{1-3I}\right)\right\} + \left\{\frac{Q_g}{Q}\right\} \\
&= \{DR_{slip}\} + \{DR_{\varepsilon}\} + \left\{DR_{Q_g}\right\} \\
&= \left\{\frac{U_s}{U_{b_0}}\right\} + \left\{\left(1 - \frac{U_s}{U_{b_0}} - \frac{Q_g}{Q}\right)\left(\frac{3(\varepsilon_{\langle\tau_R\rangle} + \varepsilon_{\langle\tau_c\rangle})}{1-3I}\right)\right\} + \left\{\frac{Q_g}{Q}\right\} \\
&= \{DR_{slip}\} + \left\{DR_{\langle\tau_R\rangle} + DR_{\langle\tau_c\rangle}\right\} + \left\{DR_{Q_g}\right\} \\
&= \left\{\frac{U_s}{U_{b_0}}\right\} + \left\{\left(1 - \frac{U_s}{U_{b_0}} - \frac{Q_g}{Q}\right)\left(\frac{3(\varepsilon_{\langle\tau_R\rangle,Re_{\tau_s}} + \varepsilon_{\langle\tau_R\rangle,mod} + \varepsilon_{\langle\tau_c\rangle})}{1-3I}\right)\right\} + \left\{\frac{Q_g}{Q}\right\} \\
&= \{DR_{slip}\} + \left\{DR_{\langle\tau_R\rangle,Re_{\tau_s}} + DR_{\langle\tau_R\rangle,mod} + DR_{\langle\tau_c\rangle}\right\} + \left\{DR_{Q_g}\right\}. \qquad (4.16)
\end{aligned}$$

Equation (4.16) provides an analytical expression for the magnitude of DR in laminar or turbulent channel flow with any pattern of SH or riblet micro-textures on the walls, while providing a breakdown of DR into five contributions: (i) the DR arising from the effective slip on the wall, as embodied in the normalized average slip velocity at the tip of the wall micro-indentations, $\{U_s/U_{b_0}\}$, represented by $\{DR_{slip}\}$; (ii) the DR arising from changes to the structure of turbulence due to the drop in the friction Reynolds number of the flow due to the presence of this effective slip at the wall, represented by $\left\{DR_{\langle\tau_R\rangle,Re_{\tau_s}}\right\}$; (iii) the DR or Drag Increase (DI) arising from other modifications to the normalized structure and dynamics of turbulence due to the presence of the micro-textures on the walls, represented by $\left\{DR_{\langle\tau_R\rangle,mod}\right\}$; (iv) the DR or DI arising from modifications to the structure of the mean flow due to the presence of the micro-texture on the walls, represented by $\left\{DR_{\langle\tau_c\rangle}\right\}$; and (v) small, and generally insignificant, DR arising from the fractional flow rate $\{Q_g/Q\}$ through the micro-texture indentations, represented by $\left\{DR_{Q_g}\right\}$. For 'idealized' SH channel flows with 'flat' liquid/gas interfaces, $Q_g = 0$, and equations (4.13) and (4.16) reduce to equation (3.5).

The integral $I_{\langle\tau_R\rangle,Re_{\tau_s}}$, required for the evaluation of $\varepsilon_{\langle\tau_R\rangle,Re_{\tau_s}}$, can be computed directly from its definition, $I_{\langle\tau_R\rangle,Re_{\tau_s}} = \left[1/(-\langle\partial\bar{P}/\partial x\rangle_{Re_{\tau_s}} h/\rho)\right] \int_0^1 -\langle\overline{uw}\rangle_{Re_{\tau_s}}(1 -$

$\chi)d\chi$, by performing additional DNS in smooth-walled, no-slip turbulent channel flows at friction Reynolds number equal to Re_{τ_s}. This is the approach adopted in this thesis. Alternatively, $I_{\langle\tau_R\rangle,Re_{\tau_s}}$ can be computed using the relation $I_{\langle\tau_R\rangle,Re_{\tau_s}} = (1/3)\left[1-(3/Re_{b_s})(U_{b_s}/u_{\tau_s})^2\right]$, which can be obtained from the analog of equation (4.9) for a smooth-walled, no-slip turbulent channel flow at a bulk Reynolds number Re_{b_s} and a friction Reynolds number Re_{τ_s}. The term $I_{\langle\tau_R\rangle,Re_{\tau_s}}$ can then be evaluated using estimates of (U_{b_s}/u_{τ_s}) from experimental correlations such as Dean's correlation (*Dean*, 1978).

4.3 Results

4.3.1 DR and its Breakdown in Channel Flows with SH LMGs or Riblets on the Walls

Figure 4.2 shows the normalized slip velocities, DRs and breakdown of DR, obtained in DNS of laminar and turbulent channel flow with SH LMGs or riblets on the walls. In laminar channel flow with SH LMGs on the walls, equation (4.13) reduces to $DR = DR_{slip} + DR_{Q_g}$, where $DR_{slip} = U_s/U_{b_0}$ is the normalized slip velocity and $DR_{Q_g} = Q_g/Q_0$ is the fraction of flow rate through the micro-texture indentations. The contribution to DR arising from DR_{Q_g} is generally negligible, except for large SH LMGs, where it can be as large as 3%, as shown in figures 4.2(b,c) and table 4.1. The normalized wall slip velocity, U_s/U_{b_0}, hence DR_{slip}, increases with increasing MG width for both SH LMGs and riblets, as shown in figure 4.2(a). However, the normalized slip velocities obtained with SH LMGs are $\sim$ 3 to 10 times larger than those obtained with riblets, depending on the width and depth of the MGs. Interface protrusion angle has a small effect on the resulting slip velocities and DRs with SH LMGs, leading to drops of up to 3% in DR_{slip} and up to 1% in DR, compared to flat interfaces. With riblets, however, the effect of interface protrusion angle on the

resulting slip velocities and DRs is more pronounced. Increasing the riblet MG depth from $d/g = 1/7$ ($\theta = -30^o$) to $d/g = 1/2$ ($\theta = -90^o$) led to increases of $\sim 220\%$ to 250% in both the slip velocity and DR. The drop in the slip velocities obtained with the SH LMGs, as the protrusion angle increases, and the increase in the slip velocities obtained with riblets, as the MG depth increases, both arise from the displacement of the boundary condition inside the MGs away from the tip of the MG. Such a displacement weakens the effect of the boundary conditions on the slip velocity at the tip of MGs, thus resulting in a drop of the slip velocities with SH LMGs, and an increase in the slip velocities with riblets.

Similar features to those observed in laminar flow for DR_{Q_g} and DR_{slip}, can also be observed in turbulent flow, as seen in figures 4.2(d,f) and table 4.1. However, the magnitude of DR_{Q_g} in turbulent flow is larger than in laminar flow with both SH LMGs and riblets. Similarly, the normalized slip velocities, U_s/U_{b_0}, in turbulent flow are larger than those in laminar flow for both SH LMGs and riblets, by factors of ~ 2 and $\sim 4-5$, respectively. The effect of interface protrusion angle on the slip velocities with SH LMGs in turbulent flow also remains minor, giving rise to drops of up to 5% or increases of up to 3.5% in DR_{slip}, compared to flat interfaces, depending on whether the maximum interface depth is $d^+ \gtrsim 10$ or $d^+ \lesssim 10$. In the latter case, when the maximum interface depth is $d^+ \lesssim 10$, the trends in the slip velocities remain similar to this in laminar flow. In the former case, when maximum interface depth is $d^+ \gtrsim 10$, the MGs are deep enough for the flow inside the SH LMGs to become turbulent, resulting in an enhancement of the slip velocities compared to flat interfaces. With riblets, the normalized slip velocities increase by a factor of ~ 2, regardless of MG size, as the riblet MG depth increases from $d/g = 1/7$, at $\theta = -30^o$, to $d/g = 1/2$, at $\theta = -90^o$, similar to laminar flow.

The trends of DR_{slip} in turbulent flow, however, do not translate into similar trends in the resulting DRs, because there are additional contributions arising from

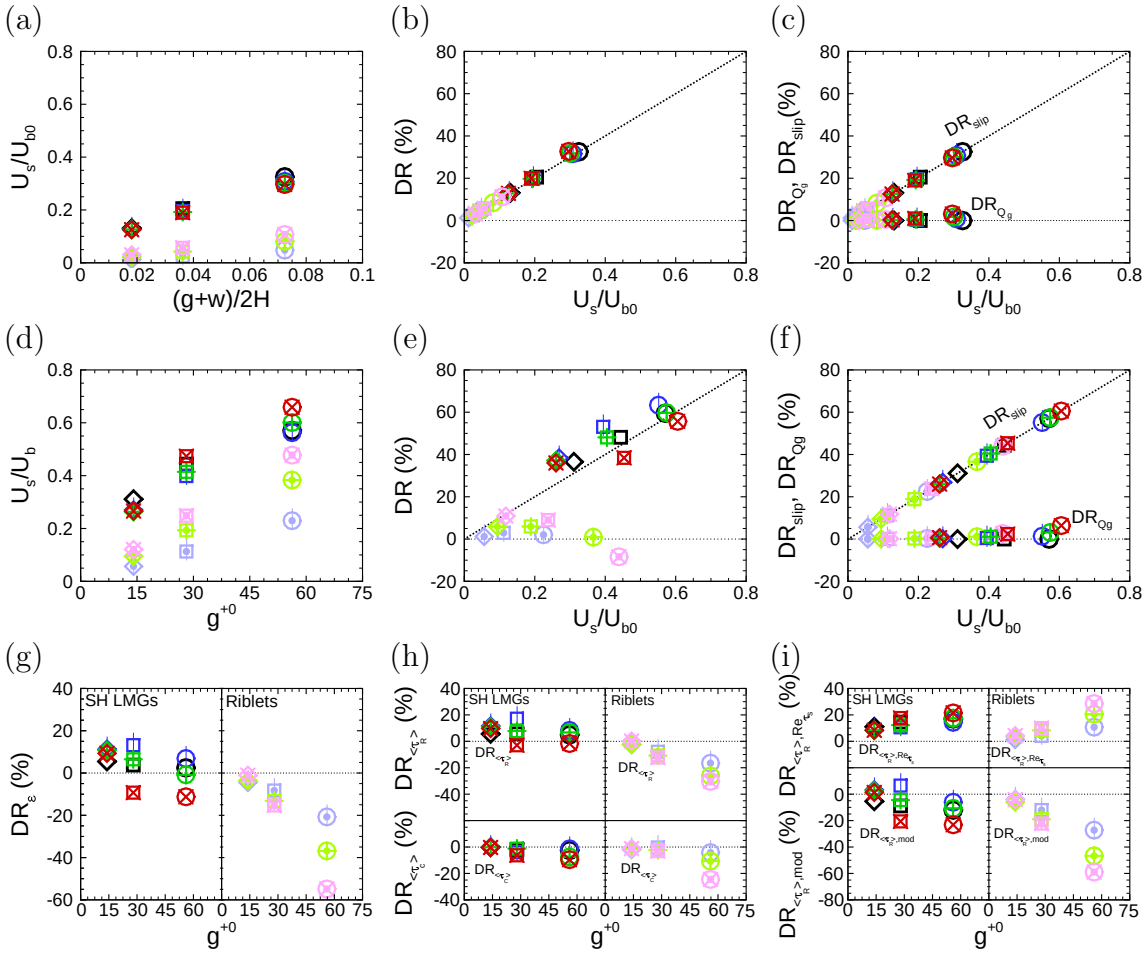

Figure 4.2: Normalized slip velocities, DRs and breakdown of DRs in laminar and turbulent channel flow with SH LMGs and riblets: (a,b,c) Normalized slip velocity, DR, and breakdown of DR in laminar channel flow with SH LMGs or riblets; (d,e,f) normalized slip velocity, DR, and breakdown of DR in turbulent channel flow with SH LMGs or riblets; (g,h,i) DR arising from DR_ε, $DR_{\langle\tau_R\rangle}$, $DR_{\langle\tau_c\rangle}$, $DR_{\langle\tau_R\rangle,Re_{\tau_s}}$ and $DR_{\langle\tau_R\rangle,mod}$ in turbulent channel flow with SH LMGs or riblets. $\diamond$, $\square$, $\bigcirc$, SH LMGs, $\theta = 0^o$, $g^{+0} = 14, 28, 56$; $\diamondsuit$, $\square\!\!\!\square$, $\bigcirc\!\!\!\!\bigcirc$, SH LMGs, $\theta = -30^o$, $g^{+0} = 14, 28, 56$; $\diamondsuit$, $\boxplus$, $\oplus$, SH LMGs, $\theta = -60^o$, $g^{+0} = 14, 28, 56$; $\diamondsuit$, $\boxtimes$, $\otimes$, SH LMGs, $\theta = -90^o$, $g^{+0} = 14, 28, 56$, respectively; $\diamondsuit$, $\square\!\!\!\square$, $\bigcirc\!\!\!\!\bigcirc$, riblets, $\theta = -30^o$, $g^{+0} = 14, 28, 56$; $\diamondsuit$, $\boxplus$, $\oplus$, riblets, $\theta = -60^o$, $g^{+0} = 14, 28, 56$; $\diamondsuit$, $\boxtimes$, $\otimes$, riblets, $\theta = -90^o$, $g^{+0} = 14, 28, 56$; $\cdots$, $\mathrm{DR} = U_s/U_{b_0}$.

the modifications to the normalized structure and dynamics of turbulence and the mean flow, embodied in DR_ε, as predicted by equation (4.13) and shown in figures 4.2(e,g). With SH LMGs, the contributions from DR_ε can result in up to $\sim 13\%$ additional DR at low protrusion angles ($\theta = -30^o$), and up to -11% Drag Increase (DI) at high protrusion angles ($\theta = -90^o$). As a result of these contributions, for a given SH LMG width, the highest DRs were always obtained at low protrusion angles ($\theta = -30^o$), and the lowest DRs were always obtained at high protrusion angles ($\theta = -90^o$). The resulting overall DRs differ from those obtained with flat interfaces by up to $+5\%$ to -10%, for low and high protrusion angles, respectively. With riblets, the contributions of DR_ε are always drag increasing. But the magnitude of DR_{slip} significantly increases for riblets of size $g^{+0} \gtrsim 14$, as seen in figure 4.2(g). This drag reducing contribution from DR_ε negates the drag reducing effect of DR_{slip}, and leads to diminishing DRs for riblets of size $g^{+0} \gtrsim 14$ and eventual DIs with riblets of size $g^{+0} \gtrsim 28$, as seen in figure 4.2(e). This drop in DR with riblets of MG size $g^+ \gtrsim 15$ is a well-known feature of DR with riblets, which has been observed in many experimental studies of riblet DR (*Bushnell and Hefner*, 1990; *Bechert et al.*, 1997), as shown in figure 4.3.

The contributions to DR arising from DR_ε can be broken down into $DR_\varepsilon = DR_{\langle\tau_R\rangle} + DR_{\langle\tau_c\rangle}$, as given by equation (4.16), where $DR_{\langle\tau_R\rangle}$ represents the contributions arising from modifications to the Reynolds shear stresses, and $DR_{\langle\tau_c\rangle}$ represents the contributions arising from any mean convective shear stresses developed in the presence of the wall micro-texture. Analysis of DNS results show that the contributions arising from mean convective shear stresses, $DR_{\langle\tau_c\rangle}$, are always drag increasing with both SH LMGs and riblets, as shown in figure 4.2(h) and table 4.1. The contributions arising from modifications to the Reynolds shear stresses, $DR_{\langle\tau_R\rangle}$, are shown by DNS to be always drag increasing with riblets of any size and SH LMGs of depth $d^+ \gtrsim 10$, and only moderately drag reducing with SH LMGs of depth $d^+ \lesssim 10$, as

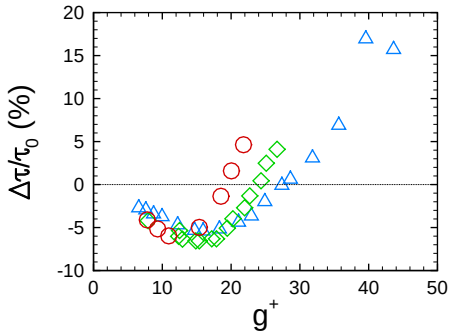

Figure 4.3: Wall-friction reduction with scallop shape riblets in turbulent boundary layer flow as a function of riblet size: △, experiments of *Bechert et al.* (1997), $d/g = 0.5$; ◇, experiments of *Bechert et al.* (1997), $d/g = 0.7$; ◯, experiments of *Bechert et al.* (1997), $d/g = 1.0$.

seen in figure 4.2(h). The finding that $DR_{\langle\tau_R\rangle}$ is always drag increasing with riblets, indicates that the contributions arising from modifications to the Reynolds shear stresses are always drag increasing with riblets. This stands in contrast with current understanding of the mechanism of DR with riblets, which has always attributed DR with riblets to the weakening of turbulent vortical structures in the near wall region (*Bushnell and Hefner*, 1990; *Choi et al.*, 1993; *Bechert et al.*, 1997; *Karniadakis and Choi*, 2003; *García-Mayoral and Jiménez*, 2011).

The contributions arising from modifications to the Reynolds shear stresses, $DR_{\langle\tau_R\rangle}$, can be further broken down into $DR_{\langle\tau_R\rangle} = DR_{\langle\tau_R\rangle,Re_{\tau_s}} + DR_{\langle\tau_R\rangle,mod}$, as shown by equation (4.16), where $DR_{\langle\tau_R\rangle,Re_{\tau_s}}$ represents the DR arising from modifications to the turbulence structure due to the drop in the friction Reynolds number of the flow from Re_{τ_0} to the friction Reynolds number, Re_{τ_s}, which would be obtained in the channel because of the effect of the wall slip velocity alone, and $DR_{\langle\tau_R\rangle,mod}$ represents the DR or DI arising from any other modifications to the normalized structure of turbulence in the presence of the wall micro-texture. The contributions arising from $DR_{\langle\tau_R\rangle,Re_{\tau_s}}$ are always drag reducing by definition, as shown in figure 4.2(i) and table 4.1. The contributions from the $DR_{\langle\tau_R\rangle,mod}$ are shown by DNS results to be drag

increasing for riblets of any size and SH LMGs of size $g^+ \gtrsim 20$, and only minimally drag reducing for SH LMGs with deformed interfaces of size $g^+ \lesssim 20$, contributing no more than 6.5% DR.

Overall, these results point to a common mechanism of DR for both SH LMGs and riblets, in which 90% to 100% of the DR with SH LMGs and 100% of the DR with riblets arises from surface slip, modifications to the normalized structure of turbulence due to the drop in the friction Reynolds number of the flow because of this surface slip, and the negligible flow rate through the wall micro-texture. Modifications to the structure of turbulence, beyond the effect of the drop in the friction Reynolds of the flow due to the presence of surface slip, were always drag increasing with riblets and SH LMGs of size $g^+ \gtrsim 20$, and only minimally drag reducing with SH LMGs with deformed interfaces of size $g^+ \lesssim 20$, contributing no more than 6.5% DR.

4.3.1.1 On the Definition of DR

In the derivations of equations (4.13) and (4.16) in section 4.2, DR was defined as $DR \equiv (1 - C_d/C_{d_0})$, based on the drag coefficient, C_d, rather than the more conventional definition $DR_f \equiv (1 - C_f/C_{f_0})$, which is based on the friction coefficient, C_f. This choice was made because the drag coefficient, C_d, is a more direct measure of the drag force, which is the main quantity of interest in skin-friction DR. Furthermore, defining the DR based on C_d circumvents the need to define the wall shear stress on 'fictitious' or 'virtual' planes (*García-Mayoral and Jiménez*, 2011), or based on the hydraulic radius from 'virtual' origins (*Luchini*, 1995), both of which have proved problematic in assessing the true magnitude of DR in internal flows (*García-Mayoral and Jiménez*, 2011; *Luchini*, 1995).

In practice, the difference between the DR as defined by equation (4.12) and DR as defined by $DR_f \equiv (1 - C_f/C_{f_0})$ is small, and does not change any of the conclusions

of the present study. Specifically, if one were to define the DR as

$$DR_f \equiv \left(1 - \frac{C_f}{C_{f_0}}\right) = \left(1 - \frac{\left(\frac{\langle \tau_w \rangle}{\rho (Q/A_n)^2}\right)}{\left(\frac{\langle \tau_{w_0} \rangle}{\rho (Q/A_0)^2}\right)}\right) = \left(1 - \frac{\langle \frac{\partial \bar{P}}{\partial x} \rangle A}{\langle \frac{\partial \bar{P}}{\partial x} \rangle_0 A_0}\right), \tag{4.17}$$

equation (4.16) would be modified to

$$\begin{aligned}
DR_f =& \left\{ (\frac{A}{A_0})(\frac{U_s}{U_{b_0}}) \right\} + \left\{ (\frac{A}{A_0}) \left(1 - \frac{U_s}{U_{b_0}} - \frac{Q_g}{Q}\right) \left(\frac{3\varepsilon}{1-3I}\right) \right\} + \left\{ 1 - (\frac{A}{A_0})(1 - \frac{Q_g}{Q}) \right\} \\
=& \left\{ (\frac{A}{A_0})(\frac{U_s}{U_{b_0}}) \right\} + \left\{ (\frac{A}{A_0}) \left(1 - \frac{U_s}{U_{b_0}} - \frac{Q_g}{Q}\right) \left(\frac{3\left(\varepsilon_{\langle \tau_R \rangle, Re_{\tau_s}} + \varepsilon_{\langle \tau_R \rangle, mod} + \varepsilon_{\langle \tau_c \rangle}\right)}{1-3I}\right) \right\} \\
&+ \left\{ 1 - (\frac{A}{A_0})(1 - \frac{Q_g}{Q}) \right\} \\
=& \left\{ DR_{f,slip} \right\} + \left\{ DR_{f,\langle \tau_R \rangle, Re_{\tau_s}} + DR_{f,\langle \tau_R \rangle, mod} + DR_{\langle \tau_c \rangle} \right\} + \left\{ DR_{f,Q_g} \right\} \\
=& \left\{ DR_{f,slip} \right\} + \left\{ DR_{f,\varepsilon} \right\} + \left\{ DR_{f,Q_g} \right\}.
\end{aligned} \tag{4.18}$$

Figures 4.4 and 4.5 and table 4.2 show the comparison between DR, and its breakdown as defined in equation (4.18), and DR_f and its breakdown, as defined in equation (4.18) for all the turbulent channel flow simulations with SH LMGs and riblets reported in the present study. The magnitudes and the trends in the data for DR_f, $DR_{f,\varepsilon}$, $DR_{f,\langle \tau_R \rangle, Re_{\tau_s}}$, $DR_{f,\langle \tau_R \rangle, mod}$ and $DR_{f,\langle \tau_c \rangle}$ are seen to be similar to those in the data for DR, DR_ε, $DR_{\langle \tau_R \rangle, Re_{\tau_s}}$, $DR_{\langle \tau_R \rangle, mod}$ and $DR_{\langle \tau_c \rangle}$, respectively. The magnitude of $DR_{f,slip}$ is higher than DR_{slip} by a factor equal to A/A_0, per its definition, while the presence of the same A/A_0 factor in the definition of DR_{f,Q_g} leads to negative values of DR_{f,Q_g}, while DR_{Q_g} always remains positive, as would be physically plausible. Overall, these results indicate that DR, as defined by equation (4.12), provides a more physically plausible definition of DR than the more conventional definition, DR_f, given by equation (4.17).

Another quantity of interest in internal flows is the power requirement for pumping a desired flow rate, Q, of a fluid through a channel of a given 'nominal' cross-sectional

	$g^{+0}(turb)$	14	14	14	14	28	28	28	28	56	56	56	56
	$w^{+0}(turb)$	2	2	2	2	4	4	4	4	8	8	8	8
	$(g+w)/2H$	0.018	0.018	0.018	0.018	0.036	0.036	0.036	0.036	0.072	0.072	0.072	0.072
	θ	0°	-30°	-60°	-90°	0°	-30°	-60°	-90°	0°	-30°	-60°	-90°
	A/A_0	1	1.006	1.012	1.023	1	1.011	1.024	1.044	1	1.021	1.046	1.088
SH LMGs	DR_{lam}	13.1%	12.8%	12.8%	12.8%	20.5%	19.9%	19.7%	20.0%	32.5%	31.5%	31.8%	32.7%
	DR_{slip}	13.1%	12.7%	12.6%	12.5%	20.5%	19.6%	19.2%	19.0%	32.5%	30.8%	30.1%	29.6%
	DR_{Q_g}	-	0.1%	0.2%	0.3%	-	0.3%	0.5%	1.0%	-	0.7%	1.7%	3.1%
	DR_{turb}	36.6%	38.5%	37.2%	36.1%	48.2%	53.1%	48.1%	38.4%	59.5%	63.3%	59.6%	55.8%
	DR_{slip}	31.1%	26.9%	26.0%	26.0%	44.4%	39.4%	40.5%	45.3%	57.1%	55.1%	57.4%	60.6%
	DR_{ϵ}	5.5%	11.4%	10.8%	9.4%	3.8%	13.2%	6.5%	-9.3%	2.4%	6.9%	-0.9%	-11.2%
	$DR_{\langle\tau_c\rangle}$	-0.1%	-0.3%	-0.2%	-0.3%	-1.9%	-3.9%	-1.2%	-6.3%	-2.6%	-1.4%	-7.6%	-9.5%
	$DR_{\langle\tau_R\rangle}$	5.6%	11.7%	11.0%	9.7%	5.7%	17.1%	7.7%	-3.0%	5.0%	8.3%	6.7%	-1.7%
	$DR_{\langle\tau_R\rangle,Re_{\tau_s}}$	11.0%	8.4%	8.3%	8.4%	14.6%	10.6%	12.2%	17.6%	17.0%	14.4%	17.4%	21.5%
	$DR_{\langle\tau_R\rangle,mod}$	-5.4%	3.3%	2.7%	1.3%	-8.9%	6.5%	-4.5%	-20.6%	-12.0%	-6.1%	-10.7%	-23.2%
	DR_{Q_g}	-	0.2%	0.4%	0.7%	-	0.5%	1.1%	2.4%	-	1.3%	3.1%	6.4%
Riblets	DR_{lam}	-	1.2%	2.2%	3.0%	-	2.4%	4.4%	5.8%	-	4.9%	8.4%	11.2%
	DR_{slip}	-	1.2%	2.2%	3.0%	-	2.4%	4.3%	5.7%	-	4.8%	8.2%	10.7%
	DR_{Q_g}	-	0.0%	0.0%	0.0%	-	0.0%	0.1%	0.1%	-	0.1%	0.2%	0.5%
	DR_{turb}	-	1.2%	5.9%	10.9%	-	3.0%	5.9%	9.0%	-	2.1%	0.9%	-8.5%
	DR_{slip}	-	5.6%	9.4%	11.8%	-	11.2%	18.9%	23.8%	-	22.5%	36.6%	43.7%
	DR_{ϵ}	-	-4.4%	-3.6%	-1.0%	-	-8.3%	-13.2%	-15.3%	-	-20.7%	-36.8%	-54.8%
	$DR_{\langle\tau_c\rangle}$	-	-1.9%	-1.4%	-1.2%	-	-0.4%	-2.4%	-3.1%	-	-4.2%	-10.7%	-24.5%
	$DR_{\langle\tau_R\rangle}$	-	-2.5%	-2.2%	0.2%	-	-7.9%	-10.8%	-12.2%	-	-16.5%	-26.1%	-30.3%
	$DR_{\langle\tau_R\rangle,Re_{\tau_s}}$	-	1.4%	3.8%	4.3%	-	4.1%	8.2%	10.0%	-	10.7%	20.5%	28.6%
	$DR_{\langle\tau_R\rangle,mod}$	-	-3.9%	-6.0%	-4.1%	-	-12.0%	-19.0%	-22.2%	-	-27.2%	-46.6%	-58.9%
	DR_{Q_g}	-	0.0%	0.1%	0.1%	-	0.1%	0.2%	0.5%	-	0.3%	1.1%	2.6%

Table 4.2: Comparison of DR and its breakdown to DR_f and its breakdown.

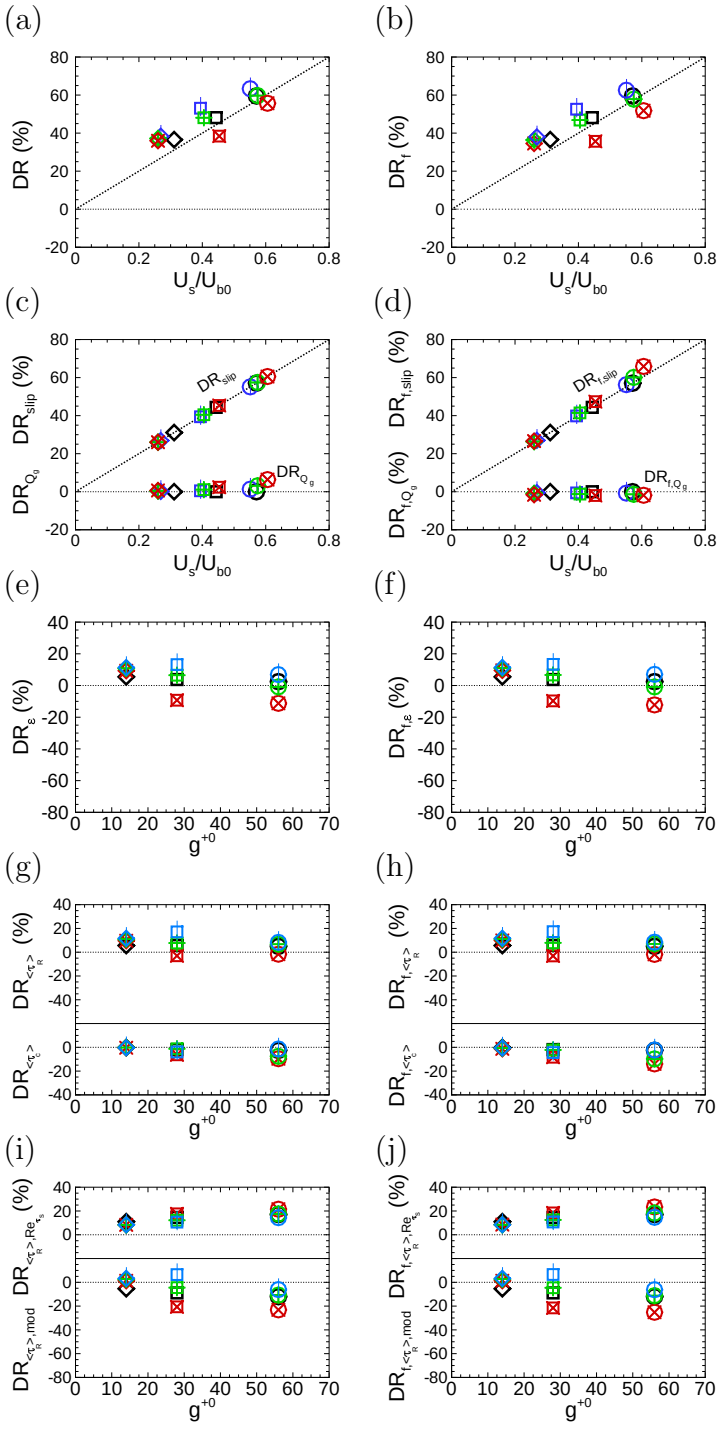

Figure 4.4: Comparison of DR and DR_f in turbulent channel flow with SH LMGs: (a,c,e,g,i) DR; (b,d,f,h,j) DR_f; ◇, □, ◯, $\theta = 0$, $g^{+0} = 14$, 28, 56, respectively; ◈, ⊟, ◍, $\theta = -30$, $g^{+0} = 14$, 28, 56, respectively; ⟐, ⊞, ⊕, $\theta = -60$, $g^{+0} = 14$, 28, 56, respectively; ⟡, ⊠, ⊗, $\theta = -90$, $g^{+0} = 14$, 28, 56, respectively.

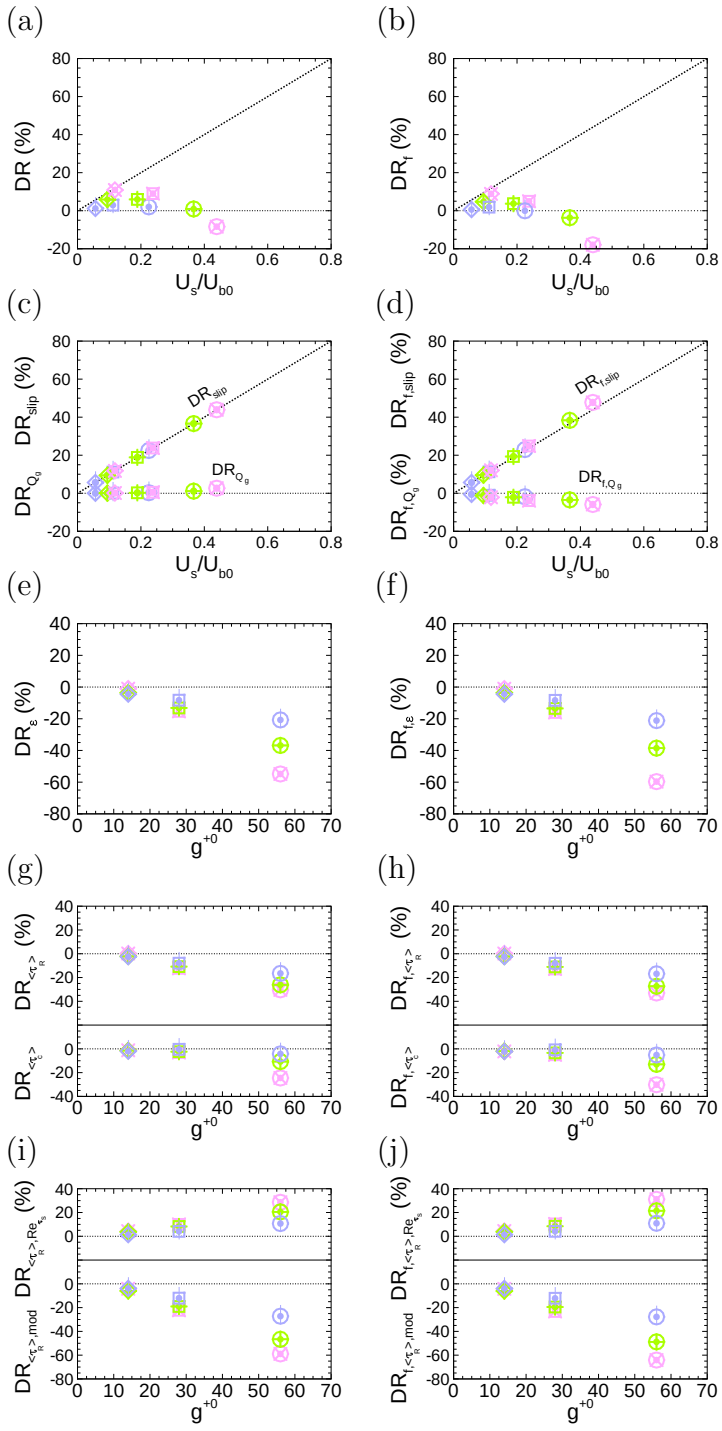

Figure 4.5: Comparison of DR and DR_f in turbulent channel flow with riblets: (a,c,e,g,i) DR; (b,d,f,h,j) DR_f; ◈, ▣, ⊕, $\theta = -30$, $g^{+0} = 14$, 28, 56, respectively; ◈, ▣, ⊕, $\theta = -60$, $g^{+0} = 14$, 28, 56, respectively; ◈, ▣, ⊗, $\theta = -90$, $g^{+0} = 14$, 28, 56, respectively.

area. The effectiveness of micro-textured walls in this metric can be measured by defining a Power Reduction (PR) ratio as

$$PR \equiv \left(1 - \frac{-\langle \frac{\partial \bar{P}}{\partial x} \rangle Q}{-\langle \frac{\partial \bar{P}}{\partial x} \rangle_0 Q}\right) = \left(1 - \frac{-\langle \frac{\partial \bar{P}}{\partial x} \rangle}{-\langle \frac{\partial \bar{P}}{\partial x} \rangle_0}\right). \tag{4.19}$$

Comparison of equations (4.19) and (4.12) shows that PR and DR have identical expressions. Consequently, all the analysis and conclusions reported for DR also applies to PR.

4.3.2 Turbulence Statistics

Figure 4.6 shows profiles of the spanwise-averaged mean streamwise velocity, $\langle \bar{U} \rangle^+ - U_s^+$, turbulence intensities, $\left\{ \langle \bar{u}_i^2 \rangle^{1/2} \right\}^+$, viscous shear stresses, $\langle \tau_v \rangle^+ = \langle \mu \partial \bar{U} / \partial z \rangle^+$, Reynolds shear stresses, $\langle \tau_R \rangle^+ = -\langle \rho \overline{uw} \rangle^+$, mean convective shear stresses, $\langle \tau_c \rangle^+ = -\langle \rho \bar{U} \bar{W} \rangle^+$, and the total shear stresses, $\langle \tau_t \rangle^+ = \langle \tau_v \rangle^+ + \langle \tau_R \rangle^+ + \langle \tau_c \rangle^+$, obtained in DNS of turbulent channel flow with SH LMGs or riblets, compared to the base flow. Here, the superscript + denotes normalization using the kinematic viscosity, ν, and the wall-friction velocity, defined as $u_\tau \equiv \sqrt{-\langle \partial \bar{P} / \partial x \rangle h / \rho}$. The common mechanism of DR with SH LMGs and riblets also leads to common features in the profiles of the spanwise-averaged mean streamwise velocity, turbulence intensities, and shear stresses in the two flows, as seen in figure 4.6.

The presence of wall slip and nonzero Reynolds shear stresses and mean convective shear stresses at the tip of MGs leads to a shortening of the viscous sublayer and the buffer layer and a downward shift of the logarithmic layer in the profiles of the mean velocity, with both SH LMGs and riblets. From Taylor series expansion, the mean streamwise velocity in the near wall region can be expressed as

$$\langle \bar{U}(z) \rangle = U_s + \left\{ \langle \frac{\partial \bar{U}}{\partial z} \rangle |_{z=0} \right\} z + \frac{1}{2} \left\{ \langle \frac{\partial^2 \bar{U}}{\partial z^2} \rangle |_{z=0} \right\} z^2 + O(z^3). \tag{4.20}$$

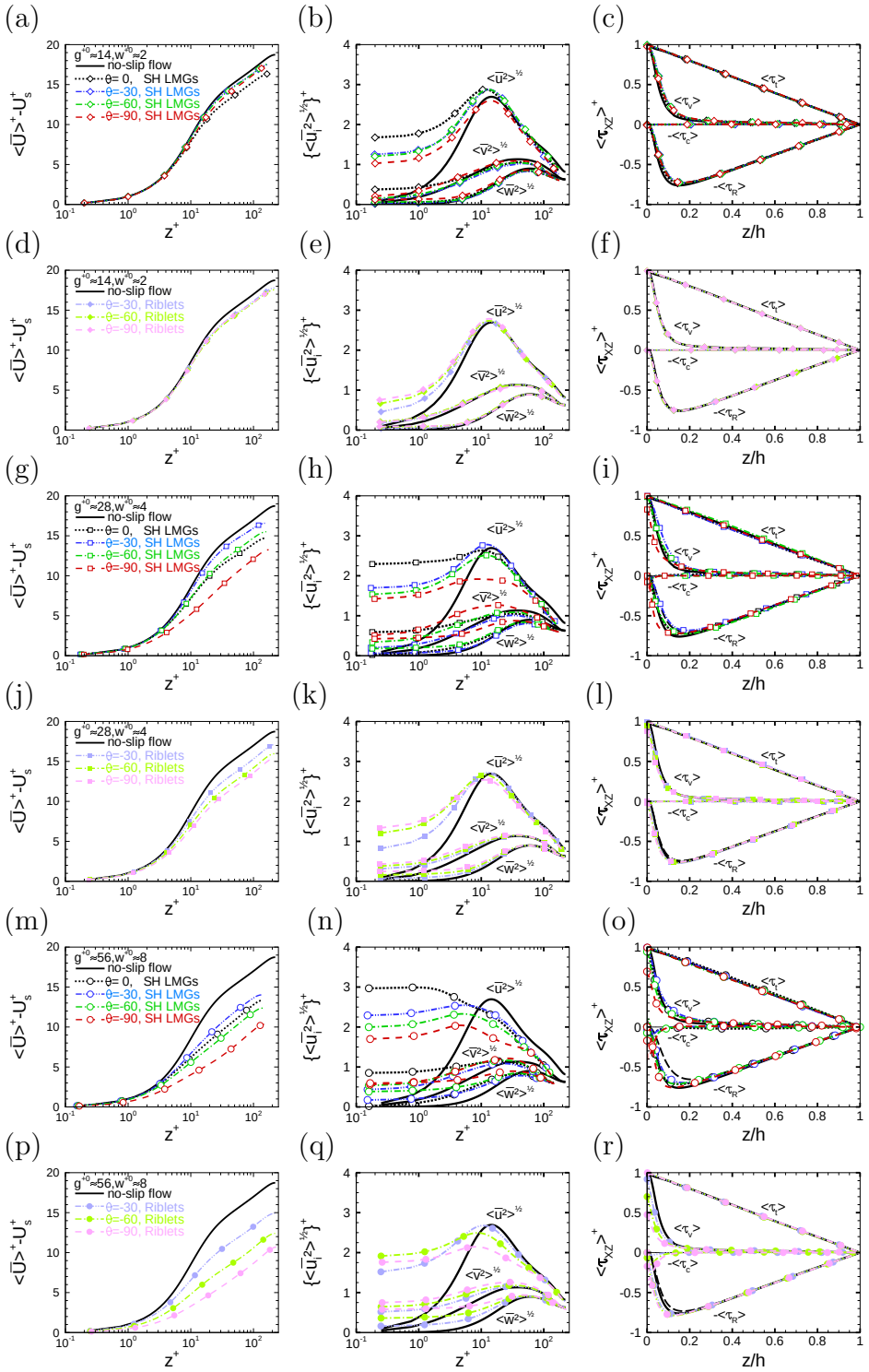

Figure 4.6: Turbulence statistics in turbulent channel flow with SH LMGs or riblets, normalized in wall units: (a,d,g,j,m) mean streamwise velocity subtracted with the slip velocity; (b,e,h,k,n) turbulence intensities; (c,f,i,l,o) Reynolds shear stress, $\langle\tau_R\rangle^+ = -\langle\rho\overline{uw}\rangle^+$, viscous shear stress, $\langle\tau_v\rangle^+ = \langle\mu\partial\bar{U}/\partial z\rangle^+$, mean convective stress, $\langle\tau_c\rangle^+ = -\langle\rho\bar{U}\bar{W}\rangle^+$, and total shrear stress, $\langle\tau_t\rangle^+ = \langle\tau_R\rangle + \langle\tau_v\rangle^+ + \langle\tau_c\rangle^+$; (a-c,g-i,m-o) SH LMGs; (d-f,j-l,p-r) riblets; ---, $\langle\tau_R\rangle^+$ in smooth, no-slip channel flow with Re_τ equal to Re_{τ_s} of SH LMGs or riblets at $\theta = -30^o$.

From equation (4.5), $\nu\langle\partial\bar{U}/\partial z\rangle|_{z=0} = -h/\rho\langle\partial\bar{P}/\partial x\rangle + \langle\overline{uw}\rangle + \langle\bar{U}\bar{W}\rangle$. Thus, equation (4.20) can be written as

$$\begin{aligned}\langle\bar{U}(z^+)\rangle^+ = U_s^+ &+ \left\{1 + \langle\overline{uw}\rangle^+|_{z=0} + \langle\bar{U}\bar{W}\rangle^+|_{z=0}\right\} z^+ \\ &+ O(z^{+^2}).\end{aligned} \tag{4.21}$$

This gives the shape of the mean velocity profile in the viscous sublayer as

$$\begin{aligned}\langle\bar{U}(z^+)\rangle^+ - U_s^+ &= \left\{1 + \langle\overline{uw}\rangle^+|_{z=0} + \langle\bar{U}\bar{W}\rangle^+|_{z=0}\right\} z^+ + O(z^{+^2}) \\ &= \left\{1 - \langle\tau_R\rangle^+|_{z=0} - \langle\tau_c\rangle^+|_{z=0}\right\} z^+ + O(z^{+^2}).\end{aligned} \tag{4.22}$$

Equation (4.22) shows that the presence of nonzero Reynolds and mean convective shear stresses at the tip of MGs leads to a deviation of the mean velocity profile in the viscous sublayer from the linear profile, $\langle\bar{U}(z)\rangle^+ - U_s^+ = z^+$, as seen in figures 4.6(a,d,g,j,m,p).

Furthermore, the presence of wall slip leads to weaker wall-normal gradients in the mean streamwise velocity over the MGs, which when mixed and averaged with the mean streamwise velocities over the MG tips, results in weaker gradients in $\langle\bar{U}\rangle^+$ over the wall, as seen in figures 4.6(c,f,i,l,o,r). This results in a thinning of the buffer layer and a downward shift of the logarithmic layer in the profiles of $\langle\bar{U}\rangle^+ - U_s^+$, with both SH LMGs and riblets, as seen in figures 4.6(a,d,g,j,m,p).

Figure 4.7 shows profiles of the spanwise-averaged mean streamwise velocity, $\langle\bar{U}\rangle^+$, without subtracting the wall slip velocity. Increasing the interface protrusion angle with SH LMGs leads to only negligible changes in the magnitude of slip velocities normalized in wall units, as seen in figures 4.7(a-c). This trend is consistent with the trends in the normalized slip velocities, U_s/U_b, shown in figure 4.2(d). In the logarithmic region, however, increasing the interface protrusion angle leads to a drop in the normalized profiles of $\langle\bar{U}\rangle^+$, as seen in figures 4.7(a-c). This slip velocity is

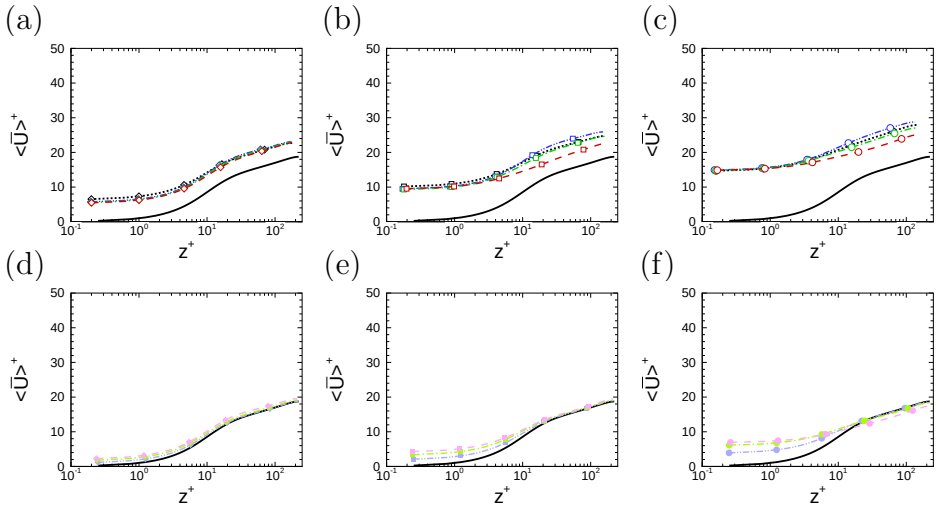

Figure 4.7: Mean streamwise velocity in turbulent channel flow with SH LMGs or riblets, normalized in wall units: (a-f) mean streamwise velocity; (a-c) SH LMGs; (d-f) riblets; Line types as in figure 4.6

retained throughout the domain, leading to an upward shift of the profiles of $\langle \bar{U} \rangle^+$ in the logarithmic layer. In addition, the presence of large non-zero $\langle \tau_c \rangle|_{z=0}$ at large MG widths and large protrusion angles, leads to modifications of not only the viscous sublayer and the shortening of the buffer layer, but also deviations of the mean velocity profile in the logarithmic layer from that in the base channel flow with no-slip walls, as shown in figure 4.7(a-c). With riblets, increasing the MG depth leads to noticeable increases in the magnitude of the slip velocities normalized in wall units, as seen in figures 4.7(d-f). However, the effect of this slip velocity disappears beyond the buffer layer, resulting in mean velocity profiles in the logarithmic layer which are not that different from those in the base flow, except for riblet with large MG widths and depths, where deviations similar to those observed for SH LMGs can be observed, as shown in figure 4.7(d-f).

The presence of surface micro-texture also leads to enhancement of the normalized streamwise, spanwise, and to a lesser extent wall-normal turbulence intensities compared to the base flow, in a surface layer of thickness $\sim g$, as shown in figures 4.6(b,e,h,k,n,q). These enhanced turbulence intensities arise from enhanced produc-

tion of the streamwise turbulence intensities due to the presence of spanwise gradients in the mean streamwise velocity, $\langle \partial \bar{U}/\partial y \rangle^+$, and additional production of streamwise Turbulence Kinetic Energy (TKE) through the $-\langle \overline{uv} \partial \bar{U}/\partial y \rangle^+$ term near the walls, as discussed in section § 4.3.3. This additional production of streamwise TKE is redistributed into the spanwise and wall-normal turbulence intensities through the pressure strain terms, as discussed in section § 4.3.3, giving rise to enhanced turbulence intensities at $z \lesssim g$ for all components of the velocity fluctuations, as shown in figures 4.6(b,e,h,k,n,q). With SH LMGs, increasing the interface protrusion angle leads to a drop in the production of streamwise turbulence intensity, and an increase in the spanwise, and to a lesser extent wall-normal turbulence intensities, compared to flat interfaces, as seen in figures 4.6(b,h,n). With riblets, increasing the MG depths leads to an increase in the production of streamwise turbulence intensity, and an increase in the normalized magnitudes of the spanwise and wall-normal turbulence intensities, compared to flat interfaces, as shown in figures 4.6(e,k,q).

Despite these dramatic changes in the mean velocity profiles and turbulence intensities, the normalized profiles of the Reynolds shear stresses, $\langle \tau_R \rangle^+ = -\langle \overline{uw} \rangle^+$, display only very subtle changes compared to the base flow, as seen in figures 4.6(c,f,i,l,o,r) and figure 4.8. It is these subtle changes which lead to the contributions of $DR_{\langle \tau_R \rangle}$ to DR. Because of the wighting factor $(1 - \chi)$ in the definition of $I_{\langle \tau_R \rangle}$ in equation (4.8) and the small values of $(1 - 3I)$ for SH LMGs and riblets in equation (4.16), a small change in the profiles of $\langle \tau_R \rangle$ in the near-wall region leads to large variations in $DR_{\langle \tau_R \rangle}$. Figures 4.8(a-c) show that SH LMGs of size $g^{+0} \approx 14$ at all protrusion angles, and SH LMGs of size $g^{+0} \gtrsim 28$ at protrusion angles of $\theta = -30^o, -60^o$, which all have an interface depth $d^+ \lesssim 10$, the normalized profiles of $\langle \tau_R \rangle^+$ display a shift towards the center of the channel, thus resulting in drag reducing contributions from $DR_{\langle \tau_R \rangle}$, as seen in figure 4.2(h). For SH LMGs of size $g^{+0} \gtrsim 28$ at protrusion angles of $\theta \approx 90^o$, which all have an interface depth of $d^+ \gtrsim 10$, however, the normalized

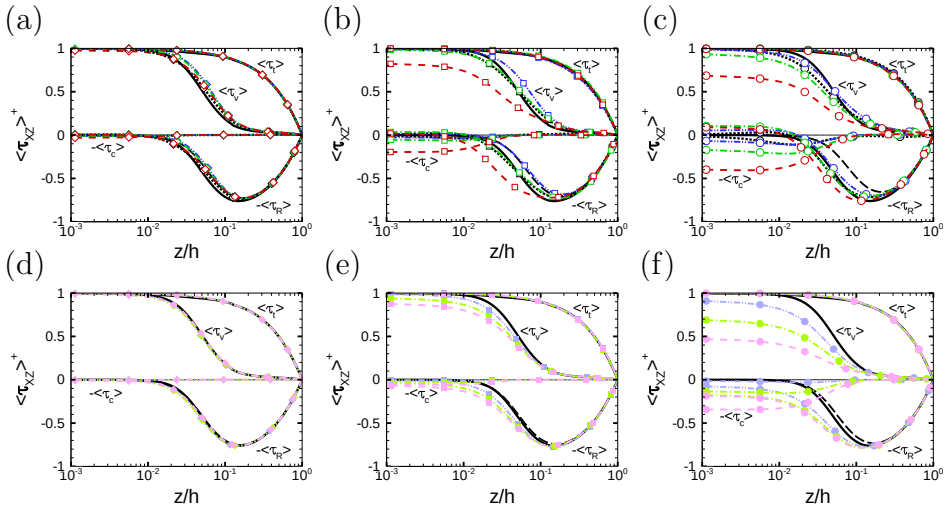

Figure 4.8: Shear stresses in turbulent channel flow with SH LMGs or riblets, normalized in wall units: (a-f) Reynolds shear stress, $\langle\tau_R\rangle^+ = -\langle\rho\overline{uw}\rangle^+$, viscous shear stress, $\langle\tau_v\rangle^+ = \langle\mu\partial\bar{U}/\partial z\rangle^+$, mean convective stress, $\langle\tau_c\rangle^+ = -\langle\rho\bar{U}\bar{W}\rangle^+$, and total shrear stress, $\langle\tau_t\rangle^+ = \langle\tau_R\rangle + \langle\tau_v\rangle^+ + \langle\tau_c\rangle^+$; (a-c) SH LMGs; (d-f) riblets; Line types as in figure 4.6

profiles of $\langle\tau_R\rangle^+$ display a shift towards the wall, as seen in 4.8(b,c), resulting in drag increasing contributions from $DR_{\langle\tau_R\rangle}$, as seen in figure 4.2(h). With riblets, figures 4.8(d-f) show that, for all MG sizes and depths, the normalized profile of $\langle\tau_R\rangle^+$, are shifted towards the wall, compared to the base flow, resulting in drag increasing contributions from $DR_{\langle\tau_R\rangle}$ to the overall DR, as seen in figure 4.2(h). The finding that the contributions from $DR_{\langle\tau_R\rangle}$ are always drag increasing with riblets stands in contrast with all previous theories of the mechanism of DR with riblets, which all attribute DR by riblets to the weakening of turbulence activity (*Bushnell and Hefner*, 1990; *Choi et al.*, 1993; *Bechert et al.*, 1997; *Karniadakis and Choi*, 2003; *García-Mayoral and Jiménez*, 2011).

Figures 4.6(c,f,i,l,o,r) and 4.8 also show the comparison between the normalized profiles of $\langle\tau_R\rangle^+$ with the profiles of $\langle\tau_R\rangle^+$ which would be obtained in a no-slip channel flow at a friction Reynolds number corresponding to Re_{τ_s} of the SH LMGs and riblets at protrusion angle $\theta = -30^o$. The relative position of these profiles

compared to $\langle\tau_R\rangle^+$ of the channels with SH LMGs and riblets is a measure of the contributions of $DR_{\langle\tau_R\rangle,mod}$ to DR. Figures 4.8(a,b) show that for small SH LMGs of size $g^{+0} \approx 14$ at all negative protrusion angles, and for SH LMGs of size $g^{+0} \approx 28$ at small negates protrusion angles, $\theta = -30^o$, the normalized profiles of $\langle\tau_R\rangle^+$ display a shift towards the center of the channel, compared to the profiles of $\langle\tau_R\rangle^+$ obtained in a no-slip channel flow at the friction Reynolds number Re_{τ_s}. This implies drag reducing contributions from $DR_{\langle\tau_R\rangle,mod}$, as seen in figure 4.2(i). With SH LMGs of size $g^{+0} \approx 28$ at medium and large protrusion angles, $\theta = -30^o, -60^o$, and large SH LMGs of size $g^{+0} \approx 56$ at all protrusion angles, however, the shift in the profiles of $\langle\tau_R\rangle^+$ is towards the wall. In this case, the shift leads to drag increasing contributions from $DR_{\langle\tau_R\rangle}$, as seen in figure 4.2(i). With riblets of all size and MG depth, also, there is a shift in the profiles of $\langle\tau_R\rangle^+$ is towards the wall, as seen in figures 4.8(d-f), resulting in drag increasing contributions from $DR_{\langle\tau_R\rangle,mod}$, shown in figure 4.2(i).

4.3.3 Turbulence Kinetic Energy Budget

In statistically stationary turbulence, the equation for TKE budget in the α direction is given by (*Hinze*, 1975)

$$\frac{D}{Dt}\frac{\overline{u_\alpha u_\alpha}}{2} = P_{\alpha\alpha} - \varepsilon_{\alpha\alpha} + t^{(\Sigma)}_{\alpha\alpha} + \Pi_{\alpha\alpha}, \tag{4.23}$$

where,

$$
\begin{aligned}
P_{\alpha\alpha} &= -\overline{u_\alpha u_\gamma}\frac{\partial \bar{U}_\alpha}{\partial x_\gamma}, \\
\varepsilon_{\alpha\alpha} &= 2\nu\overline{s_{\alpha\gamma}\frac{\partial u_\alpha}{\partial x_\gamma}}, \\
t^{(\Sigma)}_{\alpha\alpha} &= t^{(R)}_{\alpha\alpha} + t^{(press)}_{\alpha\alpha} + t^{(v)}_{\alpha\alpha} \\
&= -\frac{1}{2}\frac{\partial}{\partial x_\gamma}\overline{u_\alpha u_\alpha u_\gamma} - \frac{1}{\rho}\frac{\partial}{\partial x_\alpha}\overline{p u_\alpha} + 2\nu\frac{\partial}{\partial x_\gamma}\overline{u_\alpha s_{\alpha\gamma}}, \\
\Pi_{\alpha\alpha} &= \frac{1}{\rho}\overline{p\frac{\partial u_\alpha}{\partial x_\alpha}}.
\end{aligned}
$$

and no summation is implied over α index. Here, $P_{\alpha\alpha}$ is the rate of TKE production per unit mass, $\varepsilon_{\alpha\alpha}$ is the rate of viscous dissipation, $t^{(R)}_{\alpha\alpha}$, $t^{(press)}_{\alpha\alpha}$, and $t^{(v)}_{\alpha\alpha}$ are the rates of TKE transport by turbulent fluctuations, pressure fluctuations and viscous stresses, respectively, $t^{(\Sigma)}_{\alpha\alpha}$ is the total transport, $\Pi_{\alpha\alpha}$ is the pressure-strain correlation, and $s_{\alpha\gamma} = 1/2(\partial u_\alpha/\partial x_\gamma + \partial u_\gamma/\partial x_\alpha)$ is the fluctuating strain-rate tensor.

Summation of equation (3.8) over all three α directions results in the TKE balance equation, given by (*Hinze*, 1975)

$$
\frac{D}{Dt}\overline{k^2} = P_{ii} - \varepsilon_{ii} + t^{(\Sigma)}_{ii}, \tag{4.24}
$$

where $\overline{k^2} = \overline{u_i^2}/2$ is the turbulence kinetic energy per units mass, and the pressure-strain term is eliminated because $\Pi_{ii} = 0$.

Figures 4.9, 4.10 and 4.11 show the profiles of the terms in the spanwise-averaged equations for the components of TKE, normalized in wall units, for SH LMGs and riblets of size $g^{+0} \approx 14$ & $w^{+0} \approx 2$, $g^{+0} \approx 28$ & $w^{+0} \approx 4$ and $g^{+0} \approx 56$ & $w^{+0} \approx 8$, respectively. With both the SH LMGs and riblets, production of turbulence mainly occurs through the streamwise TKE, $\langle P_{uu}\rangle^+$. Although some minor negative contributions arising from the spanwise and wall-normal TKE production, $\langle P_{uu}\rangle^+$ and $\langle P_{uu}\rangle^+$, respectively, are also present, as seen in figures 4.9(a-c), 4.10(a-c) and 4.11(a-

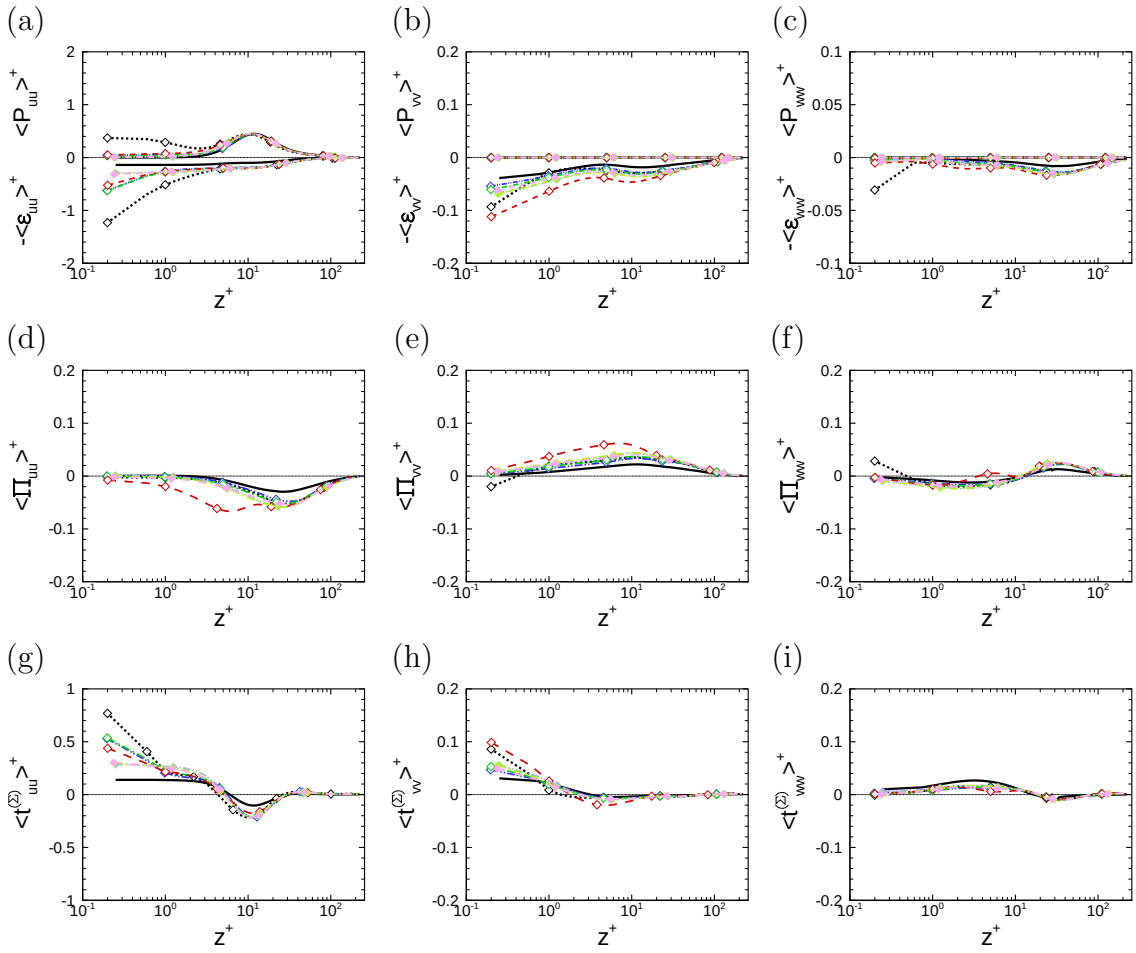

Figure 4.9: Breakdown of the TKE budget in turbulent channel flow with SH LMGs or riblets of size $g^{+0} \approx 14$ & $w^{+0} \approx 2$, normalized in wall units: (a-c) production, $\langle P_{\alpha\alpha} \rangle^+$, and dissipation, $\langle \varepsilon_{\alpha\alpha} \rangle^+$ of TKE; (d-f) pressure strain correlation, $\langle \Pi_{\alpha\alpha} \rangle^+$; (g-i) total transport of TKE, $\langle t^{(\Sigma)}_{\alpha\alpha} \rangle^+$; Line types as in figure 4.6.

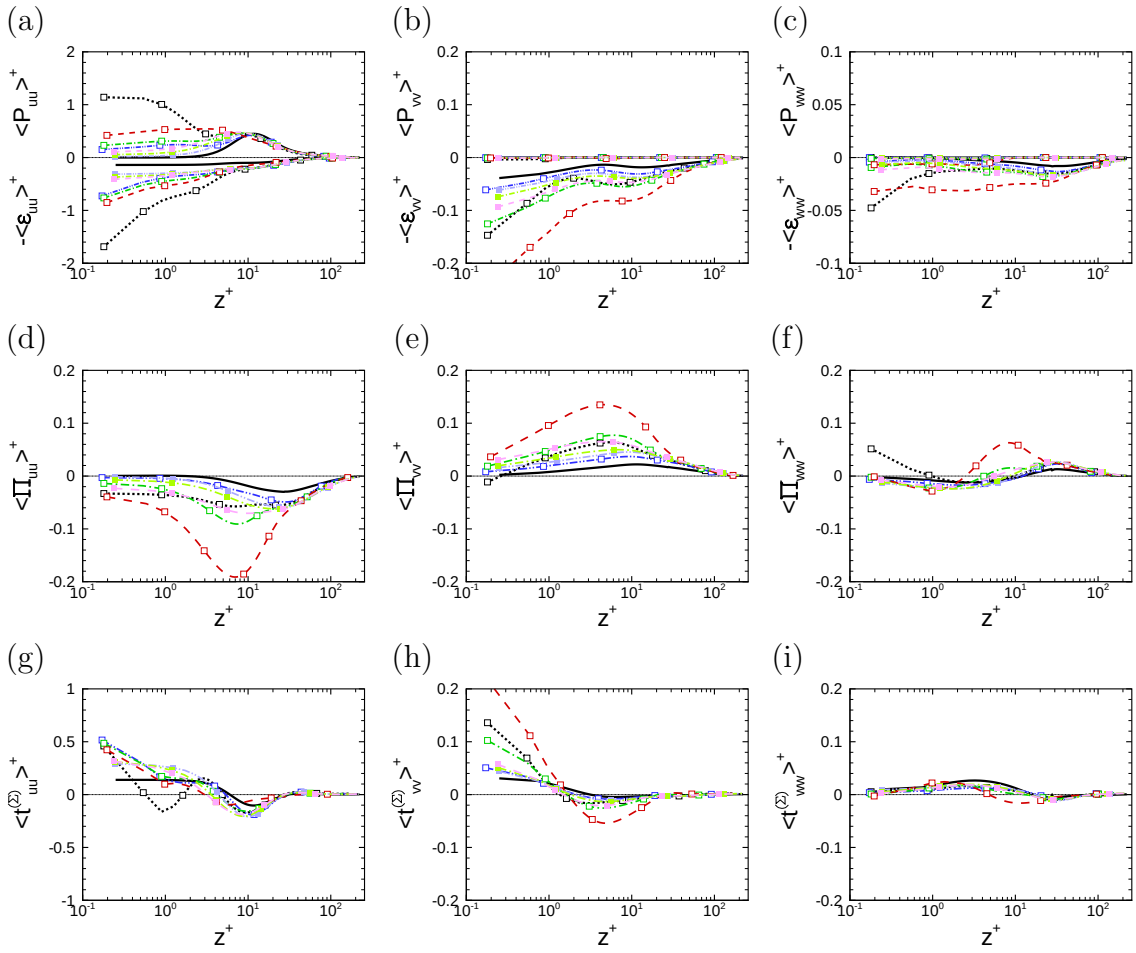

Figure 4.10: Breakdown of the TKE budget in turbulent channel flow with SH LMGs or riblets of size $g^{+0} \approx 28$ & $w^{+0} \approx 4$, normalized in wall units: (a-c) production, $\langle P_{\alpha\alpha} \rangle^+$, and dissipation, $\langle \varepsilon_{\alpha\alpha} \rangle^+$ of TKE; (d-f) pressure strain correlation, $\langle \Pi_{\alpha\alpha} \rangle^+$; (g-i) total transport of TKE, $\langle t^{(\Sigma)}_{\alpha\alpha} \rangle^+$; Line types as in figure 4.6.

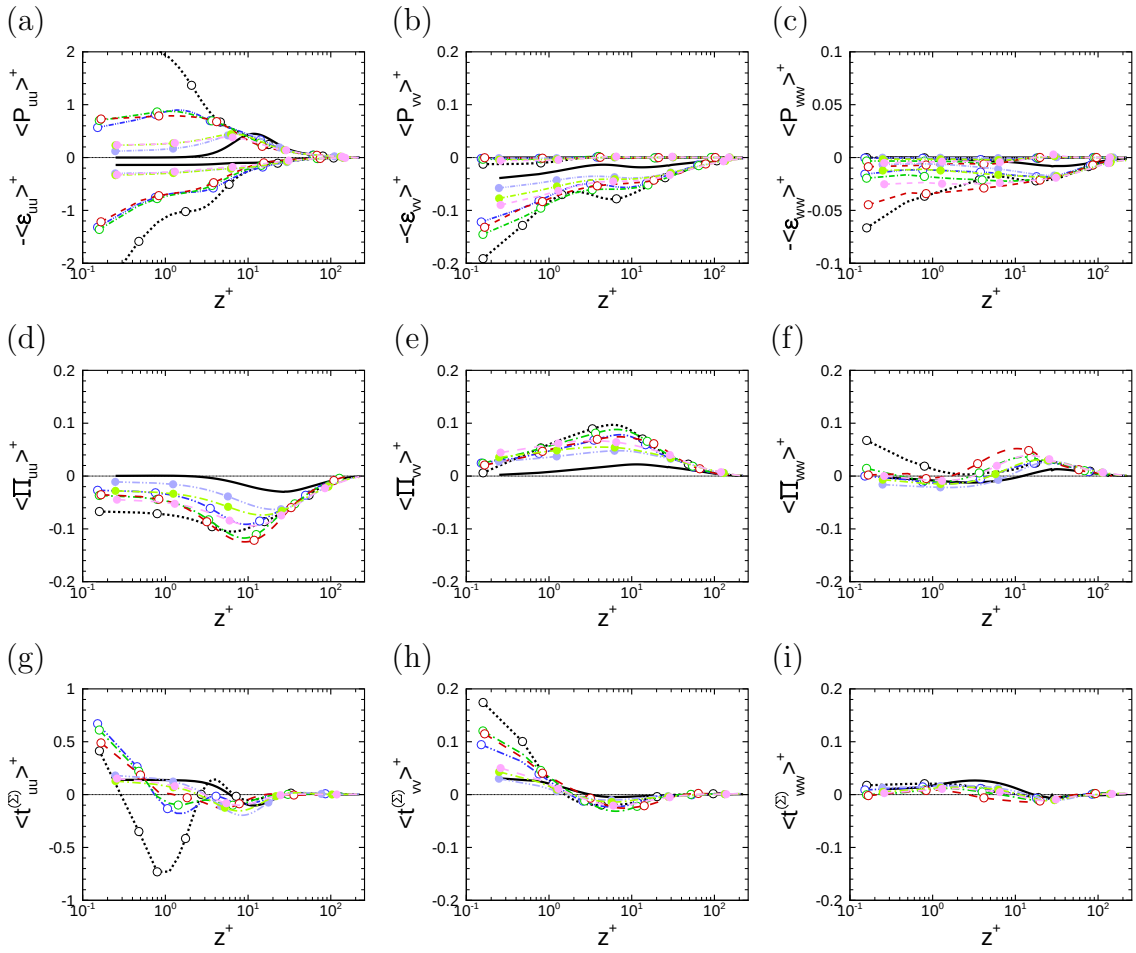

Figure 4.11: Breakdown of the TKE budget in turbulent channel flow with SH LMGs or riblets of size $g^{+0} \approx 56$ & $w^{+0} \approx 8$, normalized in wall units: (a-c) production, $\langle P_{\alpha\alpha} \rangle^+$, and dissipation, $\langle \varepsilon_{\alpha\alpha} \rangle^+$ of TKE; (d-f) pressure strain correlation, $\langle \Pi_{\alpha\alpha} \rangle^+$; (g-i) total transport of TKE, $\langle t^{(\Sigma)}_{\alpha\alpha} \rangle^+$; Line types as in figure 4.6.

c). With both SH LMGs and riblets, the presence of effective slip at the walls leads to the formation of spanwise gradients in the mean streamwise velocity, $\langle \partial \bar{U}/\partial y \rangle$, which gives rise to additional production of $\langle P_{uu} \rangle^+$ through $-\langle \overline{uv} \partial \bar{U}/\partial y \rangle^+$ within a 'surface layer' of thickness $z \sim g$. For both SH LMGs and riblets, the magnitude of this additional contribution to $\langle P_{uu} \rangle^+$ increases with increasing MG width. However, due to the higher wall slip velocities, with SH LMGs, the magnitude of the additional TKE production through $-\langle \overline{uv} \partial \bar{U}/\partial y \rangle$ is always larger with SH LMGs, by factors of up to ~ 10, compared to riblets. For a given MG width, increasing the interface protrusion angle from $\theta = -30^o$ to $\theta = -90^o$ with SH LMGs, or increasing the MG depth from $d/g = 1/7$ ($\theta = 30^o$) to $d/g = 1/2$ ($\theta = 90^o$) with riblets, leads to an increase in the magnitudes of $\langle P_{uu} \rangle^+$ production through $-\langle \overline{uv} \partial \bar{U}/\partial y \rangle^+$, within the 'surface layer', compared to the base flow, as seen in figures 4.9(a), 4.10(a) and 4.11(a). However, the magnitude of this additional production of $\langle P_{uu} \rangle^+$ never reaches those obtained with flat SH LMGs.

Along with the changes in $\langle P_{uu} \rangle^+$ production, increasing the MG widths with both SH LMGs and riblets leads to an increase in the normalized magnitudes of the pressure strain terms, $\langle \Pi_{\alpha\alpha} \rangle^+$, which transfer parts of $\langle P_{uu} \rangle^+$ to the spanwise and wall-normal TKEs, as seen in figures 4.9(d-f), 4.10(d-f) and 4.11(d-f). Increasing the interface protrusion angle from $\theta = -30^o$ to $\theta = -90^o$ with SH LMGs, or increasing the MG depth from $d/g = 1/7$ ($\theta = 30^o$) to $d/g = 1/2$ ($\theta = 90^o$) with riblets, leads to an increase in the normalized magnitudes of $\langle \Pi_{ii} \rangle^+$ terms, compared to the base flow, as seen in figures 4.9(d-f), 4.10(d-f) and 4.11(d-f). When compared to $\langle P_{uu} \rangle^+$ production, however, the relative magnitudes of $\langle \Pi_{uu} \rangle^+$ terms with SH LMGs are much larger than those with either riblets or SH LMGs with flat interfaces. This results in streamwise turbulence intensities which display two different trends with SH LMGs and riblets. Increasing the interface protrusion angle, from $\theta = -30^o$ to $\theta = -90^o$, with SH LMGs leads to a gradual decrease in the normalized magnitudes

of streamwise turbulence intensities, within the 'surface layer', while increasing the MG depth with riblets, from $d/g = 1/7$ ($\theta = -30^o$) to $d/g = 1/2$ ($\theta = -90^o$), leads to an increase in the normalized magnitudes of streamwise turbulence intensities, within the 'surface layer', as seen in figures 4.6(b,h,n). Furthermore, turbulence intensities obtained with SH LMGs, with flat interfaces in the 'surface layer' were always significantly larger than those obtained with curved SH interfaces.

Figure 4.12 shows profiles of the spanwise-averaged balance of total TKE, normalized in wall units. With both the SH LMGs and riblets, TKE production occurs mainly through the spanwise and wall-normal gradients in the mean streamwise velocity, $\langle \partial \bar{U}/\partial y \rangle$, and $\langle \partial \bar{U}/\partial z \rangle$, respectively. The TKE production through $-\langle \overline{uw} \partial \bar{U}/\partial z \rangle$ displays a shift of the peak of production towards the walls, with both the SH LMGs and riblets, and negative production with SH LMGs for $z^+ \lesssim 2$, the magnitudes of which increases with increasing MG width and protrusion angle. In addition, the presence of spanwise gradients in the mean streamwise velocity, $-\langle \overline{uv} \partial \bar{U}/\partial y \rangle$, leads to enhanced production of TKE, $\langle P \rangle^+$, within the 'surface layer', as seen in figures 4.12(b,e,h,k,n,q). When the above tow contributions are added together, the resulting total TKE displays an increase, near the walls, within the 'surface layer', together with a shift in the location of its local maximum, towards the wall, as seen in figures 4.12(a,d,g,j,m,p).

4.3.4 Vorticity Dynamics

Figure 4.13 shows the profiles of spanwise-averaged root-mean-square (rms) vorticity fluctuations, $\left\{ \langle \overline{\omega_i^2} \rangle^{1/2} \right\}^+$, normalized in wall units, in channel flows with SH LMGs or riblets, compared to the base flow. For riblets of any size and SH LMGs of size $g^+ \gtrsim 20$, where the contributions from $DR_{\langle \tau_R \rangle, mod}$ are drag increasing ($DR_{\langle \tau_R \rangle, mod} < 0$), the normalized profiles of $\left\{ \langle \overline{\omega_x^2} \rangle^{1/2} \right\}^+$ fall above that in the base flow, as seen in figures 4.13(a,g,m), indicating an enhancement of turbulence activity due to the

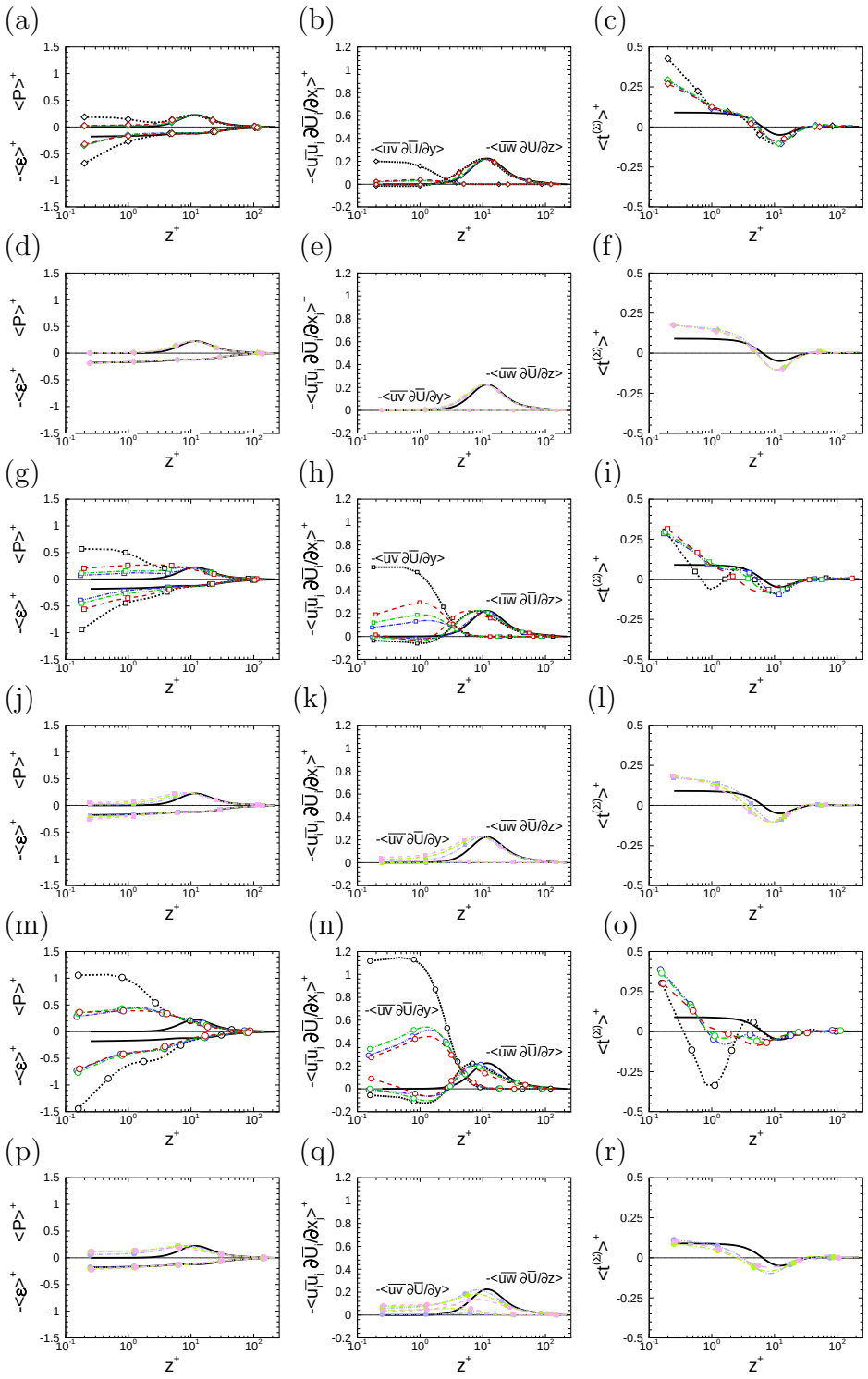

Figure 4.12: TKE budget in turbulent channel flow with SH LMGs or riblets, normalized in wall units: (a,d,g,j,m,p) production $\langle P\rangle^+$, and dissipation $\langle\varepsilon\rangle^+$ of TKE; (b,e,h,k,n,q) breakdown of TKE production into $-\langle\overline{uw}\partial\bar{U}/\partial z\rangle^+$ and $-\langle\overline{uv}\partial\bar{U}/\partial y\rangle^+$; (c,f,l,i,o,r) total transport of TKE; (a-c,g-i,m-o) SH LMGs; (d-f,j-l,p-r) riblets; Line types as in figure 4.6.

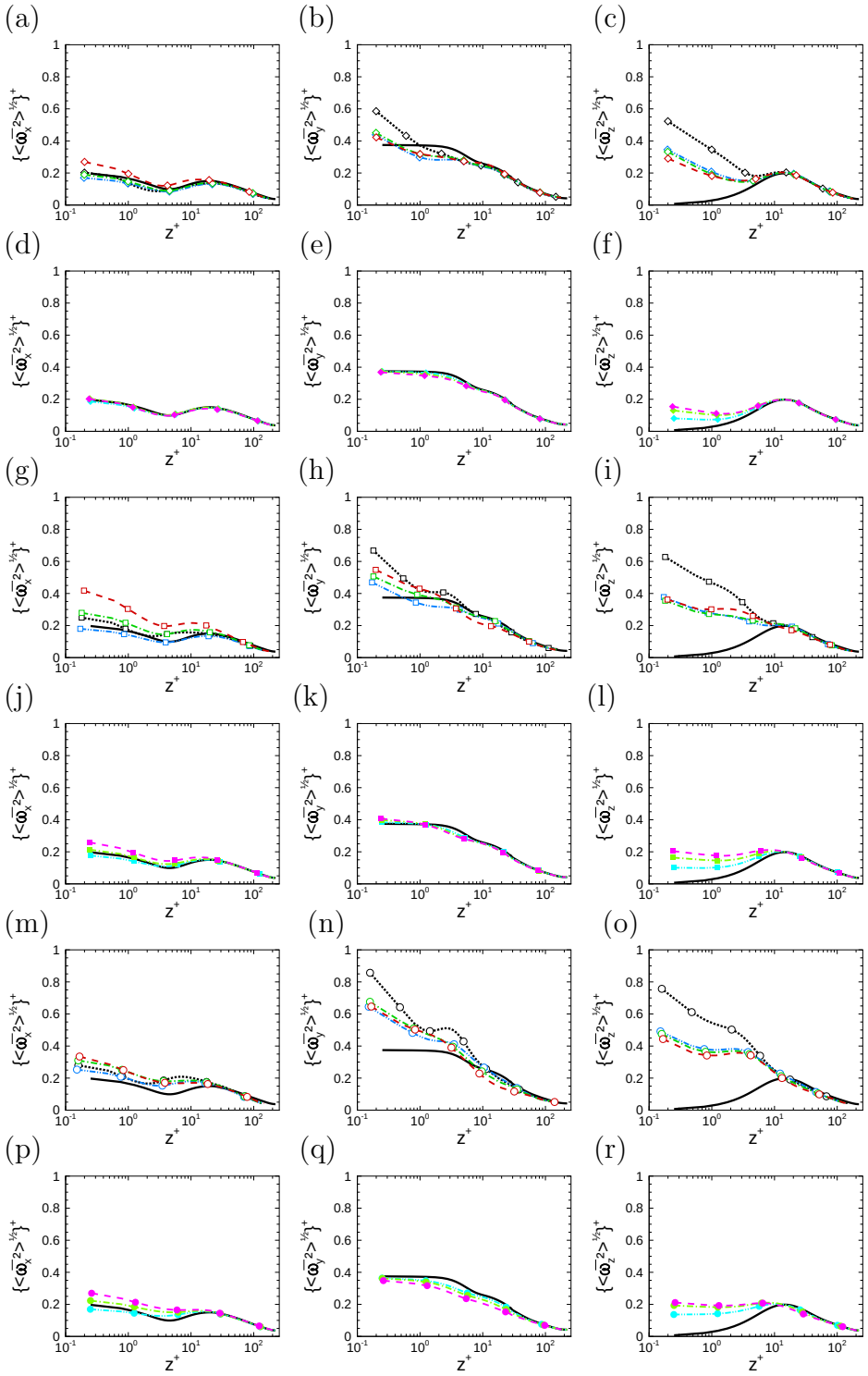

Figure 4.13: rms vorticity fluctuations in turbulent channel flow with SH LMGs or riblets, normalized in wall units: (a,d,g,j,m,p) streamwise vorticity fluctuations; (b,e,h,k,n,q) spanwise vorticity fluctuations; (c,f,i,l,o,r) wall-normal vorticity fluctuations; (a,b,c,g,h,i,m,n,o) SH LMGs; (d,e,f,j,k,l,p,q,r) riblets; line types as in figure 4.6.

presence of wall micro-texture. For SH LMGs of size $g^+ \lesssim 20$, where the contributions from $DR_{\langle\tau_R\rangle,mod}$ are drag reducing ($DR_{\langle\tau_R\rangle,mod} > 0$), the normalized profiles of $\left\{\langle\overline{\omega_x^2}\rangle^{1/2}\right\}^+$ fall bellow that in the base flow, indicating a suppression of turbulence activity due to the presence of the wall micro-texture. In addition, with SH LMGs, effective slip at the wall leads to an increase in the normalized magnitudes of spanwise-averaged spanwise vorticity fluctuations, $\left\{\langle\overline{\omega_y^2}\rangle^{1/2}\right\}^+$, within the 'surface layer', compared to the base flow, as seen in figures 4.13(b,h,n). This effect increases as the interface protrusion angle is increases from $\theta = -30^o$ to -90^o. However, the enhancements never become as large as those observed with flat SH interfaces. With riblets, increasing MG depth, from $d/g = 1/7$ ($\theta = -30^o$) to $d/g = 1/2$ ($\theta = -90^o$), leads to a drop in the normalized magnitudes of $\left\{\langle\overline{\omega_y^2}\rangle^{1/2}\right\}^+$ within the 'surface layer', compared to no-slip channel flows, as seen in figures 4.13(e,k,q). Furthermore, with both SH LMGs and riblets, the formation of a shear layer, $\partial u/\partial y$, between the low and high speed regions on top of the wall MGs, leads to an increase in the normalized magnitudes of the wall-normal vorticity fluctuations, $\left\{\langle\overline{\omega_z^2}\rangle^{1/2}\right\}^+$, within the 'surface layer', compared to the base flow, as seen in figures 4.13(c,f,i,l,o,r). Due to the much smaller magnitudes of the slip velocities with riblets, this increase in $\left\{\langle\overline{\omega_z^2}\rangle^{1/2}\right\}^+$ is less prominent with riblets. With SH LMGs, these shear layer are weakened with increasing interface deformation. Hence, for a given MG size, increasing the interface protrusion angle, from $\theta = -30^o$ to -90^o, with SH LMGs, leads to a drop in the magnitudes of $\left\{\langle\overline{\omega_z^2}\rangle^{1/2}\right\}^+$, within the 'surface layer', as seen in figures 4.13(c,i,o). With riblets, however, increasing the MG depths, from $d/g = 1/7$ ($\theta = -30^o$) to $d/g = 1/2$ ($\theta = -90^o$), strengthens the shear layers, leading to an increase in the normalized magnitudes of $\left\{\langle\overline{\omega_z^2}\rangle^{1/2}\right\}^+$, within the 'surface layer', as seen in figures 4.13(f,l,r).

In general, the near wall regions of turbulent boundary layers are dominated by a set of quasi-streamwise vortices (*Jimenez*, 1994). The effective slip at the walls alters dynamics of these near-wall streamwise vortical structures, within the 'surface

layer', through the combination of two competing effects: (i) a weakening effect resulting from the drop in wall-normal gradients of the streamwise velocity, and (ii) a strengthening effect due to establishment of spanwise wall slip. The former effect dominates for SH LMGs of size $g^+ \lesssim 20$, resulting in drag reducing contributions arising from $DR_{\langle\tau_R\rangle,mod}$ and near-wall streamwise vorticity fluctuations which are weaker than the base flow, while the latter dominates for SH LMGs of size $g^+ \gtrsim 20$ and riblets, resulting in drag increasing contributions arising from $DR_{\langle\tau_R\rangle,mod}$ and near-wall streamwise vorticity fluctuations which are stronger than the base flow, as shown in figure 4.13(a,d,g,j,m,p).

4.3.5 Pressure Fluctuations

Figure 4.14 shows profiles of the spanwise-averaged rms pressure fluctuations, $\left\{\langle\bar{p^2}\rangle^{1/2}\right\}^+$, normalized in wall units. The trends in the normalized profiles of the spanwise-averaged streamwise vorticity fluctuations, $\left\{\langle\overline{\omega_x^2}\rangle^{1/2}\right\}^+$, are also reflected in the normalized profiles of $\left\{\langle\bar{p^2}\rangle^{1/2}\right\}^+$, as seen in figures 4.14 and 4.13(a,d,g,j,m,p). With SH LMGs, increasing the MG sizes leads to an increase in the normalized magnitudes of $\left\{\langle\bar{p^2}\rangle^{1/2}\right\}^+$, within the 'surface layer', as seen in figure 4.14(a-c). For a given MG size, at small protrusion angles, $\theta \sim -30$, the presence of interface curvature with SH LMGs leads to drops of $\sim$ 12% to 26% in the normalized magnitude of $\left\{\langle\bar{p^2}\rangle^{1/2}\right\}^+$, within the 'surface layer', compared to flat interfaces. Larger protrusion angle, beyond $\theta = -30^o$, however, lead to an increase in the normalized magnitudes of $\left\{\langle\bar{p^2}\rangle^{1/2}\right\}^+$, within the 'surface layer', as seen in figures 4.14(a-c).

The magnitude of the pressure fluctuations at the wall directly affects the stability of the liquid/gas interfaces on SH surfaces. The smaller the pressure forces, the more stable the liquid/gas interfaces. Figures 4.14(a-c) and table 4.3 show that the lowest $\left\{\langle\bar{p^2}\rangle^{1/2}\right\}^+$ on the SH wall are obtained at small MG sizes, $g^{+0} \approx 14$, and small interface protrusion angles, $\theta \approx -30$. At this MG sizes, significant drops, of up

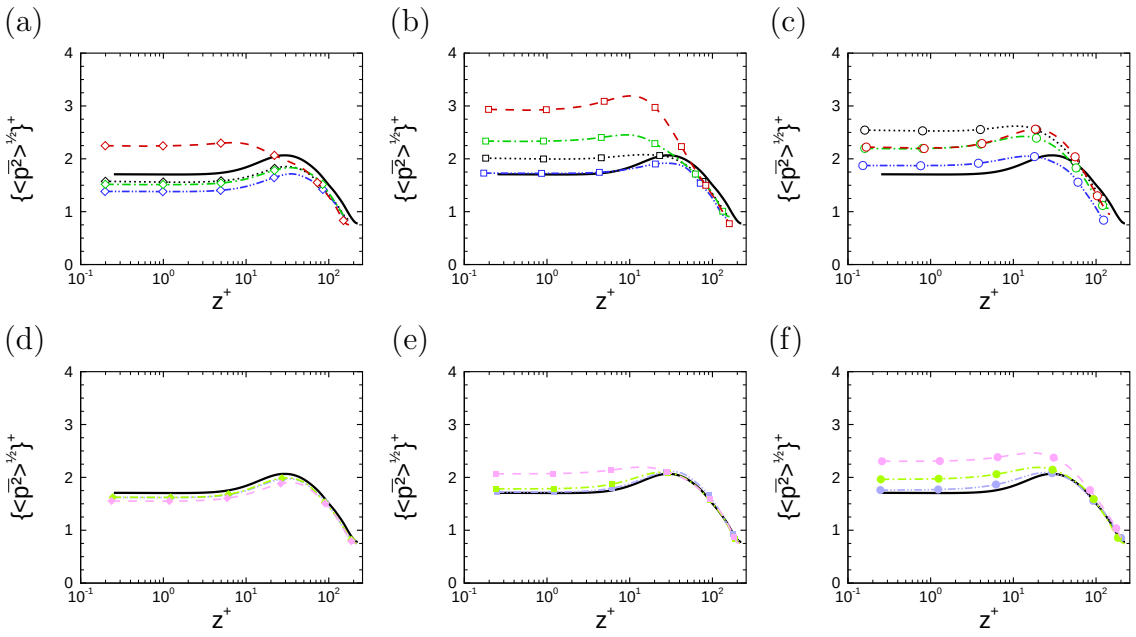

Figure 4.14: Spanwise-averaged rms pressure fluctuations in turbulent channel flow with SH LMGs and riblet, normalized in wall units: (a,b,c) $\left\{\langle\bar{p^2}\rangle^{1/2}\right\}^+$, SH LMGs; (d,e,f) $\left\{\langle\bar{p^2}\rangle^{1/2}\right\}^+$, riblets; Line types as in figure 4.6.

to a factor of ~ 2, are also observed in the instantaneous magnitudes of pressure fluctuations, p^+, as seen in figures 4.15(a-d). With larger MG widths, $g^{+0} \gtrsim 28$, however, the drop in $\left\{\langle\bar{p^2}\rangle^{1/2}\right\}^+$ and p^+ at small protrusion angles is smaller, and less pronounced, as seen in figures 4.14(b) and 4.16(a-d) and table 4.3.

With riblets of small MG sizes, $g^{+0} \approx 14$, increasing the riblet depth from $d/g = 1/7$ to $d/g = 1/2$ give rise to small drops of up to 4% in the normalized magnitudes of

g^{+0}	14	14	14	14	28	28	28	28	56	56	56	56
w^{+0}	2	2	2	2	4	4	4	4	8	8	8	8
θ	0°	-30°	-60°	-90°	0°	-30°	-60°	-90°	0°	-30°	-60°	-90°
SH LMGs $\left\{\langle\bar{p^2}\rangle^{1/2}\right\}^+\|_{z=0}$	1.57	1.38	1.52	2.25	2.01	1.73	2.33	2.93	2.54	1.87	2.19	2.22
Riblets $\left\{\langle\bar{p^2}\rangle^{1/2}\right\}^+\|_{z=0}$	-	1.62	1.62	1.55	-	1.72	1.78	2.07	-	1.76	1.96	2.29

Table 4.3: Spanwise-averaged magnitudes of r.m.s. pressure fluctuations at the tip of MGs, $\left\{\langle\bar{p^2}\rangle^{1/2}\right\}^+|_{z=0}$, in turbulent channel flow with SH LMGs and riblets, normalized in wall units.

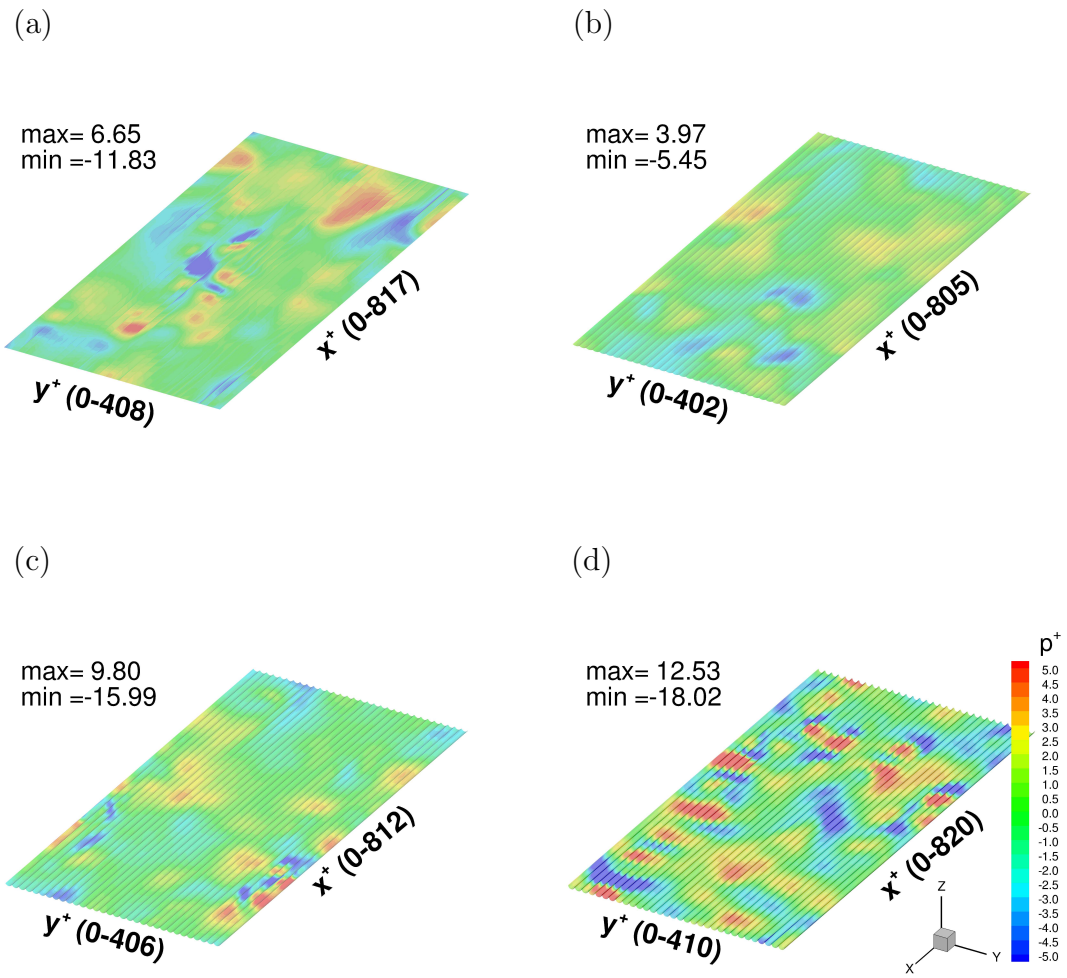

Figure 4.15: Contour plots of instantaneous pressure fluctuations in turbulent channel flow with SH LMGs of size $g^{+0} \approx 14$ & $w^{+0} \approx 2$, normalized in wall units: (a) $\theta = 0^o$; (b) $\theta = -30^o$; (c) $\theta = -60^o$; (d) $\theta = -90^o$.

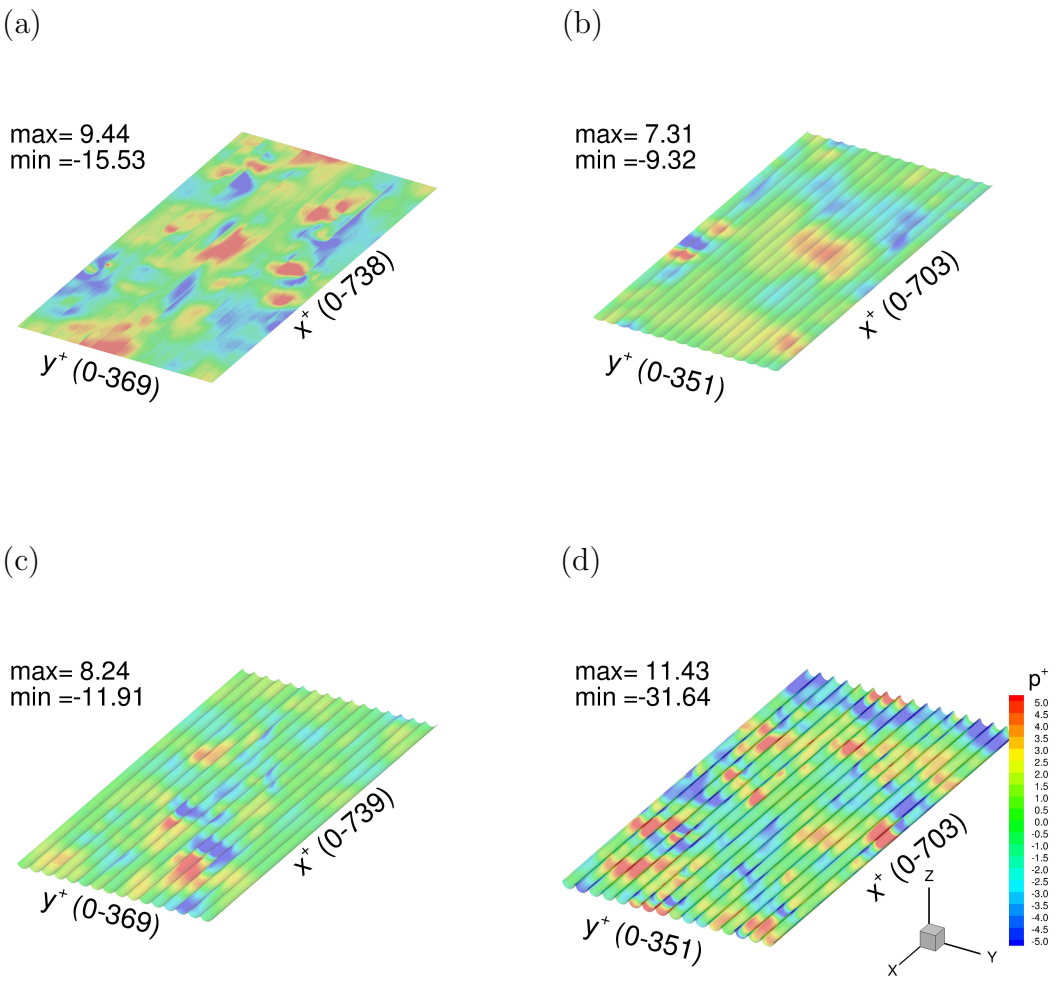

Figure 4.16: Contour plots of instantaneous pressure fluctuations in turbulent channel flow with SH LMGs of size $g^{+0} \approx 28$ & $w^{+0} \approx 4$, normalized in wall units: (a) $\theta = 0^o$; (b) $\theta = -30^o$; (c) $\theta = -60^o$; (d) $\theta = -90^o$.

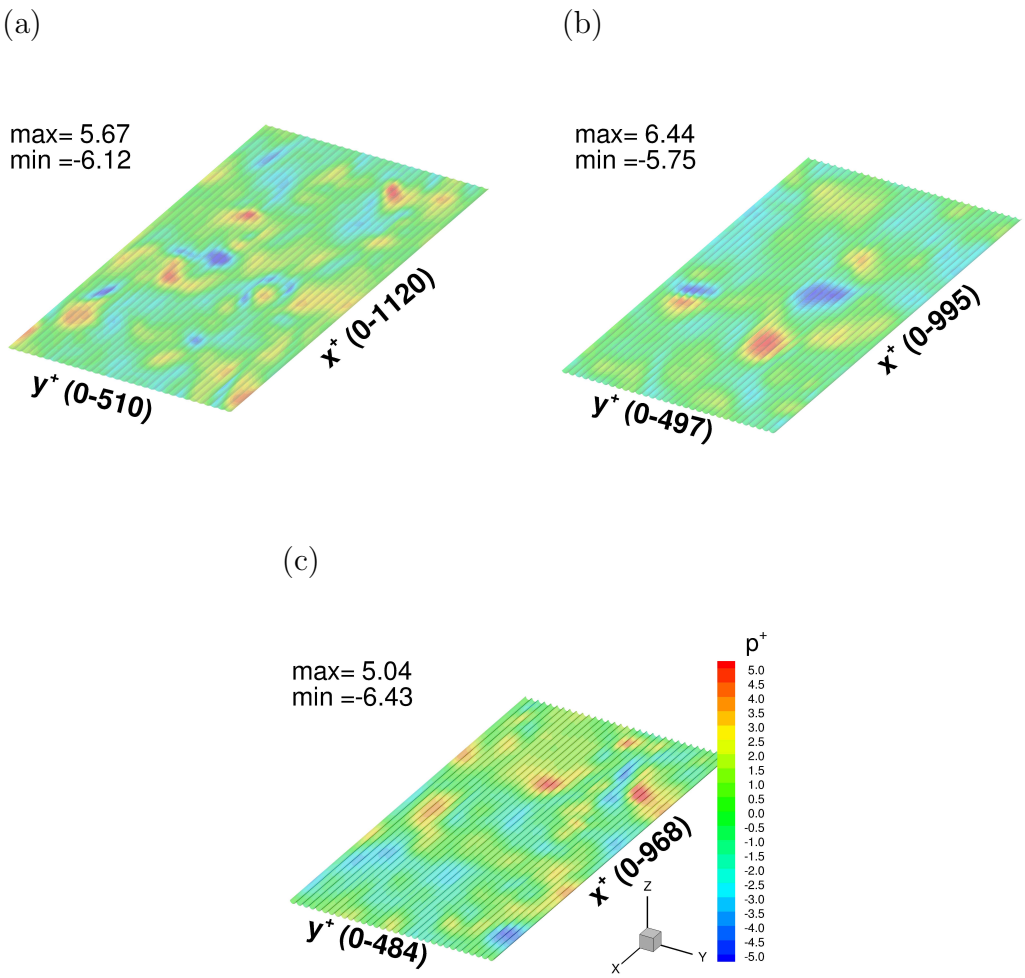

Figure 4.17: Contour plots of instantaneous pressure fluctuations in turbulent channel flow with riblets of size $g^{+0} \approx 14$ & $w^{+0} \approx 2$, normalized in wall units: (a) $d/g = 1/7$ ($\theta = -30^o$); (b) $d/g = 2/7$ ($\theta = -60^o$); (c) $d/g = 1/2$ ($\theta = -90^o$).

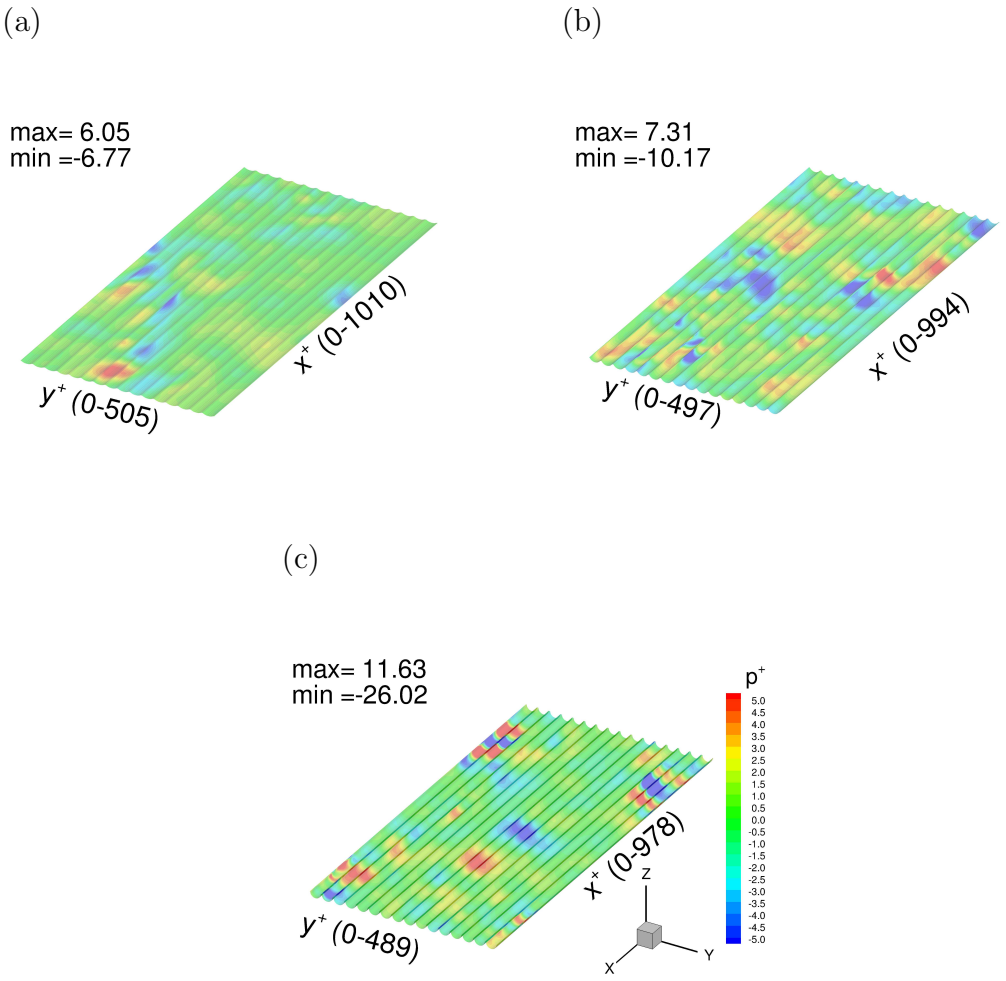

Figure 4.18: Contour plots of instantaneous pressure fluctuations in turbulent channel flow with riblets of size $g^{+0} \approx 28$ & $w^{+0} \approx 4$, normalized in wall units: (a) $d/g = 1/7$ ($\theta = -30^o$); (b) $d/g = 2/7$ ($\theta = -60^o$); (c) $d/g = 1/2$ ($\theta = -90^o$)..

$\left\{\langle\bar{p^2}\rangle^{1/2}\right\}^+$, within the 'surface layer', as seen in figure 4.14(d). With riblets of larger MG sizes, however, increasing the riblet depth leads to an increase in the normalized magnitudes of $\left\{\langle\bar{p^2}\rangle^{1/2}\right\}^+$, within the 'surface layer', as seen in figures 4.14(e-f). The smallest instantaneous pressure fluctuations with riblets are obtained at $g^{+0} \approx 14$ and $d/g = 1/7$ ($\theta = 30^o$), similar to SH LMGs, as shown in figures 4.17 and 4.18.

These features suggest that the durability and robustness of SH surfaces can be improved by embedding the SH surface inside scallop-shaped riblets of size $g^{+0} \approx 14$ and $d/g = 1/7$ ($\theta = 30^o$). Figures 4.15, 4.16, 4.17 and 4.18 show that, with both SH LMGs and riblets, the lowest instantaneous magnitudes of p^+ are observed with MGs of size $g^{+0} \approx 14$ at a MG depth of $d/g = 1/7$ ($\theta = -30^o$) with riblets and interface protrusion angle $\theta \approx -30^o$, with SH LMGs. With lower p^+, the liquid/gas interfaces on the SH surface are more stable. By designing a hierarchical SH surface, in which a set of SH LMGs of size are placed inside shallow ($\theta = -30^o$) scallop shaped riblets of width $g^{+0} \approx 14$, these features can be utilized to improve the stability and robustness of SH surfaces for DR in practical applications.

CHAPTER V

Summary and Conclusions

5.1 Summary and Conclusions

Micro-textured surfaces have long been used for skin-friction DR in wall-bounded turbulent flows. One of the most successful designs of micro-textured surfaces for skin-friction DR were made with arrays of LMGs, known as riblets. The DR efficiency of riblets, however, has been limited to less than 10% to date. Recent advances in surface treatment techniques have made it possible to bypass this limit, by covering the micro-textured surfaces with non-wetting 'hydrophobic' coatings, thus creating Super-Hydrophobic (SH) surfaces. SH surfaces are characterized with a large apparent receding contact angle, typically greater than 150^o. When such surfaces come into contact with liquids, gas pockets form inside the surface indentations, thus preventing the liquid from penetrating into the cavities, and resulting in an apparent slip. It has been shown that when the surface micro-textures are in the form of LMGs, the resulting slip lengths are maximized. Experiments with SH LMGs in turbulent boundary layer flows have shown up to 75% DR. However, neither the scaling nor the mechanism of DR with SH surfaces is yet well understood. In addition, a detailed understanding of the pressure and stress loads on the liquid/gas interfaces in the SH surfaces is not yet at hand. These issues were investigated in this thesis, using results from DNS, and analysis of the governing equations in turbulent channel flow. To this

end:

- A D3Q19 single relaxation time Lattice Boltzmann Method (LBM) code was developed for the simulation of laminar and turbulent flow in channels with various patterns of surface micro-texture. In its basic formulation, LBM tracks the evolution of sets of particle Distribution Function (DF)s in space and time. This particle based Lagrangian view provides a completely local computational algorithm, which is inherently parallel, and highly efficient for the simulations of flows with complex boundaries, with second order accuracy. Because of its Lagrangian base, the boundary conditions in LBM are implemented through applying a set of bounce back, translation or reflection rules on the DFs at the boundaries. In this thesis, the no-slip boundary conditions on the flat and curved solid walls were imposed using half-way bounce back (*Succi*, 2001) and Central Linear Interpolation (CLI) (*Ginzburg et al.*, 2008) schemes, and the shear-free boundary condition was imposed using the specular reflection scheme (*Ginzburg and Steiner*, 2003). Because measurements of DR need to be performed by keeping the flow rate the same in the micro-textured channel and the base flow, a method for maintaining constant flow rate in channel flow simulations with LBM was developed and implemented in the code. In addition, to improve the accuracy of the simulations near the wall boundaries, while keeping the computational costs in check, a grid-embedding strategy (*Lagrava et al.*, 2012) was implemented in the code, which allows employment of patches of fine grids near the domain boundaries, and a coarse grid in the rest of the domain. Bi-cubic interpolation in space and second order Lagrange interpolation in time were used for data transfer between the grids.

- The code was parallelized using the MPI2 routines (*Gropp et al.*, 1999). A two dimensional domain decomposition strategy was employed, in which the simulation domain was divided into a two dimensional array of sub-domains,

in a toroidal topology. Single processor and parallel efficiency of the codes was optimized using cache optimization, vectorization, and persistent non-blocking communications. The simulation codes achieved a parallel efficiency of at least 97% on up to 1024 processes, on TACC's Stampede supercomputer.

- DNS studies were performed in turbulent channel flows, by maintaining a constant flow rate, at a bulk Reynolds number of $Re_{bulk} = 3600$ ($Re_{\tau_0} \approx 222$). Channels of size $L_x \times L_y \times L_z = 5h \times 2.5h \times 2h$, in the streamwise, spanwise and wall-normal directions, respectively, were used for all the simulations, where h denotes the half-height of the channel. The simulations were performed both with and without grid-embedding. For the LB DNS without grid-embedding, the lattice spacing was set at $\Delta^{+0} \approx 2$, where $+0$ denotes non-dimensionalization with respect to wall-friction velocity and kinematic viscosity of the base flow. The corresponding lattice resolutions were $512 \times 256 \times 221$ in the streamwise, spanwise and wall-normal directions, respectively. The simulations with grid-embedding were performed by placing patches of fine grids adjacent to the walls, in the regions between the domain boundaries and the buffer layer ($z^{+0} \lesssim 30$), while a coarser grid covered the rest of the domain. Lattice spacings of $\Delta_c^{+0} \approx 2$ and $\Delta_f^{+0} \approx 0.5$ were used on the coarse grid at $z^{+0} \gtrsim 30$, and the fine grid at $z^{+0} \lesssim 30$, respectively, corresponding to a grid refinement ratio of $4:1$. The corresponding lattice resolutions were $512 \times 256 \times 197$ in the streamwise, spanwise and wall-normal directions, respectively, on the coarse grid, and $2048 \times 1024 \times 56$ in the streamwise, spanwise and wall-normal directions, respectively, on the fine grids.

- DNS studies were performed in turbulent channel flow with SH LMGs of size $4 \lesssim g^{+0} \lesssim 128$ & $g/w = 1, 7, 15$, SH transverse MGs of size $8 \lesssim g^{+0} \lesssim 56$ & $g/w = 1, 7$ and SH micro-posts of size $8 \lesssim g^{+0} \lesssim 56$ & $g/w = 1, 7$ on both

walls, where g and w denote the width of the MGs and the separation in between them, respectively. The liquid/gas interfaces on the SH walls were modeled as 'idealized' flat, shear-free boundaries in these simulations. DRs of 5% to 83%, -4% to 20%, and 14% to 81% were realized in DNS with LMGs, transverse MGs, and micro-posts, respectively.

- A second set of DNS studies, in turbulent channel flows, with SH LMGs or scallop-shape riblets of size $14 \lesssim g^{+0} \lesssim 56$ & $g/w = 7$, on both walls, were also performed to investigate the effect of interface curvature, and compare the results to riblets. The liquid/gas interfaces on the SH wall in these simulations were modeled as stationary curved, shear-free regions, with the meniscus shape obtained from the solution of Young-Laplace equation. Simulations were performed for interface protrusion angles of $\theta = -0^o, -30^o, -60^o, -90^o$, covering the full range of negative interface protrusion angles. The same geometries as to those formed by SH LMGs were also used for riblets, by replacing the shear-free condition inside the MGs with the no-slip condition. DRs of 36% to 63% and 11% to -9% were realized in DNS with theses SH surfaces and riblets, respectively.

- By analysis of the governing equations, an exact expression for the magnitude of DR in channel flows with any pattern of SH or riblet micro-textures on the walls was derived. This expression provides a breakdown of DR into contributions from five sources: (i) the effective slip on the wall, (ii) the drop in the friction Reynolds number of the flow due to the presence of this surface slip, (iii) modifications to the normalized structure of turbulence due to the presence of surface micro-texture, (iv) the modifications to the structure of the mean flow due to the presence of surface micro-texture and (v) the minor changes in the cross-sectional area of the channel by the surface micro-texture.

- The contributions to DR which arise from effects (i) the effective slip on the wall, (ii) the drop in the friction Reynolds number of the flow due to the presence of this surface slip, and (v) the changes in the cross-sectional area of the channel, are always drag reducing by definition. Examination of DNS results showed that over 90% of the DR with SH LMGs and all of the DR with riblets arises from these contributions.

- The contributions to DR which arise from (iii) modifications to the normalized structure of turbulence, due to the presence of surface micro-texture, were shown by DNS to be always drag increasing with riblets. For riblets of size $g^{+0} \gtrsim 14$, these contributions became significant, and led to diminishing DRs and eventual DI with riblets of size $g^{+0} > 14$. With SH LMGs, these contributions were found to be drag enhancing for LMGs of size $g^{+} \gtrsim 20$, and mildly drag reducing (contributing $\lesssim 6.6\%$ DR) with LMGs of size $g^{+} \lesssim 20$.

- The presence of interface curvature on SH LMGs led to increases of 1.9% to 4.9% in the magnitude of DR, at low protrusion angles, $\theta = -30^o$, and drops of -0.5% to -9.8% in the magnitude of DR, at high protrusion angles, $\theta = -90^o$, compared to flat interfaces. For a given MG width, the highest DRs were always obtained at low protrusion angles ($\theta = -30$).

- The presence of interface curvature on SH LMGs led to drops of -3.5% to -13.5% in the slip velocity, at low protrusion angles, $\theta = -30^o$, and either drops of up to -16.4% or increases of up to 6.1% in the slip velocity, at high protrusion angles, $\theta = -90^o$, compared to flat interfaces. Because of the contributions arising from (iii) modifications to the normalized structure of turbulence, due to the presence of surface micro-texture, however, higher slip velocities with SH LMGs do not necessarily translate into higher DRs.

- The presence of interface curvature in SH LMGs also led to significant drops

(of up to 100%) in the normalized magnitudes of the pressure fluctuations with small MGs widths ($g^{+0} \approx 14$) at small protrusion angles, $\theta \sim -30$. This has significant implications for design of more robust SH surfaces.

- The highest DRs with riblets were obtained at the largest MG depths ($\theta = -90^o$), with the best DR performance achieved with MGs of size $g^{+0} \approx 14$. The slip velocity increased with MG depth and MG width, with the highest slip velocities obtained with the largest MG depths ($\theta = -90$) at $g^{+0} \approx 56$. However, for $g^{+0} \gtrsim 14$, this effect was negated by (iii), leading to diminishing DRs and eventual DI with riblets of size $g^{0+} > 14$.

- The effect of the SH surface on the dynamics of turbulence was found to be confined to additional production of TKE within a 'surface layer' of thickness on the order of the width of SH surface indentations.

The main findings of the present study are the common mechanism of DR with SH surfaces and riblets, and the drop in the pressure loads on the liquid/gas interfaces of the SH surface at low curvatures and small MG sizes. Using results from DNS and mathematical analysis, it was shown that, DR, with both the SH surfaces and riblets, arises from a common mechanism. This common mechanism is the surface slip, which is the sole mechanism of DR with riblets, and the dominant mechanism of DR with SH surfaces. In addition, by analysis of the DNS results, it was found that interface curvature has an important effect on the magnitude of pressure fluctuations on the liquid/gas interfaces on the SH surface. Small interface curvatures on narrow SH LMGs lead to significant drops in the magnitude of pressure fluctuations. This can be used for the design of hierarchical SH surfaces with better longevity and stability in turbulent flow environment.

CHAPTER VI

Future Works

6.1 Future Works

For successful application of SH surfaces as a means of skin-friction DR in wall-bounded turbulent flows, many issues remain to be addressed in future works.

In the DNS studies presented in this thesis, the SH surfaces were modeled as stationary, shear-free surfaces. However, on real SH surfaces in turbulent flows, the liquid/gas interfaces are not stationary. Interface dynamics can have significant effects on the resulting DRs, through providing compliance effects or introducing additional dissipation caused by its fluctuations. Hence, it would be beneficial to extend the current studies to include the dynamics of the liquid/gas interfaces. In addition, the liquid/gas interfaces on the SH surfaces are not totally shear-free. The additional shear on the interface can degrade the slip velocities developed on the surface, and thus the resulting DRs. As a result, investigation of the effect of this additional shear on the resulting slip velocities and DRs can be beneficial.

Furthermore, the simulations in this thesis were performed at a bulk Reynolds number of $Re_b = 3600$, corresponding to a friction Reynolds number of $Re_{\tau_0} \approx 222$. Turbulent flows in practical settings, however, are at much higher Reynolds numbers. Therefore, it would be beneficial to repeat the present DNS studies at higher Reynolds numbers, and investigate the effect of the Reynolds number of the flow on the results.

In addition, to maintain the stability of liquid/gas interfaces, the MG sizes on real SH surfaces are very small, of size on the order of 1 wall unit. To capture the dynamics of flow near such small MGs, however, an extremely fine grid is required near the walls. Nevertheless, the current DNS studies were performed on MGs of larger sizes, in order to keep the computational costs feasible. Future works should focus on smaller MG sizes by using several levels of grid-embedding, to avoid excessive computational costs.

Moreover, the DNS studies presented in this thesis were performed on SH surfaces with periodic patterns of surface micro-textures, such as LMGs, transverse MGs and micro-posts. In practice, however, SH surfaces with random patterns of micro-textures are easier to fabricate. Future studies should therefore focus on DR with SH surfaces with random patterns of micro-textures.

Finally, robustness and longevity of SH surfaces in turbulent flows are still open questions. It is not clear for how long a SH surface can sustain the high shear rates of turbulent flows, before the air inside the surface cavities is dragged out by the flow. In addition, robustness of liquid/gas interfaces on the SH surface under the pressure fluctuations in turbulent flows has not been investigated to date. Previous studies on this subject have been limited to a one-way coupling, in which the interfaces are modeled as stationary. Interaction of a dynamically moving interface with the pressure fields of a turbulent flow, however, is a non-linear problem for which a one-way coupling can not be justified. Future studies should focus on the robustness and longevity of the interface, by considering both the interface dynamics and shear, in order to design robust and enduring drag reducing surfaces for applications in turbulent flows. The current study showed that the normalized magnitudes of pressure fluctuations are smaller on small SH MGs at low interface curvatures. This feature can be used to design hierarchical surfaces, made of scallop-shaped riblets which are embedded with multiple narrow SH LMGs. The liquid/gas interfaces on the SH LMGs, with

these hierarchical surfaces, will experience lower pressure and shear loads. As a result, such hierarchical surfaces would provide more stable and durable SH surfaces. Future studies should investigate the DR characteristics of such hierarchical surfaces.

BIBLIOGRAPHY

BIBLIOGRAPHY

Aidun, C. K., and J. R. Clausen (2010), Lattice-Boltzmann Method for Complex Flows, *Annu. Rev. Fluid Mech.*, *42*(1), 439–472, doi:10.1146/annurev-fluid-121108-145519.

Amati, G., S. Succi, and R. Piva (1997), Massively parallel lattice-boltzmann simulation of turbulent channel flow, *Int. J. Mod. Phys. C*, *8*(04), 869–877.

Balasubramanian, A. K., A. C. Miller, and O. K. Rediniotis (2004), Microstructured Hydrophobic Skin for Hydrodynamic Drag Reduction, *AIAA J.*, *42*(2), 411–414, doi:10.2514/1.9104.

Bechert, D., and M. Bartenwerfer (1989), The viscous flow on surfaces with longitudinal ribs, *J. Fluid Mech.*, *206*, 105–129.

Bechert, D., M. Bruse, W. Hage, J. T. Van der Hoeven, and G. Hoppe (1997), Experiments on drag-reducing surfaces and their optimization with an adjustable geometry, *J. Fluid Mech.*, *338*, 59–87.

Belyaev, a. V., and O. I. Vinogradova (2010), Effective slip in pressure-driven flow past super-hydrophobic stripes, *J. Fluid Mech.*, *652*, 489–499, doi:10.1017/S0022112010000741.

Benzi, R., L. Biferale, M. Sbragaglia, S. Succi, and F. Toschi (2006), Mesoscopic modelling of heterogeneous boundary conditions for microchannel flows, *J. Fluid Mech.*, *548*(-1), 257, doi:10.1017/S0022112005007512.

Bespalko, D., A. Pollard, and M. Uddin (2012), Analysis of the pressure fluctuations from an LBM simulation of turbulent channel flow, *Comput. Fluids*, *54*, 143–146, doi:10.1016/j.compfluid.2011.10.008.

Bhatnagar, P. L., E. P. Gross, and M. Krook (1954), A model for collision processes in gases. i. small amplitude processes in charged and neutral one-component systems, *Physical review*, *94*(3), 511.

Borue, V., S. A. Orszag, and I. Staroselsky (1995), Interaction of Surface Waves with turbulence: direct numerical simulation of turbulent open channel flow, *J. Fluid Mech.*, *286*, 1–32.

Bushnell, D., and J. Hefner (1990), *Viscouse drag reduction in boundary layers*, AIAA.

Bushnell, D. M., and C. B. McGinley (1989), Turbulence Control in Wall Flows, *Annu. Rev. Fluid Mech.*, *21*, 1–20, doi:10.1146/annurev.fl.21.010189.000245.

Busse, A., and N. D. Sandham (2012), Influence of an anisotropic slip-length boundary condition on turbulent channel flow, *Phys. Fluids.*, *24*(5), 055,111, doi: 10.1063/1.4719780.

Cao, N., S. Chen, S. Jin, and D. Martinez (1997), Physical symmetry and lattice symmetry in the lattice boltzmann method, *Phys. Rev. E*, *55*, R21–R24, doi: 10.1103/PhysRevE.55.R21.

Cha, T.-G., J. W. Yi, M.-W. Moon, K.-R. Lee, and H.-Y. Kim (2010), Nanoscale patterning of microtextured surfaces to control superhydrophobic robustness, *Langmuir*, *26*(11), 8319–8326.

Checco, A., B. M. Ocko, A. Rahman, C. T. Black, M. Tasinkevych, A. Giacomello, and S. Dietrich (2014), Collapse and reversibility of the superhydrophobic state on nanotextured surfaces, *Phys. Rev. Lett.*, *112*(21), 216,101.

Chen, S., and G. D. Doolen (1998), Latice boltzmann method for fluid flows, *Annu. Rev. Fluid Mech.*, *30*(1), 329–364, doi:10.1146/annurev.fluid.30.1.329.

Chernyshov, O., and V. Zayets (1970), Some peculiarities of the structure of the skin of sharks, *Hydrodynamic Problems of Bionics (in Russian)*, *4*, 77–83.

Chikatamarla, S. S., S. Ansumali, and I. V. Karlin (2006), Entropic lattice boltzmann models for hydrodynamics in three dimensions, *Phys. Rev. Lett.*, *97*, 010,201.

Choi, C.-H., U. Ulmanella, J. Kim, C.-M. Ho, and C.-J. Kim (2006), Effective slip and friction reduction in nanograted superhydrophobic microchannels, *Phys. Fluids.*, *18*(8), 087,105, doi:10.1063/1.2337669.

Choi, H., P. Moin, and J. Kim (1991), On the effect of riblets in fully developed laminar channel flows, *Phys. Fluids A Fluid Dyn.*, *3*(8), 1892, doi:10.1063/1.857918.

Choi, H., P. Moin, and J. Kim (1993), Direct numerical simulation of turbulent flow over riblets, *J. Fluid Mech.*, *255*, 503–539.

Choi, K.-s. (1989), Near-wall structure of a turbulent boundary layer with riblets, *J. Appl. Phys.*, *208*, 417–458.

Chu, D. C., and G. E. Karniadakis (1993), A direct numerical simulation of laminar and turbulent flow over riblet-mounted surfaces, *J. Fluid Mech.*, *250*, 1–42.

Corrsin, S. (1953), Interpretation of viscous terms in the turbulent energy equation, *Journal of the Aeronautical Sciences*, *20*(12), 853–854, doi:10.2514/8.2881.

Coustols, E., and A. Savill (1992a), *Turbulent Skin-Friction Drag Reduction By Active and Passive Means. Part 1. Everything You Wanted to Know about Riblets, LEBUs and Other Devices*, OFFICE NATIONAL D'ETUDES ET DE RECHERCHES AEROSPATIALES TOULOUSE (France), Defense Technical Information Center.

Coustols, E., and A. Savill (1992b), *Turbulent Skin-Friction Drag Reduction By Active and Passive Means. Part 2.*, OFFICE NATIONAL D'ETUDES ET DE RECHERCHES AEROSPATIALES TOULOUSE (France), Defense Technical Information Center.

Crowdy, D. (2010), Slip length for longitudinal shear flow over a dilute periodic mattress of protruding bubbles, *Phys. Fluids. (1994-present)*, *22*(12), 121,703.

Crowdy, D. G. (2016), Analytical formulae for longitudinal slip lengths over unidirectional superhydrophobic surfaces with curved menisci, *J. Fluid Mech.*, *791*, R7.

Daniello, R. J., N. E. Waterhouse, and J. P. Rothstein (2009), Drag reduction in turbulent flows over superhydrophobic surfaces, *Phys. Fluids.*, *21*(8), 085,103, doi:10.1063/1.3207885.

Davies, J., D. Maynes, B. Webb, and B. Woolford (2006), Laminar flow in a microchannel with superhydrophobic walls exhibiting transverse ribs, *Phys. Fluids*, *087110*(2006), doi:10.1063/1.2336453.

Davis, A. M. J., and E. Lauga (2009), The friction of a mesh-like super-hydrophobic surface, *Phys. Fluids.*, *21*(11), 113,101, doi:10.1063/1.3250947.

Davis, A. M. J., and E. Lauga (2010), Hydrodynamic friction of fakir-like superhydrophobic surfaces, *J. Fluid Mech.*, *661*, 402–411, doi:10.1017/S0022112010003460.

De Gennes, P.-G., F. Brochard-Wyart, and D. Quéré (2002), *Capillarity and wetting phenomena: drops, bubbles, pearls, waves*, Springer.

Dean, R. B. (1978), Reynolds Number Dependence of Skin Friction and Other Bulk Flow Variables in Two-Dimensional Rectangular Duct Flow, *J. Fluids Eng.*, *100*(2), 215, doi:10.1115/1.3448633.

D'Humières, D., I. Ginzburg, M. Krafczyk, P. Lallemand, and L.-S. Luo (2002), Multiple-relaxation-time lattice Boltzmann models in three dimensions., *Philos. Trans. A. Math. Phys. Eng. Sci.*, *360*(1792), 437–51, doi:10.1098/rsta.2001.0955.

Eggels, J. G. (1996), Direct and large-eddy simulation of turbulent fluid flow using the lattice-boltzmann scheme, *Int. J. Heat Fluid Flow*, *17*(3), 307–323.

Feng, L., et al. (2002), Super-hydrophobic surfaces: from natural to artificial, *Adv. Mater.*, *14*(24), 1857–1860.

Feuillebois, F., M. Bazant, and O. Vinogradova (2009), Effective Slip over Superhydrophobic Surfaces in Thin Channels, *Phys. Rev. Lett.*, *102*(2), 026,001, doi:10.1103/PhysRevLett.102.026001.

Filippova, O., and D. Hänel (1998), Grid Refinement for Lattice-BGK Models, *J. Comput. Phys.*, *147*(1), 219–228, doi:10.1006/jcph.1998.6089.

Frigo, M., and S. G. Johnson (1998), Fftw: An adaptive software architecture for the fft, in *Acoustics, Speech and Signal Processing, 1998. Proceedings of the 1998 IEEE International Conference on*, vol. 3, pp. 1381–1384, IEEE.

Fukagata, K., K. Iwamoto, and N. Kasagi (2002), Contribution of Reynolds stress distribution to the skin friction in wall-bounded flows, *Phys. Fluids.*, *14*(11), L73, doi:10.1063/1.1516779.

Fukagata, K., N. Kasagi, and P. Koumoutsakos (2006), A theoretical prediction of friction drag reduction in turbulent flow by superhydrophobic surfaces, *Phys. Fluids.*, *18*(5), 051,703, doi:10.1063/1.2205307.

García-Mayoral, R., and J. Jiménez (2011), Hydrodynamic stability and breakdown of the viscous regime over riblets, *J. Fluid Mech.*, *678*, 317–347, doi: 10.1017/jfm.2011.114.

Ginzburg, I., and K. Steiner (2003), Lattice Boltzmann model for free-surface flow and its application to filling process in casting, *J. Comput. Phys.*, *185*(1), 61–99, doi:10.1016/S0021-9991(02)00048-7.

Ginzburg, I., F. Verhaeghe, and D. D'Humières (2008), Study of Simple Hydrodynamic Solutions with the Two-Relaxation-Times Lattice Boltzmann Scheme, *Commun. Comput. Phys.*, *3*(3), 519–581.

Goldstein, D., and T. Tuan (1998), Secondary flow induced by riblets, *J. Fluid Mech.*, *363*, 115–151.

Gropp, W., E. Lusk, and R. Thakur (1999), *Using MPI-2: Advanced features of the message-passing interface*, MIT press.

Guo, Z., and T. Zhao (2002), Lattice Boltzmann model for incompressible flows through porous media, *Phys. Rev. E*, *66*(3), 1–9, doi:10.1103/PhysRevE.66.036304.

Hao, P.-F., C. Wong, Z.-H. Yao, and K.-Q. Zhu (2009), Laminar Drag Reduction in Hydrophobic Microchannels, *Chem. Eng. Technol.*, *32*(6), 912–918, doi: 10.1002/ceat.200900001.

He, X., and L.-S. Luo (1997), Theory of the lattice boltzmann method: From the boltzmann equation to the lattice boltzmann equation, *Phys. Rev. E*, *56*, 6811–6817, doi:10.1103/PhysRevE.56.6811.

Hinze, J. O. (1975), *Turbulence*, 2nd ed., Mc Graw-Hill.

Holdych, D. J., D. R. Noble, J. G. Georgiadis, and R. O. Buckius (2004), Truncation error analysis of lattice Boltzmann methods, *J. Comput. Phys.*, *193*(2), 595–619, doi:10.1016/j.jcp.2003.08.012.

Hyväluoma, J., and J. Harting (2008), Slip flow over structured surfaces with entrapped microbubbles, *Phys. Rev. Lett.*, *100*(24), 246,001.

Jelly, T., S. Jung, and T. Zaki (2014), Turbulence and skin friction modification in channel flow with streamwise-aligned superhydrophobic surface texture, *Phys. Fluids. (1994-present)*, *26*(9), 095,102.

Jimenez, J. (1994), On the structure and control of near wall turbulence, *Phys. Fluids.*, *6*(2), 944, doi:10.1063/1.868327.

Jung, T., H. Choi, and J. Kim (2016), Effects of the air layer of an idealized superhydrophobic surface on the slip length and skin-friction drag, *J. Fluid Mech.*, *790*, R1.

Karatay, E., a. S. Haase, C. W. Visser, C. Sun, D. Lohse, P. A. Tsai, and R. G. H. Lammertink (2013a), Control of slippage with tunable bubble mattresses., *Proc. Natl. Acad. Sci. U. S. A.*, *110*, 8422–6, doi:10.1073/pnas.1304403110.

Karatay, E., P. A. Tsai, and R. G. Lammertink (2013b), Rate of gas absorption on a slippery bubble mattress, *Soft matter*, *9*(46), 11,098–11,106.

Karniadakis, G., and K.-S. Choi (2003), Mechanisms of Transverse Motions in Turbulent Wall Flows, *Annu. Rev. Fluid Mech.*, *35*(1), 45–62, doi:10.1146/annurev.fluid.35.101101.161213.

Kim, B. J., P. Moin, and R. Moser (1987), Turbulence statistics in fully developed channel flow at low Reynolds number, *J. Fluid Mech.*, *177*, 133–166.

Komori, S., R. Nagaosa, Y. Murakami, S. Chiba, K. Ishii, and K. Kuwahara (1993), Direct numerical simulation of three-dmensional open-channel flow with zero-shear gas-liquid interface, *Phys. Fluids.*, *5*(1), 115–125.

Krüger, T., F. Varnik, and D. Raabe (2010), Second-order convergence of the deviatoric stress tensor in the standard bhatnagar-gross-krook lattice boltzmann method, *Phys. Rev. E*, *82*.

Kwon, Y., N. Patankar, J. Choi, and J. Lee (2009), Design of surface hierarchy for extreme hydrophobicity, *Langmuir*, *25*(11), 6129–6136.

Ladd, A. J. C., and R. Verberg (2001), Lattice-Boltzmann Simulations of Particle-Fluid Suspensions, *J. Stat. Phys.*, *104*(5-6), 1191–1251, doi:10.1023/A:1010414013942.

Lagrava, D., O. Malaspinas, J. Latt, and B. Chopard (2012), Advances in multi-domain lattice Boltzmann grid refinement, *J. Comput. Phys.*, *231*(14), 4808–4822, doi:10.1016/j.jcp.2012.03.015.

Lammers, P., K. Beronov, R. Volkert, G. Brenner, and F. Durst (2006), Lattice BGK direct numerical simulation of fully developed turbulence in incompressible plane channel flow, *Comput. Fluids*, *35*(10), 1137–1153, doi:10.1016/j.compfluid.2005.10.002.

Latt, J. (2007), Hydrodynamic limit of lattice boltzmann equations, Ph.D. thesis, University of Geneva.

Latt, J., and B. Chopard (2008), Straight velocity boundaries in the lattice Boltzmann method, *Phys. Rev. E*, *77*(5), 056,703, doi:10.1103/PhysRevE.77.056703.

Lauga, E., and H. A. Stone (2003), Effective slip in pressure-driven Stokes flow, *J. Fluid Mech.*, *489*, 55–77, doi:10.1017/S0022112003004695.

Lee, C., and C.-J. Kim (2011), Underwater restoration and retention of gases on superhydrophobic surfaces for drag reduction, *Phys. Rev. Lett.*, *106*(1), 014,502.

Lee, C., and C.-J. . Kim (2009), Maximizing the giant liquid slip on superhydrophobic microstructures by nanostructuring their sidewalls, *Langmuir*, *25*(21), 12,812–12,818.

Lee, C., C.-H. Choi, and C.-J. Kim (2008), Structured Surfaces for a Giant Liquid Slip, *Phys. Rev. Lett.*, *101*(6), 064,501, doi:10.1103/PhysRevLett.101.064501.

Ling, H., S. Srinivasan, K. Golovin, G. H. McKinley, A. Tuteja, and J. Katz (2016), High-resolution velocity measurement in the inner part of turbulent boundary layers over super-hydrophobic surfaces, *J. Fluid Mech.*, *801*, 670–703, doi:10.1017/jfm.2016.450.

Luchini, P. (1995), Asymptotic analysis of laminar boundary-layer flow over finely grooved surfaces, *Eur. J. Mech. B/Fluids*, *14*(2), 169–195.

Lumley, J., and P. Blossey (1998), Control of Turbulence, *Annu. Rev. Fluid Mech.*, *30*(1), 311–327, doi:10.1146/annurev.fluid.30.1.311.

Lumley, J. L. (1969), Drag Reduction by Additives, *Annu. Rev. Fluid Mech.*, *1*(1), 367–384, doi:10.1146/annurev.fl.01.010169.002055.

Ma, M., and R. M. Hill (2006), Superhydrophobic surfaces, *Curr. Opin. Colloid Interface Sci.*, *11*(4), 193–202.

Martell, M. B., J. B. Perot, and J. P. Rothstein (2009), Direct numerical simulations of turbulent flows over superhydrophobic surfaces, *J. Fluid Mech.*, *620*, 31, doi:10.1017/S0022112008004916.

Martell, M. B., J. P. Rothstein, and J. B. Perot (2010), An analysis of superhydrophobic turbulent drag reduction mechanisms using direct numerical simulation, *Phys. Fluids.*, *22*(6), 065,102, doi:10.1063/1.3432514.

Maynes, D., K. Jeffs, B. Woolford, and B. W. Webb (2007), Laminar flow in a microchannel with hydrophobic surface patterned microribs oriented parallel to the flow direction, *Phys. Fluids.*, *19*(9), 093,603, doi:10.1063/1.2772880.

Mei, R., W. Shyy, D. Yu, and L.-S. Luo (2000), Lattice boltzmann method for 3-d flows with curved boundary, *J. Comput. Phys.*, *161*(2), 680–699.

Min, T., and J. Kim (2004), Effects of hydrophobic surface on skin-friction drag, *Phys. Fluids.*, *16*(7), L55, doi:10.1063/1.1755723.

Mohammadi, A., and J. M. Floryan (2013), Pressure losses in grooved channels, *J. Fluid Mech.*, *725*, 23–54.

Mohammadi, A., and J. M. Floryan (2015), Numerical Analysis of Laminar-Drag-Reducing Grooves, *J. Fluids Eng.*, *137*(4), 041,201, doi:10.1115/1.4028842.

Nishino, T., M. Meguro, K. Nakamae, M. Matsushita, and Y. Ueda (1999), The lowest surface free energy based on-cf3 alignment, *Langmuir*, *15*(13), 4321–4323.

Nourgaliev, R., T. Dinh, T. Theofanous, and D. Joseph (2003), The lattice boltzmann equation method: theoretical interpretation, numerics and implications, *Int. J. Multiphase Flow*, *29*(1), 117 – 169.

Ogata, S., and K. Shimizu (2011), Drag Reduction by Hydrophobic Microstructures, *Journal of Environment and Engineering*, *6*(2), 291–301, doi:10.1299/jee.6.291.

Orszag, S. A., and A. T. Patera (1983), Secondary instability of wall-bounded shear flows, *J. Fluid Mech.*, *128*, 347–385.

Ou, J., and J. P. Rothstein (2005), Direct velocity measurements of the flow past drag-reducing ultrahydrophobic surfaces, *Phys. Fluids.*, *17*(10), 103,606, doi:10.1063/1.2109867.

Ou, J., B. Perot, and J. P. Rothstein (2004), Laminar drag reduction in microchannels using ultrahydrophobic surfaces, *Phys. Fluids.*, *16*(12), 4635, doi:10.1063/1.1812011.

Papageorgiou, D. P., K. Tsougeni, A. Tserepi, and E. Gogolides (2012), Superhydrophobic, hierarchical, plasma-nanotextured polymeric microchannels sustaining high-pressure flows, *Microfluid Nanofluid*, *14*(1-2), 247–255, doi:10.1007/s10404-012-1043-2.

Park, H., H. Park, and J. Kim (2013), A numerical study of the effects of superhydrophobic surface on skin-friction drag in turbulent channel flow, *Phys. Fluids. (1994-present)*, *25*(11), 110,815.

Park, H., G. Sun, et al. (2014), Superhydrophobic turbulent drag reduction as a function of surface grating parameters, *J. Fluid Mech.*, *747*, 722–734.

Peet, Y., and P. Sagaut (2009), Theoretical prediction of turbulent skin friction on geometrically complex surfaces, *Phys. Fluids.*, *21*(10), 105,105, doi: 10.1063/1.3241993.

Peguero, C., and K. Breuer (2009), On Drag Reduction in Turbulent Channel Flow over Superhydrophobic Surfaces, in *Advances in Turbulence XII Proceedings of the 12th EUROMECH European Turbulence Conference, September 7-10, 2009, Marburg, Germany*, edited by B. Eckhardt, pp. 233–236, Springer Berlin Heidelberg, doi:10.1007/978-3-642-03085-7_57.

Perkins, H. J. (1970), The formation of streamwise vorticity in turbulent flow, *J. Fluid Mech.*, *44*(04), 721, doi:10.1017/S0022112070002112.

Philip, J. R. (1972a), Flows satisfying mixed no-slip and no-shear conditions, *Zeitschrift für angewandte Mathematik und Physik ZAMP*, *23*(3), 353–372, doi: 10.1007/BF01595477.

Philip, J. R. (1972b), Integral properties of flows satisfying mixed no-slip and no-shear conditions, *Zeitschrift für angewandte Mathematik und Physik ZAMP*, *23*(6), 960–968, doi:10.1007/BF01596223.

Pope, S. (2000), *Turbulent Flows*, Cambridge University Press.

Premnath, K. N., M. J. Pattison, and S. Banerjee (2009), Generalized lattice boltzmann equation with forcing term for computation of wall-bounded turbulent flows, *Phys. Rev. E*, *79*, 026,703, doi:10.1103/PhysRevE.79.026703.

Qian, Y., and S. Orszag (1993), Lattice BGK models for the Navier-Stokes equation: Nonlinear deviation in compressible regimes, *EPL*, *21*(3), 255–259.

Rastegari, A., and R. Akhavan (2013), Lattice boltzmann simulations of drag reduction by super-hydrophobic surfaces, in *Proc. 14th ETC Conf., September 1-4, 2013.*

Rastegari, A., and R. Akhavan (2015), On the mechanism of turbulent drag reduction with super-hydrophobic surfaces, *J. Fluid Mech.*, *773*(R4).

Rastegari, A., and R. Akhavan (2016a), Structure and dynamics of turbulence in super-hydrophobic channel flow, in *Progress in wall turbulence: Understanding and Modelling*, Springer International Publishing.

Rastegari, A., and R. Akhavan (2016b), The common mechanism of turbulent skin-friction drag reduction with superhydrophobic surfaces and riblets, *In process.*

Rathgen, H., and F. Mugele (2010), Microscopic shape and contact angle measurement at a superhydrophobic surface, *Farad. Discuss*, *146*, 49–56.

Rosenberg, B. J., T. Van Buren, M. K. Fu, and A. J. Smits (2016), Turbulent drag reduction over air-and liquid-impregnated surfaces, *Phys. Fluids. (1994-present)*, *28*(1), 015,103.

Rothstein, J. P. (2010), Slip on Superhydrophobic Surfaces, *Annu. Rev. Fluid Mech.*, *42*(1), 89–109, doi:10.1146/annurev-fluid-121108-145558.

Samaha, M. A., H. V. Tafreshi, and M. Gad-el Hak (2012), Influence of Flow on Longevity of Superhydrophobic Coatings, *Langmuir*, *28*(25), 9759–9766, doi:10.1021/la301299e.

Sbragaglia, M., and A. Prosperetti (2007), A note on the effective slip properties for microchannel flows with ultrahydrophobic surfaces, *Phys. Fluids. (1994-present)*, *19*(4), 043,603.

Schellenberger, F., N. Encinas, D. Vollmer, and H.-J. Butt (2016), How water advances on superhydrophobic surfaces, *Phys. Rev. Lett.*, *116*(9), 096,101.

Seo, J., and A. Mani (2016), On the scaling of the slip velocity in turbulent flows over superhydrophobic surfaces, *Phys. Fluids*, *28*(2), 025,110, doi:10.1063/1.4941769.

Seo, J., R. García-Mayoral, and A. Mani (2015), Pressure fluctuations and interfacial robustness in turbulent flows over superhydrophobic surfaces, *J. Fluid Mech.*, *783*, 448–473.

Smith, C., and S. Metzler (1983), The characteristics of low-speed streaks in the near-wall region of a turbulent boundary layer, *J. Fluid Mech.*, *129*, 27–54.

Solomon, B. R., K. S. Khalil, and K. K. Varanasi (2014), Drag Reduction using Lubricant-Impregnated Surfaces in Viscous Laminar Flow, *Langmuir*, *30*(36), 10,970–10,976, doi:10.1021/la5021143.

Steinberger, A., C. Cottin-Bizonne, P. Kleimann, and E. Charlaix (2007), High friction on a bubble mattress., *Nature Materials*, *6*(9), 665–8, doi:10.1038/nmat1962.

Succi, S. (2001), *The Lattice Boltzmann Equation for Fluid Dynamics and Beyond*, Oxford University Press.

Touil, H., D. Ricot, and E. Lévêque (2014), Direct and large-eddy simulation of turbulent flows on composite multi-resolution grids by the lattice Boltzmann method, *J. Comput. Phys.*, *256*, 220–233, doi:10.1016/j.jcp.2013.07.037.

Tretheway, D. C., and C. D. Meinhart (2004), A generating mechanism for apparent fluid slip in hydrophobic microchannels, *Phys. Fluids.*, *16*(5), 1509, doi:10.1063/1.1669400.

Truesdell, R., A. Mammoli, P. Vorobieff, F. van Swol, and C. Brinker (2006), Drag Reduction on a Patterned Superhydrophobic Surface, *Phys. Rev. Lett.*, *97*(4), 1–4, doi:10.1103/PhysRevLett.97.044504.

Tsai, P., A. M. Peters, C. Pirat, M. Wessling, R. G. H. Lammertink, and D. Lohse (2009), Quantifying effective slip length over micropatterned hydrophobic surfaces, *Phys. Fluids.*, *21*(11), 112,002, doi:10.1063/1.3266505.

Türk, S., G. Daschiel, A. Stroh, Y. Hasegawa, and B. Frohnapfel (2014), Turbulent flow over superhydrophobic surfaces with streamwise grooves, *J. Fluid Mech.*, *747*, 186–217.

Tyrrell, J. W. G., and P. Attard (2001), Images of Nanobubbles on Hydrophobic Surfaces and Their Interactions, *Phys. Rev. Lett.*, *87*(17), 1–4, doi: 10.1103/PhysRevLett.87.176104.

Voronov, R. S., D. V. Papavassiliou, and L. L. Lee (2008), Review of Fluid Slip over Superhydrophobic Surfaces and Its Dependence on the Contact Angle, *Industrial & Engineering Chemistry Research*, *47*(8), 2455–2477, doi:10.1021/ie0712941.

Wang, L., C. Teo, and B. Khoo (2014), Effects of interface deformation on flow through microtubes containing superhydrophobic surfaces with longitudinal ribs and grooves, *Microfluid Nanofluid*, *16*(1-2), 225–236.

Wang, Z., N. Koratkar, L. Ci, and P. Ajayan (2007), Combined micro-/nanoscale surface roughness for enhanced hydrophobic stability in carbon nanotube arrays, *Appl. Phys. Lett.*, *90*(14), 143,117.

Watanabe, K., Y. Udagawa, and H. Udagawa (1999), Drag reduction of Newtonian fluid in a circular pipe with a highly water-repellent wall, *J. Fluid Mech.*, *381*(September 2000), 225–238, doi:10.1017/S0022112098003747.

Watanabe, K., T. Takayama, S. Ogata, and S. Isozaki (2003), Flow between two coaxial rotating cylinders with a highly water-repellent wall, *AIChE J.*, *49*(8), 1956–1963, doi:10.1002/aic.690490805.

Watanabe, K., S. Ogata, A. Hirose, and A. Kimura (2007), Flow Characteristics of the Drag Reducing Solid Wall, *Journal of Environment and Engineering*, *2*(1), 108–114, doi:10.1299/jee.2.108.

Wellein, G., T. Zeiser, G. Hager, and S. Donath (2006), On the single processor performance of simple lattice boltzmann kernels, *Comput. Fluids*, *35*(8), 910–919.

Wexler, J. S., I. Jacobi, and H. A. Stone (2015), Shear-Driven Failure of Liquid-Infused Surfaces, *Phys. Rev. Lett.*, *114*(16), 168,301, doi: 10.1103/PhysRevLett.114.168301.

Wilke, J., T. Pohl, M. Kowarschik, and U. Rüde (2003), Cache performance optimizations for parallel lattice boltzmann codes, in *European Conference on Parallel Processing*, pp. 441–450, Springer.

Wolf-Gladrow, D. A. (2000), *Lattice-gas cellular automata and lattice Boltzmann models: an introduction*, 1725, Springer.

Wong, T.-S., S. H. Kang, S. K. Tang, E. J. Smythe, B. D. Hatton, A. Grinthal, and J. Aizenberg (2011), Bioinspired self-repairing slippery surfaces with pressure-stable omniphobicity, *Nature*, *477*(7365), 443–447.

Woolford, B., J. Prince, D. Maynes, and B. W. Webb (2009), Particle image velocimetry characterization of turbulent channel flow with rib patterned superhydrophobic walls, *Phys. Fluids.*, *21*(085106), doi:10.1063/1.3213607.

Zheng, Q.-S., Y. Yu, and Z.-H. Zhao (2005), Effects of hydraulic pressure on the stability and transition of wetting modes of superhydrophobic surfaces, *Langmuir*, *21*(26), 12,207–12,212.